Cross Correlation of IceCube Neutrinos with Tracers of Large Scale Structure

by

David J. Guevel

A dissertation submitted in partial fulfillment of
the requirements for the degree of

Doctor of Philosophy

(Physics)

at the

UNIVERSITY OF WISCONSIN–MADISON

2025

Date of final oral examination: July 7, 2025

The dissertation is approved by the following members of the Final Oral Committee:

Ke Fang, Assistant Professor, Physics
Justin Vandenbroucke, Associate Professor, Physics
Keith Bechtol, Associate Professor, Physics
Francis Halzen, Professor, Physics
Ellen Zweibel, Professor, Astronomy

© Copyright by David J. Guevel 2025

All Rights Reserved

ACKNOWLEDGMENTS

My parents, Teresa and Rick, supported me in my scientific career from early childhood. They encouraged my academic career and encouraged me to learn about the natural world. My sisters Lauren and Lindsey Guevel have been peers whom I have drawn inspiration from in the study of science and engineering.

This thesis would not have been possible without the patience and support of my wife Krysten Pfau. Despite the long work hours and cold Wisconsin winters, she never doubted my decision to pursue a PhD.

Ke Fang deserves the lion's share of the credit for my development as a scientist. Her supervision provided the light touch needed to guide my research to fruition while allowing me to succeed and sometimes fail on my own merits.

The students, faculty, and staff at the Wisconsin IceCube Particle Astrophysics Center and the Physics Department at UW Madison have provided a friendly and collaborative atmosphere. I am particularly grateful for the friends and colleagues I have made at UW Madison: Angelina Partenheimer, Emily Joseph, Paul Gradney, and Will Luszczak.

I learned an enormous amount from my prior research experience with the REXIS telescope team and at Las Cumbres Observatory. Josh Grindlay, Rick Binzel, Jaesub Hong, Branden Allen, and Dan Hoak taught me how to work as a member of a scientific collaboration and introduced me to high-energy astrophysics. Carolyn Thayer, Maddy Lambert, and Mark Chodas were valuable peers then and remain close friends today. At Las Cumbres Observatory, Andy Howell, Iair Arcavi, and Griffin Hosseinzadeh were my first scientific mentors and their influence shaped the way I approach research.

CONTENTS

Contents ii

List of Tables v

List of Figures vi

Abstract ix

1 Introduction 1

2 Multi-Messenger Astrophysics 4

2.1 Introduction 4

2.2 Photon and Neutrino Physics 4

2.3 Cherenkov Radiation 10

2.4 Cosmic Ray Astrophysics 15

2.5 γ-ray Astrophysics 23

2.6 Neutrino Astrophysics 24

2.7 Summary 34

3 The Large-Scale Structure 35

3.1 Introduction 35

3.2 Two-Point Correlations 35

3.3 Large-Scale Structure 40

3.4 Summary 47

4 IceCube Neutrino Observatory 49

4.1 Introduction 49

4.2 Neutrino Interactions 49

4.3 The IceCube Detector 52

4.4 Event Morphology 55

4.5 Northern Tracks Data Set 58

4.6 Summary 60

5 IceCube Cross-Correlation: Methods and Results 61

5.1 Introduction 61

5.2 unWISE-2MASS Galaxy Catalog 61

5.3 Neutrino Mapmaking 67

5.4 Simulated Data Set Generation 69

5.5 Cross Correlation Likelihood Formalism 71

5.6 Astrophysical Model Estimation 74

5.7 Atmospheric Model Estimation 76

5.8 Covariance Matrix Estimation 77

5.9 Hypothesis Testing 78

5.10 Estimator Bias 79

5.11 Systematic Uncertainties 80

5.12 Goodness of Fit 82

5.13 Stress Tests 83

5.14 Results 87

5.15 Summary 91

6 IceCube Cross-Correlation: Interpretation 95

6.1 Introduction 95

6.2 Correlated Neutrino Flux Constraint 95

6.3 Neutrino Source Population Modeling 97

6.4 Power Law Source Distribution 101

6.5 unWISE-2MASS Tracing 103

6.6 No Evolution 105

6.7 Star Formation Rate Evolution 106

6.8 Summary 106

7 Outlook 108

A Hypothesis Testing 111

B Software 116

B.1 Source 116

B.2 Scripts 117

References 119

LIST OF TABLES

2.1 Cosmic Ray Observatories 15

2.2 Diffuse Neutrino Single Power Law Measurements from IceCube 33

5.1 Parameters Varied in Systematic Uncertainty Estimation 82

5.2 Summary of Fit Parameters 92

5.3 Upper Limits for Various Spectral Indices 93

6.1 Correlation Strength for Non-Parametric Models 106

LIST OF FIGURES

2.1 Compton Scattering Diagram 9
2.2 Inverse Compton Scattering Energy Distribution 11
2.3 Huygens' Principle for Cherenkov Radiation 12
2.4 Feynman diagrams for decay of π^+ and μ^- 14
2.5 Cosmic Ray Energy Spectrum 17
2.6 Cosmic Ray Composition 18
2.7 Hillas Criterion for Cosmic Ray Source Candidates 21
2.8 Diffuse Multi-Messenger Spectral Energy Distribution 23
2.9 Neutrino Emission from Astrophysical and Anthropogenic Sources 25
2.10 TXS 0506+056 Spectral Energy Distribution 27
2.11 NGC 1068 Spectral Energy Distribution 29
2.12 Multi-Messenger View of the Galactic Plane 32
2.13 Diffuse Neutrino Flux Power Law Measurements 33

3.1 Sloan Digital Sky Survey Large Scale Structure 41
3.2 Matter Power Spectrum 42

4.1 Weak Interaction Vertices for Neutrinos 50
4.2 Neutral Current Interaction 51
4.3 Charged Current Interaction 52
4.4 IceCube Detector Schematic 53
4.5 IceCube String Layout 54
4.6 Digital Optical Module Engineering Diagram 56
4.7 Neutrino Flavor and Event Morphology 57
4.8 IceCube Track Event 58

5.1 WISE and 2MASS Passbands 62

5.2 unWISE-2MASS Galaxy Density 65
5.3 unWISE-2MASS Redshift Distribution 66
5.4 unWISE-2MASS Angular Power Spectrum 68
5.5 Inverse IceCube Weight Maps 70
5.6 IceCube unWISE-2MASS Cross-Correlation Model Templates 75
5.7 Kernel Density Estimate of Atmospheric Neutrinos 76
5.8 Atmospheric Model Template MC-Data Agreement 77
5.9 unWISE-2MASS Multipole Correlation Matrix 78
5.10 Bias of Astrophysical Fit Parameters 81
5.11 Fractional Systematic Uncertainty 83
5.12 Cross-Correlation Goodness-of-Fit 84
5.13 Test Statistic Distribution Including Bright Point Sources 85
5.14 Test Statistic Distribution Including Isotropic Background 86
5.15 Test Statistic Distribution Including Uncorrelated Large Scale Structure Background 88
5.16 Cross Correlation Test Statistic Distribution 89
5.17 Unblinded Cross Power Spectra 90
5.18 Binned Residual Cross Power Spectra 90
5.19 Unblinded Goodness of Fit 91
5.20 Cross Correlation Likelihood Contours 92
5.21 Cross Correlation Likelihood CDF with $\gamma = 2.37$ 94

6.1 Cross Correlation Upper Limits 96
6.2 SFR Source and Counts Distribution 100
6.3 Power Law Counts Distributions 102
6.4 Neutrino Source Distribution Constraints 103
6.5 Two Dimensional Neutrino Source Distribution Constraints 104
6.6 Constraints of SFR and No Evolution Populations 105

7.1 Projected Cross Power Spectra Relative Uncertainty 110

ABSTRACT

Multi-messenger astrophysics aims to study energetic astrophysical environments using physical channels that have historically been inaccessible. Technological developments have created new opportunities to detect neutrinos, cosmic rays, and gravitational waves from distant astrophysical environments. Neutrinos are unique among these messengers because they are produced in large numbers in energetic environments and because they propagate through interstellar and intergalactic space with little interaction along the way preserving the information about their sources. The IceCube Neutrino Observatory has discovered astrophysical neutrinos from extragalactic, and galactic sources and unresolved background sources. The accelerators that produce the energetic extragalactic neutrinos likely trace the large-scale structure, so the diffuse astrophysical neutrino flux may exhibit anisotropy similar to other large-scale structure tracers though no anisotropy has been detected in the diffuse neutrino flux. Galaxies, detected in infrared observations, are well-suited to be used as tracers of large-scale structure. This thesis presents a two-point angular cross-correlation between IceCube neutrinos and an infrared galaxy catalog. This angular correlation required novel modifications to include the effects IceCube's declination and energy dependent effective area and point spread function while also accounting for multipole coupling caused by the use of a galactic plane mask. Despite improvements in the sensitivity to anisotropy, no statistically significant correlation was observed. The upper limit on the correlation strength is used to place constraints on the share of the diffuse neutrino flux that can be contributed from source correlated with the local large-scale structure. If the neutrino spectral energy distribution follows a power law with a spectral index held fixed to the diffuse muon neutrino measurement, the correlated sources can contribute no more than 54% of the diffuse muon neutrino flux. I also placed constraints on the evolution of neutrino sources with respect to redshift, assuming a parameterized model of neutrino source redshift evolution. The correlation upper limit rules out nearby source populations while allowing more distant evolution models, such as those tracing

the star-formation rate. The next generation of ice Cherenkov detectors such as IceCube Gen2 will be capable of constraining the correlation with three times the precision and potentially detecting anisotropy in the diffuse neutrino flux.

1 INTRODUCTION

Multi-messenger astrophysics is a growing field that offers surprising discoveries with every new observation. Within multi-messenger astrophysics, neutrino astronomy stands out for the difficulty of both performing observations and explaining the astrophysics that produce those observations. Despite the difficulty, the IceCube Neutrino Observatory has made numerous exciting discoveries. It has observed astrophysical neutrinos with an extragalactic origin from active galactic nuclei, neutrino emission from the Milky Way galactic plane, and a population of extragalactic energetic neutrinos from unresolved sources. The last in this list is called the diffuse neutrino flux. The diffuse neutrino flux appears to be the same in every direction in the sky. The isotropic distribution and the relatively few bright neutrino sources suggest that these neutrinos emerge from a large population of faint sources rather than a few bright sources. A few individual neutrino sources have been found; however, these sources are not sufficient to explain the isotropic astrophysical neutrino measurements. If astrophysical neutrino sources prove to be faint, then searches for individual point-like neutrino sources are unlikely to be fruitful. New methods must focus on explaining the diffuse astrophysical neutrino flux in terms of the aggregate properties of the ensemble of neutrino sources.

Unlike the apparent distribution of astrophysical neutrinos, the universe is not isotropic. The distribution of dark matter and baryonic matter in the universe follows a web-like structure caused by the evolution of primordial perturbations in these density fields from the early universe. Compact objects like galaxies form in dark matter overdensities like raindrops condensing within a cloud. At large scale, galaxies trace the underlying density structure. The production of high energy neutrinos requires an energetic environment which can only be found within compact objects where gravitational potential energy can be transformed into kinetic energy for particle acceleration; therefore, it is likely that neutrino emitters are also tracers of the large-scale structure. If the relationship between

the large-scale structure and astrophysical neutrinos can be quantified, it will provide insight into the identity of astrophysical neutrino sources.

This thesis presents a search for spatial correlations of the IceCube diffuse neutrino flux with a galaxy catalog derived from infrared observations. The results of the correlation analysis are used to constrain the contribution of correlated sources to the diffuse astrophysical neutrino flux and provide constraints on the distribution of neutrino sources with respect to redshift. Similar studies with future neutrino observatories will provide stronger constraints on the origin of astrophysical neutrinos.

This thesis is organized into seven chapters providing scientific context and a novel analysis of astrophysical neutrinos.

- Chapter 2 describes the current state of knowledge in multi-messenger astrophysics including neutrinos, cosmic rays, and γ-rays with particular emphasis on neutrino astronomy. The basic physics underlying the connection between astrophysical messengers is described and the observational status of each is discussed.

- Chapter 3 introduces the large-scale structure of the universe and the techniques used to describe anisotropies in the distribution of catalogs. The two-point correlation and cross-correlation functions are described within.

- Chapter 4 describes the IceCube Neutrino Observatory. The IceCube Neutrino Observatory has been operating successfully for more than a decade and has a sophisticated design and data processing pipeline. The physical and digital designs are described within.

- Chapter 5 introduces the cross-correlation analysis of IceCube neutrinos with tracers of large-scale structure. The analysis method, statistical implementation, and results are described.

- Chapter 6 discusses the astrophysical implications of the results found in Chapter 5. The constraints on the contribution of the correlated neutrino flux to the diffuse muon neutrino flux are reported. Constraints on the distribution of neutrino sources with respect to redshift are also presented.
- Chapter 7 presents the outlook for neutrino astronomy as a whole and the outlook for similar large-scale structure studies with future neutrino observatories.

2.1 Introduction

Astronomy has been practiced using light for millennia; however, the application of physical principles to explain astronomical observations began in earnest after the development of modern physics, particularly quantum physics and general relativity when atomic spectroscopy was applied to solar observations. Although electromagnetism traditionally was the only channel to observe astronomical phenomena, the full range of physical phenomena can occur in high energy astrophysical environments. The technology to observe such signals has not existed until recently. Multi-messenger astrophysics is the practice of using multiple channels to study astrophysical phenomena. The messengers that are of practical use today are electromagnetism, neutrinos, cosmic rays, and gravitational waves. Although gravitational waves are useful to study mergers of massive compact objects, they are not relevant to this work and will not be discussed further. A brief overview of relevant physics and observations of photons, neutrinos, and cosmic rays is presented below.

2.2 Photon and Neutrino Physics

Neutrino Physics

Neutrinos were first theorized by Wolfgang Pauli to explain momentum, energy, and angular momentum conservation in beta decays (Brown, 1978). Neutrinos participate in interactions governed by the weak force (Griffiths, 2011). There are three flavors of neutrinos corresponding to the three flavors of leptons, ie electron, muon, and tau neutrinos denoted by ν_e, ν_μ, and ν_τ. Neutrinos are extremely light; the upper limit on the neutrino mass is less than 0.120 eV based on direct measurements and cosmological constraints (Drexlin et al., 2013; Lesgourgues & Pastor, 2012). Because they are so light, they only interact imperceptibly with gravity. Neutrinos are electrically neutral, so they do not

participate in electromagnetic interactions. Similarly, they have no color charge, so they do not participate in strong interactions. As leptons, neutrinos do couple to the weak force. Any interaction involving neutrinos will conserve electric charge and lepton number.

Through the study of neutrino emission from fusion in the sun and fission reactor neutrino experiments, it was found that neutrino flavors can change. This phenomenon is called neutrino oscillation. Neutrino oscillation occurs because weak interactions occur in flavor eigenstates and neutrino propagation depends on the mass eigenstates. Neutrinos have the unusual property that the mass and flavor eigenstates are not the same; the measurements of mass and flavor are non-commutative. Like any unitary transformation, the mass eigenstates can be represented as a linear combination of flavor eigenstates. If the flavor states are represented by the index α and the mass states are represented by the letter i, then

$$|\nu_i\rangle = U_{i\alpha} |\nu_\alpha\rangle \tag{2.1}$$

where $U_{i\alpha}$ is a unitary matrix that describes the basis transformation. For three neutrino flavors, this matrix is called the Pontecorvo–Maki–Nakagawa–Sakata matrix or PNMS matrix. This matrix is usually parameterized in terms of "mixing angles,"

$$U_{i\alpha} = \begin{bmatrix} c_{12}c_{13} & s_{12}c_{13} & s_{13}e^{-i\delta} \\ -s_{12}c_{23} - c_{12}s_{23}s_{13}e^{i\delta} & c_{12}c_{23} - s_{12}s_{23}s_{13}e^{i\delta} & s_{23}c_{13} \\ s_{12}s_{23} - c_{12}c_{23}s_{13}e^{i\delta} & -c_{12}s_{23} - s_{12}c_{23}s_{13}e^{i\delta} & c_{23}c_{13} \end{bmatrix} \tag{2.2}$$

where $s_{ab} = \sin(\theta_{ab})$ and $c_{ab} = \cos(\theta_{ab})$. The phase δ is related to charge parity symmetry and is currently observationally consistent with zero. The time evolution operator is diagonal in the mass basis,

$$|\nu_j(t)\rangle \approx e^{-i\frac{m_j^2 Lc}{2E\hbar}} |\nu_j(0)\rangle \tag{2.3}$$

where L is the distance traveled by the neutrino. If a neutrino of flavor α propagates some distance, the transition probability is derived by writing the flavor eigenstate in terms of

its mass eigenstates and then applying the time evolution operator. The probability of measuring flavor β from a neutrino originally in the flavor eigenstate α is

$$P_{\alpha\to\beta} = \left|\sum_j U^*_{\alpha j} U_{\beta j} e^{-i\frac{m_j^2 Lc}{2E\hbar}}\right|. \tag{2.4}$$

Over astrophysically relevant distances, a neutrino beginning in a single flavor eigenstate will have approximately equal probability of being measured as any of the three flavors. In astrophysics, it is usually sufficient to assume that neutrinos are equally divided among the three flavor eigenstates.

Radiative Processes

Electrically charged particles can produce photons through numerous radiative channels. In classical electromagnetism, any charged particle that is accelerated will emit electromagnetic radiation. The radiated power is described by the Larmor formula,

$$P = \mu_0 \frac{q^2 a^2}{6\pi c} \tag{2.5}$$

where q is the particle charge, a^2 is the particle acceleration vector norm squared, and μ_0 is the vacuum permittivity. At high energy, the standard model predicts additional interaction channels including two-photon interactions. In various limits, radiative processes are given specific names. The radiative processes relevant to high-energy astrophysics or the detection of high-energy astrophysical particles are described below.

Thermal Radiation

An object with finite temperature emits electromagnetic radiation called thermal radiation. An idealized thermodynamic system called a blackbody assumes an opaque and non-reflective surface. In this case, the power of electromagnetic radiation is described by the

Stefan-Boltzmann Law

$$P = A\epsilon\sigma T^4 \tag{2.6}$$

where A is the blackbody surface area, ϵ is the emissivity, and σ is called the Stefen-Boltzmann constant, and T is the temperature (Rybicki & Lightman, 1985). The emissivity is equal to one in the ideal blackbody case, but it can be a function of frequency, ie. $0 \leq \epsilon(\nu) \leq 1$. The spectral energy distribution of blackbody radiation is described by the Planck spectrum,

$$I_\nu = \frac{2h\nu^3}{c^2}\frac{1}{e^{\frac{h\nu}{k_B T}} - 1} \tag{2.7}$$

or for wavelength

$$I_\lambda = \frac{2hc^2}{\lambda^5}\frac{1}{e^{\frac{hc}{\lambda k_B T}}}. \tag{2.8}$$

Wien's displacement law gives the peak of the blackbody radiation spectrum,

$$\lambda_{\text{peak}} = \frac{b_{\text{Wein}}}{T} \tag{2.9}$$

where b_{Wein} is the Wein's displacement law constant.

Thermal radiation is ubiquitous in astrophysics, but it is usually more complex than a simple blackbody spectrum. Most baryonic matter exists in a plasma state with internal degrees of freedom and non-trivial radiative transport. For example, stars emit continuum radiation which is approximately Planck distributed, but also feature emission and absorption lines. The continuum emission is due to the continuous energy states of free particles undergoing elastic scattering; this is sometimes called "free-free" emission caused by ionization and recombination of electrons and ions. Emission and absorption lines can occur when electrons transfer between energy levels ("bound-bound" emission or "absorption"). Other spectral features including sharp edges occur when atoms change ionization state (free-bound emission or absorption). When a plasma is transparent to its emission it is called optically thin. In this case, the radiated power is not determined by

Equation 2.6; instead the power depends on volume and density,

$$P = \Lambda(T) \int_V n_e^2 dV. \tag{2.10}$$

The volume integral over electron number density n_e defines the emission measure and $\Lambda(T)$ is the cooling function. The cooling function depends on the composition and temperature of the plasma.

Synchrotron Radiation

When a charged particle is deflected by a uniform magnetic field, it moves in a circular trajectory. The circular motion is an acceleration, so the charged particle will emit radiation (Jackson, 1999). This is called cyclotron radiation. The acceleration is $a = \frac{mv^2}{r}$, so the cyclotron power is

$$P = \frac{\sigma_T B^2 v^2}{c\mu_0} \tag{2.11}$$

where $\sigma_T = \frac{8\pi r_0^2}{3}$ is called the Thomson cross section. In the relativistic limit, this is called synchrotron radiation (Rybicki & Lightman, 1985). The power radiated becomes

$$P = \frac{4}{3}\sigma_T c\beta^2\gamma^2 U_B \tag{2.12}$$

where $\beta = \frac{v}{c}$, $\gamma = \frac{1}{\sqrt{1-\beta^2}}$, and $U_B = \frac{B^2}{8\pi}$.

In astrophysics, the observed emission is usually the aggregate emission from a large ensemble of charged particles. Often, the distribution of the energy of these particles can be described by a power law within some observable frequency range. If the energy distribution of charged particles is described by a power law $\frac{dN}{dE} \propto E^s$ for $s > 0$, the spectrum of synchrotron radiation will also follow a power law with $P(E) \propto E^p$. The spectral indices of the particle energy distribution s and the observed synchrotron radiation

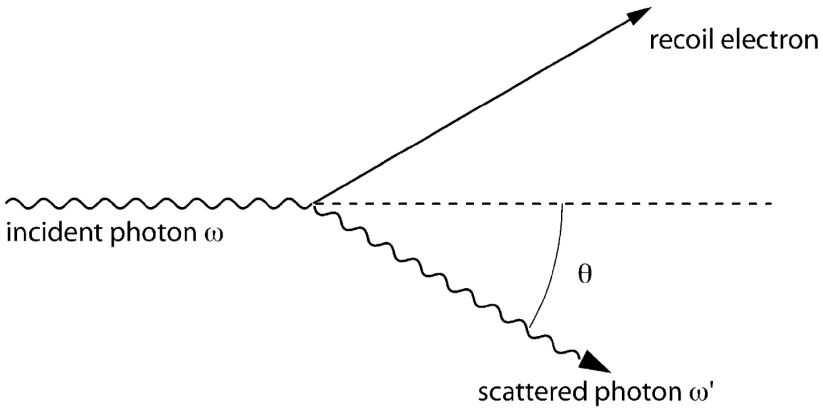

Figure 2.1: **Compton Scattering Diagram.** Figure reproduced from (Tavernier, 2010)

p are related by

$$s = \frac{p-1}{2} \tag{2.13}$$

For a single charged particle moving in a uniform magnetic field, the synchrotron radiation will be polarized in the plane of motion. In astrophysical contexts, the magnetic fields are often turbulent, and the observed synchrotron emission originates from a large ensemble of electrons propagating through the turbulent magnetic field. In this case, the polarization direction will average out to appear unpolarized. In some cases, the magnetic field may be well-ordered, and polarization can be observed.

Compton Scattering

Compton scattering occurs when a photon scatters elastically with a charged particle (Tavernier, 2010). In the process of scattering, the photon and electron exchange energy. The process is shown in Figure 2.1. The kinematics of Compton scattering can be derived with special relativity. If the incident photon has energy $E = \hbar\omega$ before scattering in the charged particle rest frame, the photon will have energy

$$E' = \frac{E}{1 + \frac{E}{mc^2}(1 - \cos(\theta))} \tag{2.14}$$

after scattering where θ is the angle that the charged particle recoils at relative to the initial photon momentum vector. The differential cross section for Compton scattering is described by the Klein-Nishina formula

$$\frac{d\sigma}{d\Omega} = \frac{1}{2}\left(\frac{E'}{E}\right)^2\left(\frac{E'}{E} + \frac{E}{E'} - \sin^2(\theta)\right) \tag{2.15}$$

At high energy ($E >> mc^2$ for the mass of the charged particle), the total cross-section becomes

$$\sigma = r_0^2\pi\frac{mc^2}{E}\left(\log\left(\frac{2E}{mc^2}\right) + \frac{1}{2}\right) \tag{2.16}$$

and the scattering tends to only deflect the photon by a small angle.

In the charged particle rest frame before scattering, the recoil electron will always receive energy from the photon. If the charged particle has a high speed relative to the observer, the photon may be boosted in energy by many orders of magnitude. This is referred to as inverse Compton scattering. In astrophysical contexts, inverse Compton scattering can occur when a cosmic microwave background photon Compton scatters with the hot plasma in a galaxy cluster, or when an infrared photon can scatter with a relativistic electron in an AGN jet where it can be boosted to become a TeV γ-ray. The observed spectrum of an ensemble of inverse Compton photons will depend on the underlying distribution of electrons and initial photon energies. For example, a far infrared thermal population of photons will be boosted to higher energies by a power law distribution of electrons as shown in Figure 2.2.

2.3 Cherenkov Radiation

Cherenkov radiation is light that is emitted when a charged particle propagates with a speed greater than the local speed of light in a polarizable material (Tavernier, 2010). The speed of light in a vacuum is 299,792,458 meters per second and is denoted by c. In a

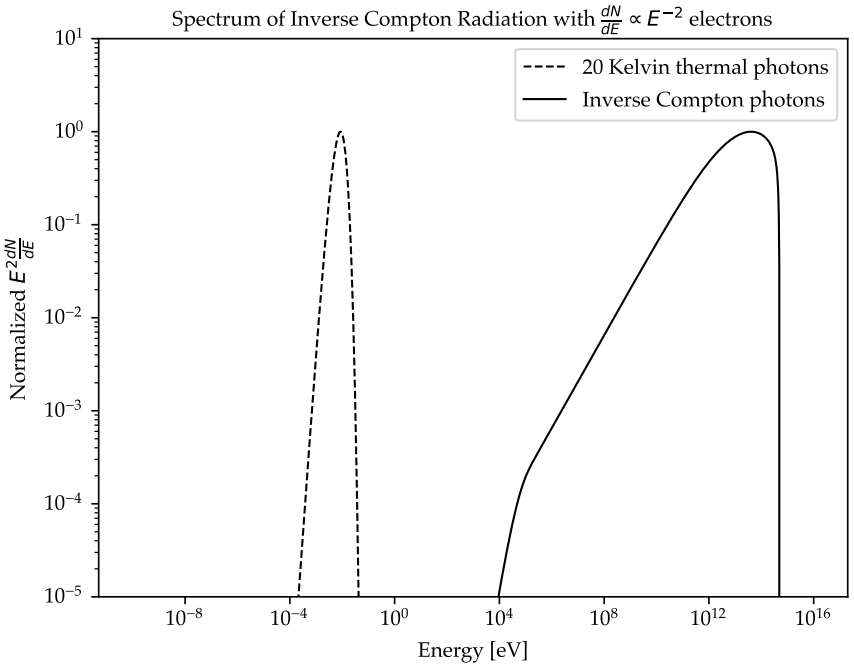

Figure 2.2: **Inverse Compton Scattering Energy Distribution.** The energy distribution of thermal photons with a 20 Kelvin temperature after inverse Compton scattering with an electron population following an energy distribution $\frac{dN}{dE} \propto E^{-2}$.

polarizable medium with refractive index n, the speed of light is $v = \frac{c}{n}$. Ice has a refractive index equal to 1.31 which corresponds to a speed of light equal to 228849204 meters per second or 76% the speed of light in vacuum. When a charged particle traverses a polarizable material, its electric field will slightly polarize the surrounding material. As the charged particle leaves, the material will return to its original unpolarized state. This process excites and relaxes a weak dipole electric field at each point in the material. This perturbation to the electric field propagates at the material speed of light. The propagation of these perturbations can be visualized with Huygens' principle as shown in Figure 2.3. If the particle moves more slowly than the material speed of light, the wavefronts will arrive at a distant observer with random phases and destructively interfere. If the particle moves faster than the material speed of light, the wavefronts will constructively interfere and create an observable light pulse.

The angle of the coherent wavefront with respect to the particle trajectory is called the

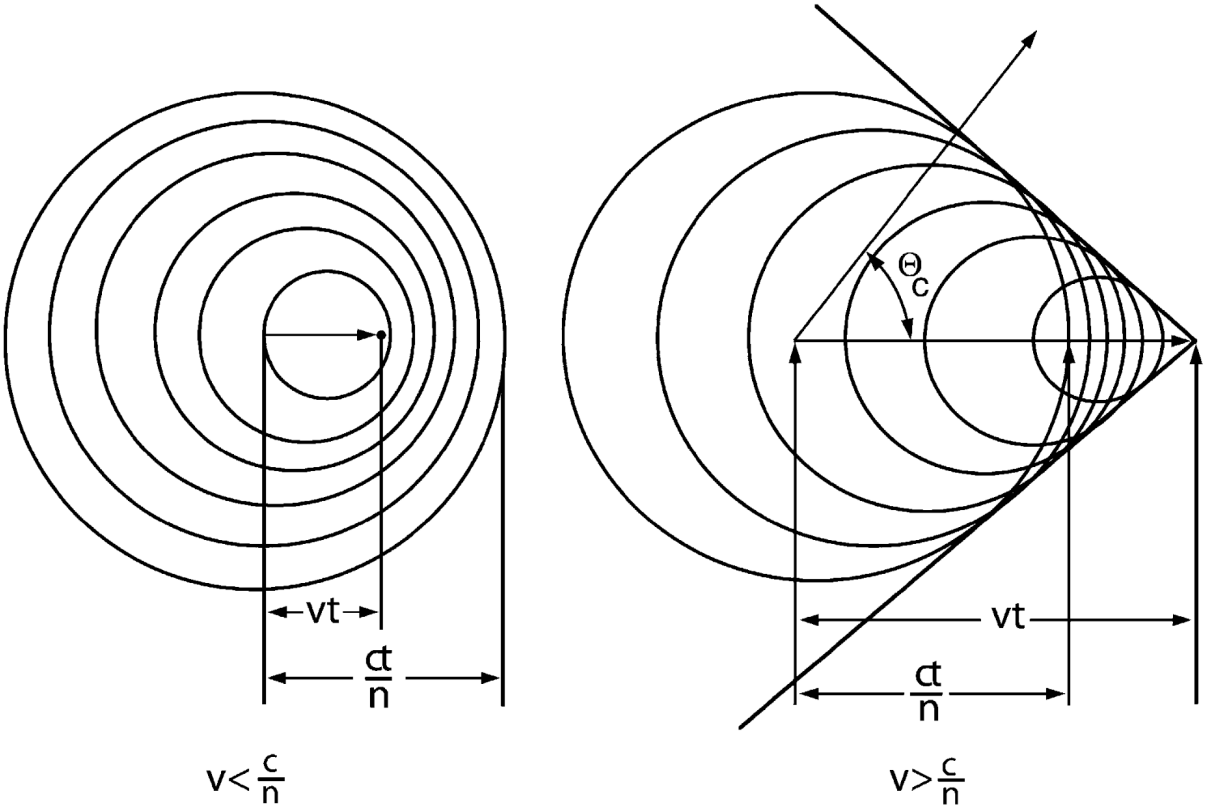

Figure 2.3: **Huygens' Principle for Cherenkov Radiation.** Wavefronts for electromagnetic perturbations from a particle moving below the material speed of light (left) and above the material speed of light (right) Tavernier (2010). Below the material speed of light, the wavefronts will arrive at an observer with a random phase and will deconstructively interfere. Above the material speed of light, the wavefronts will constructively interfere and be observable.

Cherenkov angle. It is defined by

$$\cos(\theta_c) = \frac{c}{nv}. \tag{2.17}$$

The differential intensity per unit frequency and track length is given by the Frank-Tamm formula

$$\frac{d^2E}{d\hbar\omega\, dx} = \hbar\omega \frac{Z^2\alpha}{\hbar c}\left(1 - \frac{c^2}{n^2v^2}\right). \tag{2.18}$$

Equation 2.18 shows that the energy flux increases linearly with frequency; however, the photon flux per unit frequency and track length is constant.

Hadronic Neutrino and γ-ray Production

Neutrinos and γ-rays can be produced in energetic astrophysical environments. High-energy astrophysical neutrino production is closely linked to γ-ray production through two primary processes. These processes are called pp and $p\gamma$ interactions. The details of these physical processes determine the ratio of neutrino emission to γ-ray emission.

pp Interactions

Proton-proton or pp interactions occur when an extremely energetic proton or nucleus collides with another proton or nucleus. This can occur in astrophysical environments where cosmic rays have recently been accelerated, but collide with the surrounding interstellar medium. An AGN, for example, may launch jets of energetic plasma into the surrounding interstellar medium. The interactions may produce charged or neutral pions which decay into muons, antimuons, and neutrinos (Kelner et al., 2006). The muons and antimuons further decay into electrons, positrons, and neutrinos, ie.

$$\begin{aligned} p + p &\rightarrow \pi^0 + X \\ p + p &\rightarrow \pi^+ + X \\ p + p &\rightarrow \pi^- + X \end{aligned} \tag{2.19}$$

where X can be a wide variety of hadrons. Neutral pions decay into two photons while charged pions decay into a neutrino and a lepton. The branching ratio for decay into a muon and muon neutrino is more than 0.999, but the decay can occasionally produce an electron and electron neutrino. The muon or antimuon decays into an electron, positron,

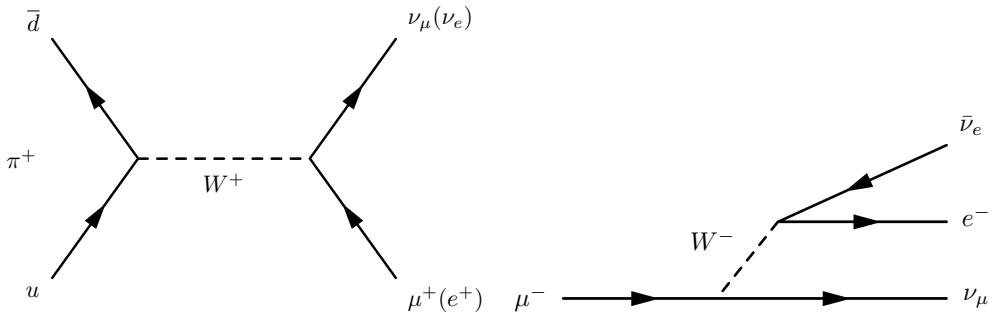

Figure 2.4: **Feynman diagrams for decay of π^+ and μ^-.** Left: Decay of π^+ into μ^+ or e^+ and ν_μ and ν_e. Right: A μ^- can decay into a W^- and ν_μ. The W^- decays into $\bar{\nu}^e$ and e^-. In both cases, charge conjugation can be applied to generate diagrams for π^0 and μ^+.

and neutrinos.

$$\begin{aligned}
\pi^0 &\rightarrow \gamma + \gamma \\
\pi^+ &\rightarrow \bar{\nu}_\mu + \mu^+ \\
&\rightarrow \bar{\nu}_\mu + e^+ + \nu_e + \bar{\nu}_\mu \\
\pi^- &\rightarrow \bar{\nu}_\mu + \mu^- \\
&\rightarrow \nu_\mu + e^- + \bar{\nu}_e + \nu_\mu
\end{aligned} \tag{2.20}$$

A Feynman diagram for the decay of muons is shown in Figure 2.4.

All varieties of pion (π^0, π^+, and π^-) are produced in approximately equal numbers, Equation 2.20 requires that the neutrino $\nu_e : \nu_\mu : \nu_\tau$ flavor ratio is $1 : 2 : 0$. By the time the neutrinos arrive at Earth, neutrino oscillations ensure an equal flavor ratio. Equation 2.20 also shows that there are three neutrinos and antineutrinos per γ-ray. As a rule of thumb, the neutrinos receive approximately 5% of the initial proton energy, and the γ-rays receive approximately 10% Kelner et al. (2006); Kelner & Aharonian (2008).

$p\gamma$ Interactions

Energetic protons can also interact with low energy photons through the Δ-resonance which decay into pions (Kelner & Aharonian, 2008). These interactions are called photomesonic

Name	Location	Energy Range	Reference
Pierre Auger Observatory	Argentina	$> 10^{17}$ eV	Góra et al. (2018)
Telescope Array	Utah	$> 1.6 \times 10^{18}$ eV	Abu-Zayyad et al. (2013)
HiRes	Utah	$> 10^{17}$ eV	Matthews & Jui (2000)
KASCADE	Germany	100 TeV - 80 PeV	Haungs et al. (2006)
Tibet ASγ	Tibet	1 TeV - 100 PeV	Amenomori et al. (2011)
IceTop	South Pole	1 PeV - 1 EeV	IceCube Collaboration et al. (2013)
AMS-02	Space	100 MeV - 1 TeV	Alekseev et al. (2017)
Pamela	Space	50 MeV - 100 GeV	Alekseev et al. (2017)

Table 2.1: **Cosmic Ray Observatories.** Cosmic ray observatories span 11 orders of magnitude in energy and use diverse detection technology. A few key experiments are summarized here.

interactions.

$$\begin{aligned} p + \gamma &\rightarrow \pi^0 + X \\ p + \gamma &\rightarrow \pi^+ + X \\ p + \gamma &\rightarrow \pi^- + X \end{aligned} \tag{2.21}$$

The pions decay through the same channels as described previously.

2.4 Cosmic Ray Astrophysics

Cosmic rays are charged protons and nuclei hurled through space by astrophysical particle accelerators, likely AGN. This section will outline observations of cosmic rays and present the theory that attempts to explain the observations.

Experimental Results

Cosmic rays have been observed using a variety of techniques through the 20th century and continue to be observed by increasingly large and sophisticated observatories. The particular detector technology used for observing cosmic rays depends on the energy and composition of interest.

Cosmic rays have been observed over many orders of magnitude in energy. The energy spectrum of cosmic rays over eleven orders of magnitude is shown in Figure 2.5. The cosmic ray energy spectrum has several notable features. The first is called the "knee". The knee is a spectral break at about a few PeV. Below the knee, the spectrum is slightly steeper than above the knee. Below the knee, the spectral index is -2.7, and above the knee, the spectrum steepens to -3.1. Above a few EeV, the spectrum has additional features. The cosmic ray flux drops significantly above a few EeV due to suppression by the Greisen–Zatsepin–Kuzmin effect (Greisen, 1966; Zatsepin & Kuz'min, 1966). This feature is commonly called the "ankle" The physical origins of the knee and the ankle are discussed in Section 2.4.

The composition of cosmic rays has also been measured by various experiments. The low energy cosmic ray composition was measured by HEAO-3 (Lund, 1984). The relative abundances are shown in Figure 2.6. HEAO-3 found that cosmic rays are dominated by single protons. Helium is the next most common, with a helium-to-proton ratio of 1:10. Heavier elements are much less common. Elements with even atomic numbers are slightly more stable than elements with odd atomic numbers, so they have a higher relative abundance. The cosmic ray composition is similar to the composition of local Galactic abundance; however, lithium, beryllium, and boron are overrepresented in cosmic rays. Heavier elements are also slightly more common in cosmic rays than in the local Galactic abundance. This suggests that there is a difference in the production or diffusion of heavier elements relative to lighter elements when they are accelerated to high energy. The large excess of lighter elements is due to spallation: collisions of energetic heavy elements with the colder interstellar medium. Spallation causes the heavy nucleii to fragment into lighter elements, so the abundance of lithium, berylium, and boron are depleted relative to the galactic average.

The Pierre Auger Collaboration reported the composition of cosmic rays at ultra-high-energy ($> 10^{17}$ eV) (Settimo et al., 2016). This measurement is based on the width of observed air showers caused by primary cosmic ray interaction with the Earth's atmosphere;

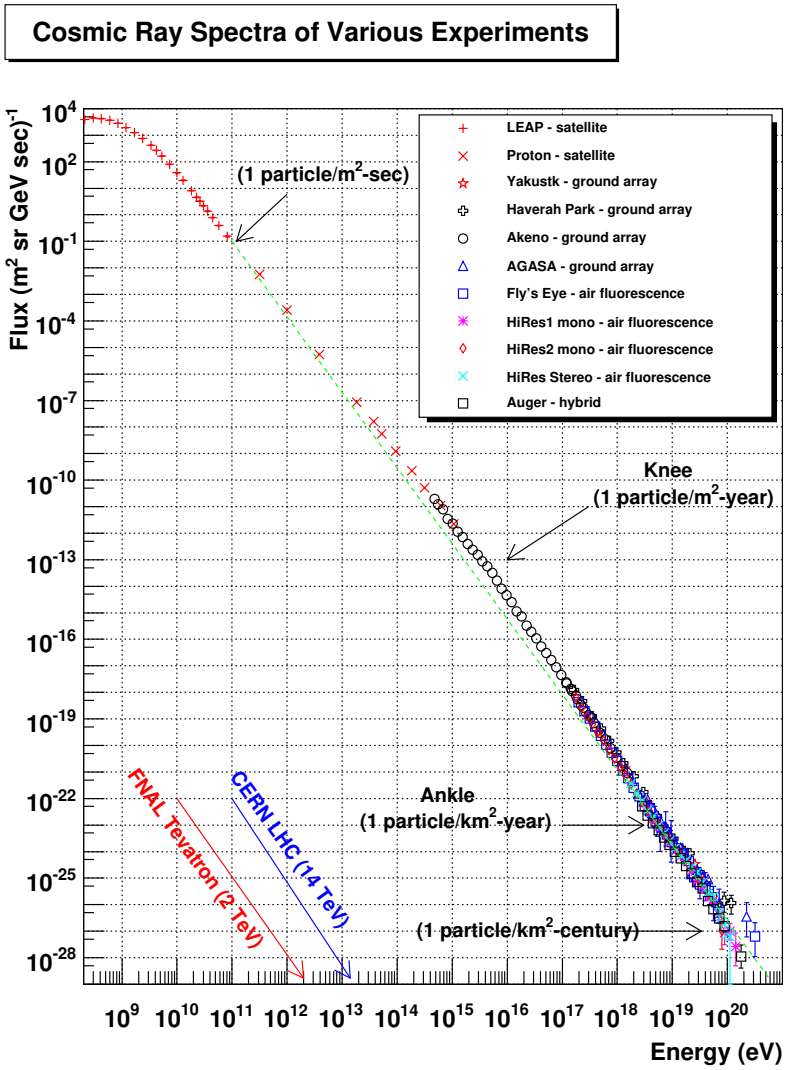

Figure 2.5: **Cosmic Ray Energy Spectrum.** The cosmic ray energy spectrum spans more than eleven orders of magnitude and is approximately a broken power law with a break at a few PeV. There is an additional spectral break at around 100 EeV. Figure produced by William Hanlon[1].

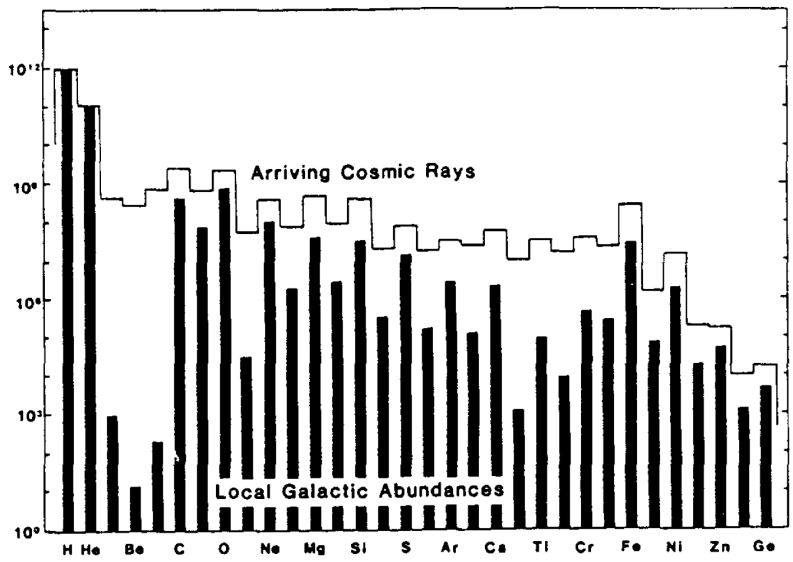

Figure 2.6: **Cosmic Ray Composition.** The composition of cosmic rays is somewhat different from the Galactic local average composition. Both are dominated by hydrogen and helium, but there is an excess of light elements in cosmic rays and an excess just below iron. Figure reproduced from Lund (1984)

they cannot resolve the element specifically but can estimate how the average shower width would look for pure hydrogen and pure iron cosmic rays. They found that the composition favors light elements at lower energy and becomes heavier at higher energy.

The spatial distribution of cosmic rays is of great interest for the potential to study the accelerators that produce energetic cosmic rays. At the GeV energy scale, cosmic rays propagate through the galaxy diffusively; they are strongly deflected by the galactic and solar system magnetic field. At the TeV to PeV energy scale, cosmic rays exhibit a weak dipole. At the ultra-high-energy scale, the Pierre Auger Collaboration has reported the discovery of a dipole in the distribution of cosmic rays (THE Pierre Auger Collaboration et al., 2017). At this energy, the cosmic rays are only weakly deflected by magnetic fields, so their trajectory can be used to identify cosmic ray accelerators. The Auger dipole points away from the galactic center, so it suggests an extragalactic origin. The strength of the dipole observed by Pierre Auger cannot be explained by known γ-ray sources alone (Partenheimer et al., 2024).

Theoretical Results

The physical processes that accelerate cosmic rays are poorly understood. The most popular acceleration theories are derived from work by Fermi. Fermi acceleration occurs when particles are propagating within a cloud with an inhomogeneous magnetic field. The inhomogeneities may act as magnetic mirrors which can scatter charged particles (Hooper, 2024). If the cosmic rays are scattered by an angle $\cos\theta < \frac{v_{CR}}{v_{\text{cloud}}}$, the cosmic ray will gain energy equal to

$$\frac{\Delta E}{E} = 2v_{\text{cloud}}v_{CR}\cos(\theta) + 2v_{\text{cloud}}. \tag{2.22}$$

Averaged over angle θ this is,

$$\left\langle \frac{\Delta E}{E} \right\rangle = \frac{8v_{\text{cloud}}^2}{3}. \tag{2.23}$$

If the scattering mirrors are assumed to be isotropically moving and the cosmic rays have interaction rate R and characteristic escape time τ, the number of cosmic rays per unit energy interval is

$$N(E) \propto E^{-1-\frac{3}{8v_{\text{cloud}}^2 R\tau}} \tag{2.24}$$

which is second order in the cloud velocity. This kind of acceleration is usually called second-order Fermi acceleration for this reason. The power law spectrum is required to explain the observed cosmic ray energy distribution. Second-order Fermi acceleration is not efficient enough to explain the large cosmic ray flux at Earth.

The acceleration can be much more efficient when the scatterers are not isotropically distributed. First order Fermi acceleration occurs when the scatterers are preferentially moving toward the cosmic rays or equivalently, the cosmic rays moving toward the shock are efficiently accelerated. This can occur in astrophysical environments where a shock wave collides with surrounding interstellar gas like in a supernova remnant. In this case,

the angle-averaged fractional energy gain is

$$\left\langle \frac{\Delta E}{E} \right\rangle = \frac{4 v_{\text{shock}}}{3} \tag{2.25}$$

where v_{shock} is the velocity of the shock wave. This first-order process can accelerate cosmic rays much more efficiently than second-order Fermi acceleration, so sites of directional flows can accelerate cosmic rays to higher energy.

Acceleration sites are limited by the physical size and magnetic containment of an astrophysical object. Hillas (1984) provides a useful criterion for the candidate sites of cosmic ray acceleration. The Hillas criterion describes the constraint that, under an acceleration process resembling Fermi acceleration, the cosmic rays must be contained by the magnetic field inside a source with a typical radius size until the cosmic rays are accelerated to sufficiently high energy that they escape. The Larmor radius is a useful measure of magnetic containment. When the Larmor radius of a charged particle exceeds the physical size of the acceleration site, the cosmic rays can escape. A charged particle in a uniform magnetic field will undergo circular motion with a radius determined by the particle mass, velocity, and charge.

$$r = \frac{\gamma m v}{|q| B} = 1.08 \left(\frac{E}{10^{15}\ \text{eV}} \right) \left(\frac{B}{\mu\text{G}} \right)^{-1} z^{-1}\ \text{pc} \tag{2.26}$$

where B is the magnetic field strength, γ is the Lorentz factor, and z is the atomic number. The magnetic field in astrophysical environments is typically turbulent, but the Larmor radius is a reasonable approximation to the length scales where diffusion is suppressed. In other words, a particle with energy less than E can be contained in a radius determined by Equation 2.26. The Hillas criterion is a necessary but not sufficient condition; sufficient energy within the astrophysical environment must be available to produce energetic shocks where Fermi acceleration can occur.

The Hillas criterion can also be used to explain the spectral break at the "knee." Rear-

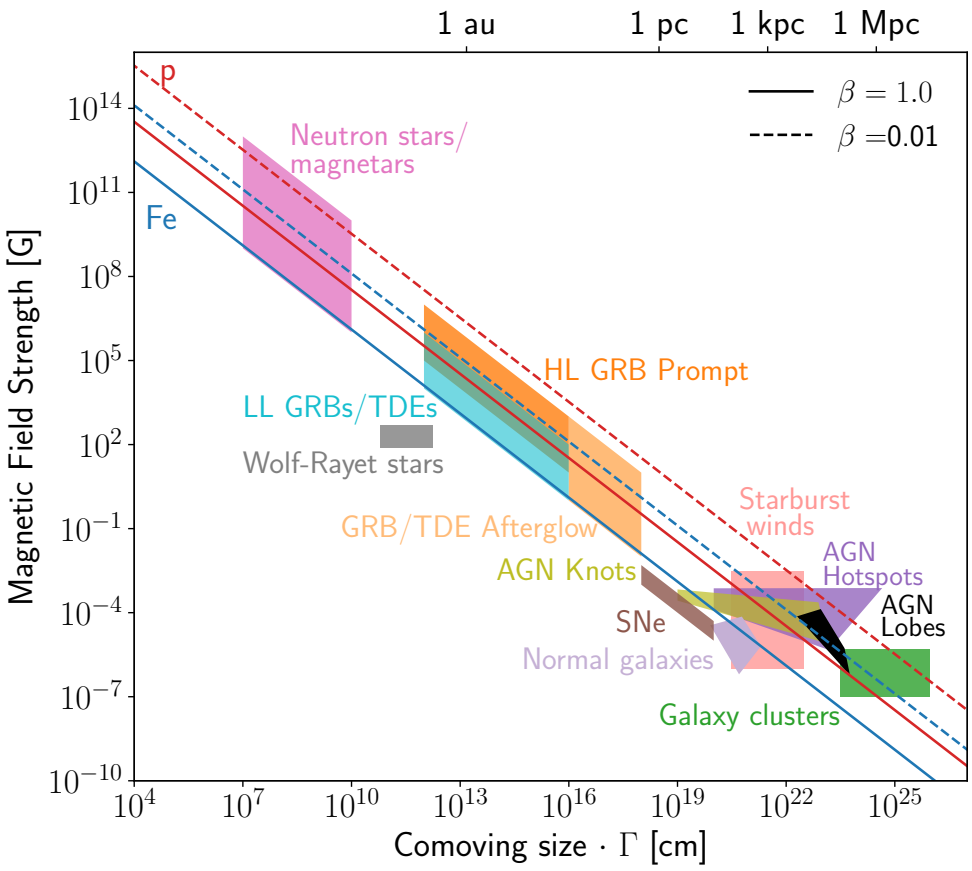

Figure 2.7: **Hillas Criterion for Cosmic Ray Source Candidates.** The Hillas Criterion defines the relationship between magnetic field strength and physical size of cosmic ray accelerator candidates if cosmic rays are accelerated by a Fermi-like acceleration process. The blue and red lines correspond to proton and iron nucleus acceleration up to 10^{20} eV. β refers to the speed of outflows where acceleration occurs. Figure reproduced from Alves Batista et al. (2019)

ranging Equation 2.26,

$$E = 1.08 \left(\frac{r}{\text{pc}}\right) \left(\frac{B}{\mu\text{G}}\right)^{-1} z^{-1}\ 10^{15}\ \text{eV}. \tag{2.27}$$

The thickness of the Milky Way disk is approximately 300 pc thick and the average magnetic field strength is approximately 10μG. Protons with energy above 32 PeV and iron nuclei with energy above 1.2 PeV cannot be magnetically confined in the Milky Way disk where they could propagate diffusively to Earth. Instead, they may escape into intergalactic

space. In this scenario, the spectral break would represent a transition from cosmic rays accelerated within the galaxy to those produced extragalactically. The spectral shape will be smoothed around the knee depending on the composition of galactic cosmic rays.

It is also possible that cosmic rays with energy above a few PeV are simply not accelerated in the Milky Way. There are few sources energetic enough to accelerate cosmic rays to super-PeV energy. These sources, called PeVatrons, are rare in the Milky Way; however, there is evidence for PeV cosmic acceleration in a few galactic Galactic sources. These include:

- **Supernova remnants:** Supernova remnants are expected to contribute a dominant fraction of lower energy cosmic rays; however, PeV cosmic ray acceleration in supernova remnants is rare. Particle acceleration may occur when the supernova remnant winds collide with the surrounding interstellar medium. These shock waves form an environment where diffusive shock acceleration can occur. Fang et al. (2022) found evidence for PeV cosmic ray acceleration in one particular supernova remnant. Whether there is a dominant population of PeVatron supernova remnants is unknown.

- **Star-forming regions:** Regions where intense star formation has recently occurred can also be conducive to diffusive shock acceleration. Massive stars produce strong winds. If the star-forming region is compact enough, the winds from many stars can collide and produce a labyrinth of overlapping shock fronts. Cosmic rays can bounce from one shock front to another many times before escaping. PeV cosmic ray production has been observed in one particular star-forming region called the Cygnus Cocoon (Ackermann et al., 2011; Abeysekara et al., 2021; Astiasarain et al., 2023). X-ray observations have also been performed to rule out leptonic γ-ray emission in such PeVatrons (Mizuno et al., 2015; Guevel et al., 2023).

- **The Galactic Center:** The Galactic Center is also the host of PeV cosmic ray production. γ-ray observations from HESS and HAWC found 100 TeV emission suggesting the

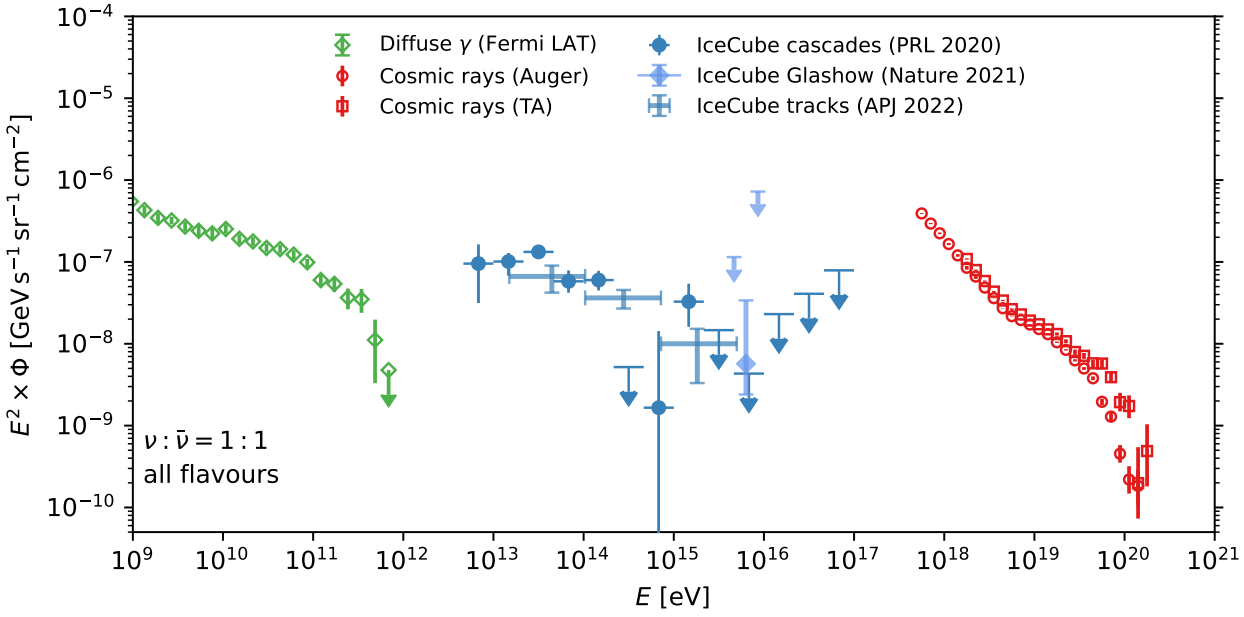

Figure 2.8: **Diffuse Multi-Messenger Spectral Energy Distribution.** The energy flux of the unresolved background of cosmic rays, γ-rays , and neutrinos. The energy flux of these messengers is similar despite the large difference in messenger energy suggesting a link between the physical processes that produce them.

presence of 1 PeV cosmic rays (HESS Collaboration et al., 2016; Albert et al., 2024). Contemporary or relic outflows from the Milky Way central black hole into a dense molecular cloud may be responsible for the γ-ray emission. Although the Milky Way black hole is quiescent now, it had active outflows in the past (Sarkar, 2024).

2.5 γ-ray Astrophysics

Traditional electromagnetic astronomy is such a colossal topic that it would constitute multiple theses to scratch the surface. This section will be restricted to electromagnetic high-energy astrophysics as it relates to multimessenger astrophysics. Typically this involves energies greater than 1 GeV but also includes non-thermal radiation in radio and X-ray wavelengths.

The study of high-energy astrophysics began at low frequency. Karl Jansky discovered

radio emission from the galactic center in the 1930s from synchrotron radiation of relativistic electrons in the environment surrounding the black hole at the center of the Milky Way (Jansky, 1935). Recently, the Event Horizon Telescope captured images of Sag A* (Event Horizon Telescope Collaboration, 2022). Both of these images have shown that the environments surrounding supermassive black holes are extremely energetic and have the potential to produce γ-rays , neutrinos, and cosmic rays.

γ-rays and X-rays are attenuated by the Earth's atmosphere, so they must be observed at high altitudes. The first astrophysical X-ray sources were X-ray binaries. The X-ray emission in this case was produced by the thermal emission from a hot accretion disk surrounding neutron stars and black holes. Non-thermal X-ray emission can also be produced by relativistic electrons undergoing synchrotron radiation. The combination of X-ray and radio emission can be a powerful tool for constraining electron populations in an astrophysical environment. γ-rays were first discovered by high-altitude balloons that were searching for γ-ray emission from nuclear weapons testing. These missions found several bright γ-ray sources including the Geminga pulsar. γ-ray emission is ubiquitous in energetic astrophysical environments including active galactic nuclei, neutron star and black hole mergers, supernovae, novae, and supernova remnants.

2.6 Neutrino Astrophysics

Astrophysical neutrinos have only recently been discovered. This section will describe observations of astrophysical neutrino sources starting with the sun and continuing to more energetic and distant sources.

Solar Neutrinos

In the 1960's it was known that the sun was powered by nuclear fusion. This was known from optical spectroscopic observations showing a large concentration of helium in the sun.

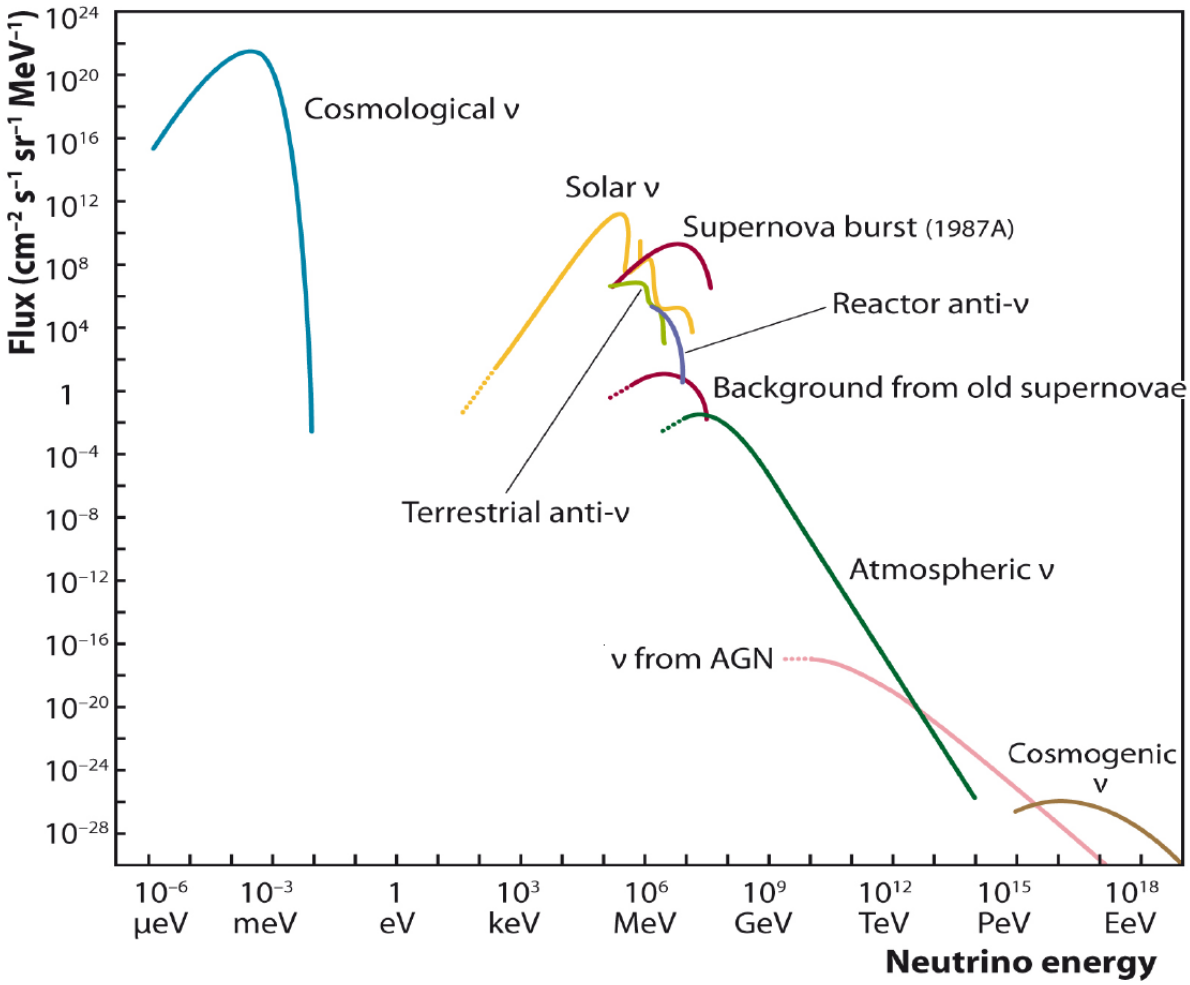

Figure 2.9: **Neutrino Emission from Astrophysical and Anthropogenic Sources.** Astrophysical and anthropogenic neutrinos span a large energy range. The flux falls rapidly at higher energy requiring increasingly large detectors. Figure reproduced from Spiering (2012).

Nuclear fusion will necessarily produce neutrinos, so physicists began to search for these neutrinos. The Homestake experiment was a neutrino detection experiment designed to detect these solar neutrinos. The experiment did detect solar neutrinos, but found that the flux was less than one third of the theoretical prediction based on the optical luminosity of the sun. It was discovered decades later that neutrinos can oscillate between flavors which explained the deficit of neutrinos observed in the Homestake experiment. The Homestake experiment had only observed electron neutrinos.

SN 1987A

Neutrino astronomy burst into the scientific world with the detection of neutrinos from a nearby supernova (Arnett et al., 1989). On February 24, 1987, a new supernova was discovered in the Large Magellanic Cloud. This was the nearest supernova since the Kepler's supernova in 1604. The availability of modern astronomical observatories made this event a unique opportunity to study the details of the supernova explosion and evolution into a supernova remnant. An extensive observing campaign was undertaken across the electromagnetic spectrum. After an archival search, neutrino emission was observed in the hours preceding the detection of visible light (Hirata et al., 1987; Bionta et al., 1987).

SN 1987A was a core-collapse supernova; core-collapse occurs when the nuclear fusion is unable to oppose the gravitational pressure of the star's mass. The catastrophic collapse occurs rapidly, increasing the pressure in the star's core. The innermost volume of the star may form a neutron star or collapse into a black hole. An outwardly propagating shockwave will form when the stellar material collides with the surface of the neutron star. As the shockwave forms, the highest temperatures and pressures are reached. At such high temperatures, neutrinos and antineutrinos are formed through thermal emission and electron capture. The neutrinos carry up to 10^{46} J or approximately 10% of the stellar mass. As the shockwave propagates outward, the material becomes less dense and eventually becomes optically thin to visible light.

TXS 0506+056

On September 22, 2018, the IceCube Collaboration reported a high-energy muon neutrino with energy estimated to be 290 TeV and automatically distributed a real-time alert to the astronomical community (The IceCube Collaboration et al., 2018). The Fermi γ-ray observatory followed up on the IceCube alert. The Fermi-LAT telescope detected a γ-ray flare from a known γ-ray blazar called TXS 0506+056. Blazars are a class of active galactic nuclei where the AGN jet is oriented face toward Earth. The spectral energy distribution of

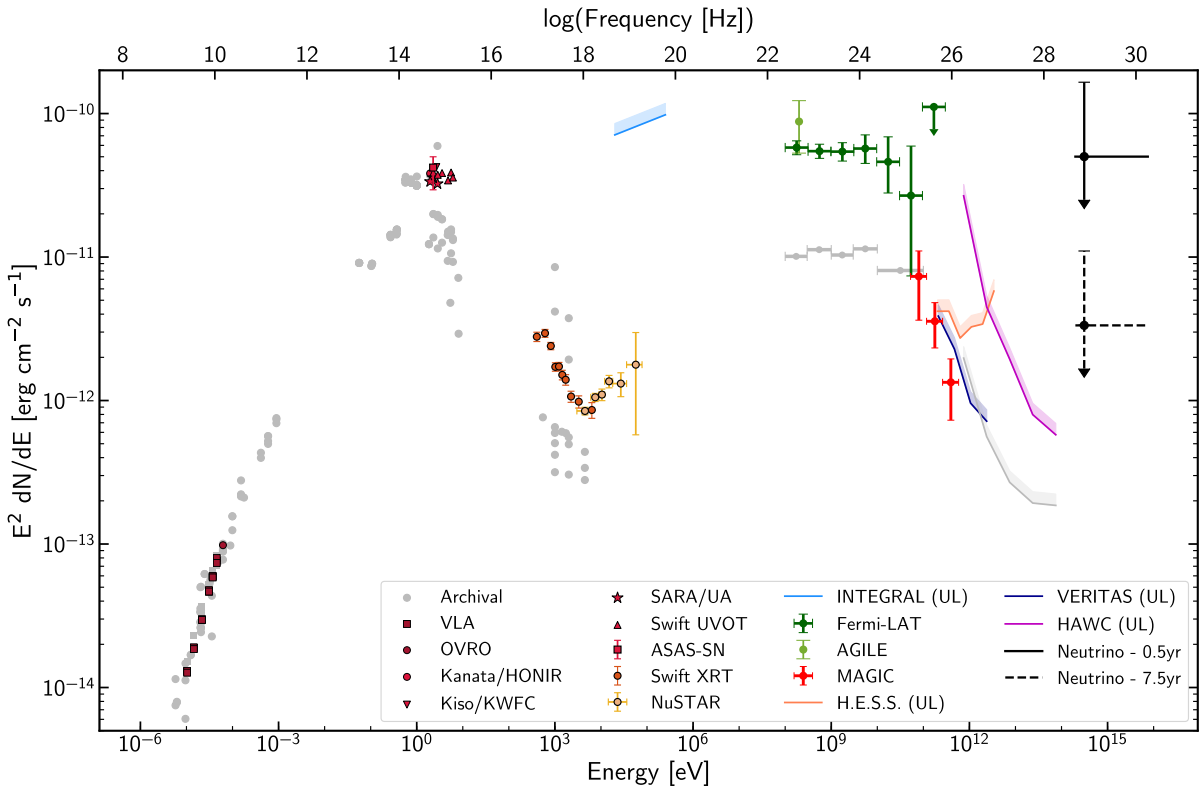

Figure 2.10: **TXS 0506+056 Spectral Energy Distribution.** The high energy neutrino event IC 170922A triggered an extensive multi-wavelength followup. The spectral energy distribution shows the typical two-humped shape indicating the presence of synchrotron and inverse Compton radiation from a population of relativistic electrons. Upper limits on neutrino emission from IceCube demonstrate the likelihood of detecting one event lice IC170922A every 0.5 years and 7.5 years. Figure reproduced from The IceCube Collaboration et al. (2018).

electromagnetic emission from blazars is characterized by a smooth spectrum featuring two broad peaks. The first is due to synchrotron radiation of freshly accelerated charged particles, primarily electrons, oscillating in the interstellar magnetic field. The synchrotron component usually peaks in optical, UV, or even X-ray wavelengths but is also detectible in radio wavelengths. The higher energy component is usually attributed to inverse Compton scattering of the same relativistic electrons that produce the synchrotron radiation. The electrons scatter lower energy, likely infrared, photons and boost them up to γ-ray energy. If there is significant proton or nucleus acceleration with the AGN jets, these hadrons can

produce neutrinos through pp or $p\gamma$ interactions.

The neutrino event and association of the neutrino with an astrophysical source triggered an intense follow-up campaign from experiments across the electromagnetic spectrum.

- Very-high-energy γ-rays: The HESS, Veritas, and MAGIC observatories, all imaging atmospheric Cherenkov Telescopes which are sensitive to TeV-energy photons, observed emission elevated by five times relative to the quiescent state of TXS 0506+506 The air shower water Cherenkov observatory HAWC placed an upper limit on photons with energy up to 100 TeV.

- High-energy γ rays: Fermi-LAT and AGILE observed elevated GeV emission around the time of the neutrino detection. The flux increased by a similar factor as the very-high-energy emission.

- X-rays: The Swift observatory detected soft X-ray emission $(0.3$ keV - 10 keV$)$ with a falling spectrum indicating that the soft X-rays are produced by synchrotron radiation. The hard X-ray emission observed by NuStar transitions to a rising spectrum indicating that those X-rays are the low energy tail of the inverse Compton scattering.

- Optical: Numerous telescopes observed TXS 0506+056 during the observing campaign. They identified elevated visible light relative to the quiescent state. This light is produced by synchrotron radiation rather than thermal radiation.

- Radio: The Karl G. Jansky Very Large Array and Owens Valley Radio Observatory both observed TXS 0506+056 during the flare period and the quiescent state. OVRO observed a gradual increase in radio emission in the 18 months before IC170922A. Emission before the eruption may suggest a build-up of material in the blazar accretion disk which may accrete in one single lump causing the outburst.

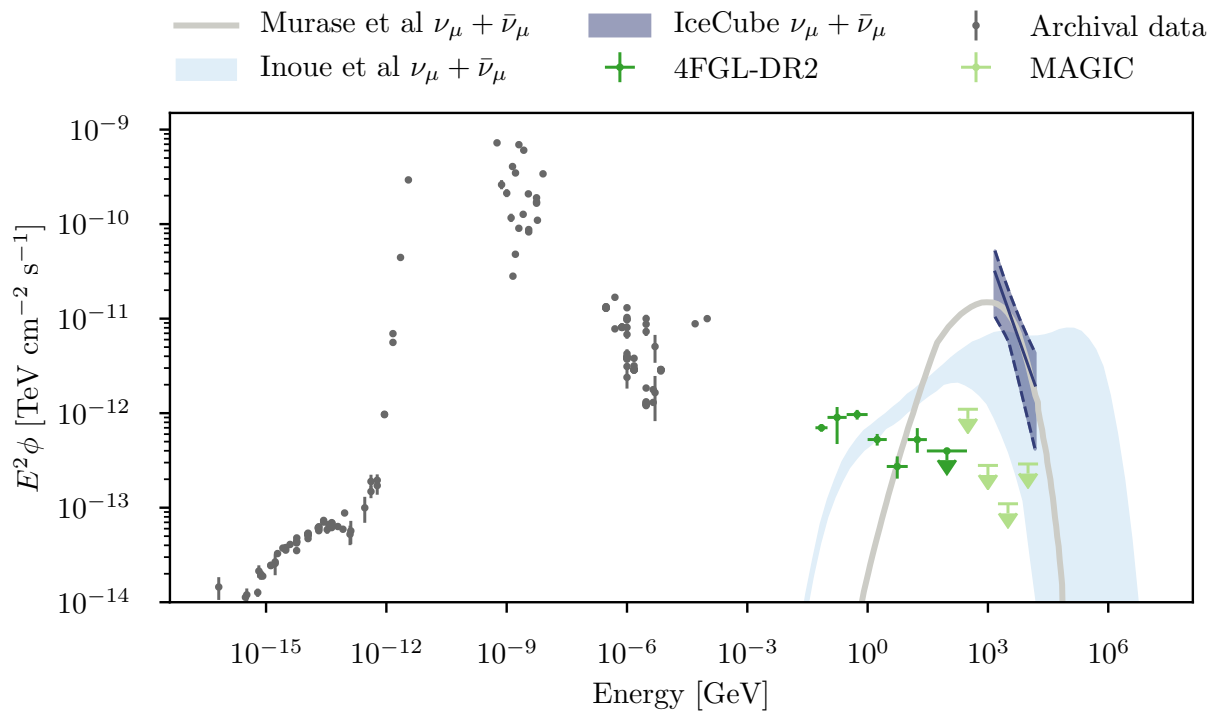

Figure 2.11: **NGC 1068 Spectral Energy Distribution.** The multi-messenger spectral energy distribution of NGC 1068 shows neutrino emission two orders of magnitude greater than γ-ray emission at similar energy. The correspondence between neutrino and γ-ray emission described earlier in this chapter requires the neutrino production site to be opaque to γ-ray emission. Figure reproduced from IceCube Collaboration et al. (2022a).

These observations are shown in Figure 2.10. The multi-wavelength observing campaign showed variability on time scales of a few days indicating a shift of synchrotron radiation to higher energy. The presence of neutrino emission indicates that there is a hadronic cosmic ray acceleration occurring within the AGN jets. A follow-up study of archival IceCube data found two neutrino flares of moderate statistical significance in September 2014 and March 2015 suggesting temporal variability is common.

NGC 1068

NGC 1068, also known as M77, is a well-studied Seyfert galaxy that has a high rate of star formation. The IceCube Collaboration performed a catalog search for neutrino emission

from 110 known γ-ray sources including NGC 1068 which was found to be a point source of neutrinos with a significance of 4.2σ after correcting for multiple hypothesis testing (IceCube Collaboration et al., 2022a). The best fit spectrum is softer than TXS 0506+056. The neutrino emission is attributed to hadronic interactions of freshly accelerated cosmic rays. The exact site of acceleration cannot be resolved by IceCube, but it must be an extremely energetic environment. The AGN jet or star-forming environments are proposed acceleration sites.

Whether the neutrinos are generated through pp or $p\gamma$ interactions, the neutrino emission is brighter than what would be expected based on the TeV γ-ray upper limits. The TeV γ-ray flux is expected to be similar to the neutrino emission. This is not seen in NGC 1068. This can be explained by a neutrino production site which is opaque to higher energy γ-rays. GeV γ-rays may undergo Compton scattering with surrounding electrons or pair production with lower energy photons in the intense radiation fields near the central engines (Fang et al., 2023). In either case, MeV energy γ-rays may escape and be observed by future telescopes such as the Compton Spectrometer and Imager.

Milky Way Galaxy

The IceCube Collaboration has observed neutrinos from the Milky Galaxy galactic plane (IceCube Collaboration et al., 2023). The Milky Way is a spiral galaxy mostly composed of stars and diffuse plasma in a disk that is gravitationally bound to the galaxy but is too warm to collapse into stars. The Earth lies in this disk. The diffuse plasma has been observed in γ-rays by Fermi-LAT (Ackermann et al., 2012). One explanation for the diffuse γ-ray emission is that ultra-high-energy cosmic rays collide with the diffuse plasma in the Milky Way disk and undergo pp interactions. If this is correct, then there will also be neutrino emission following a similar distribution spatial distribution.

The IceCube Collaboration performed a template-based search for neutrinos using a set of events with cascade-like morphology (IceCube Collaboration et al., 2023). Three

templates for diffuse galactic neutrino emission have been proposed based on γ-ray observations from Fermi-LAT (Gaggero et al., 2015). The resulting significance map is shown in Figure 2.12.

1. Π^0 Model: This template assumes the MeV-GeV π^0 decay follows a power law distribution in photon energy assuming the spectrum behaves like $E^{-2.7}$. The spatial part of this template is created by modeling the diffusion of cosmic rays through the galactic disk.

2. KRA-γ with 5 PeV Cutoff Model: This template allows the spectrum to vary as a function of position and assumes a 5 PeV cutoff in the neutrino energy distribution. The spatial distribution traces the Fermi diffuse galactic emission.

3. KRA-γ with 50 PeV Cutoff Model: This template is the same as the previous one but extends the neutrino spectrum up to 50 PeV.

The most significant detection was found for the KRAγ template with a 4.71σ result before correction for multiple trials correction. This suggests that there is significant neutrino emission from the galactic plane; however, the neutrino emission could also be from individual point sources rather than truly diffuse emission. The IceCube Collaboration tested catalogs of pulsar wind nebulae, supernova remnants, and unidentified γ-ray sources. No significant result was found. A template based on the Fermi bubbles was also tested and was not found significantly (Su et al., 2010).

Diffuse Neutrino Flux

The IceCube Collaboration has also discovered a population of neutrinos that have not been attributed to specific sources (IceCube Collaboration et al., 2020, 2024). The ensemble of TeV to PeV neutrinos from unknown sources is called the diffuse neutrino flux. This diffuse neutrino emission is thought to be produced by specific neutrino sources below the IceCube detection threshold rather than a truly diffuse process. The diffuse neutrino

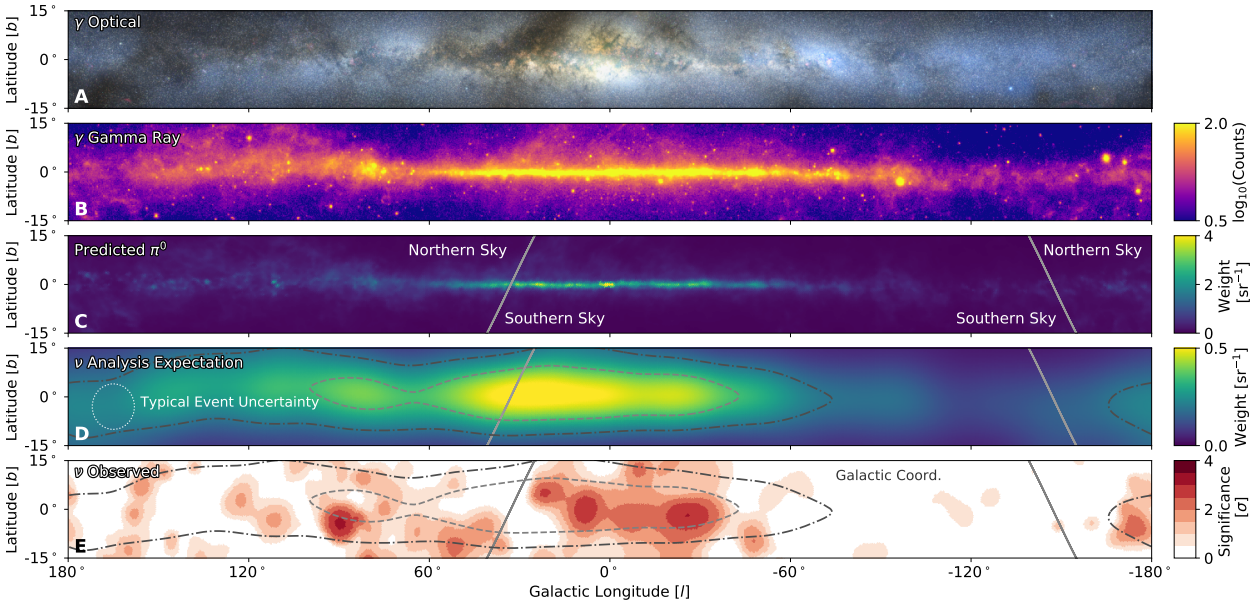

Figure 2.12: **Multi-Messenger View of the Galactic Plane.** Multi-Messenger observations of the Milky Way Galactic Plane. In descending order: (1) visible light from stars with the darker regions indicating dust obscuration; (2) diffuse γ-ray observations from Fermi-LAT; (3) model prediction for neutrino emission; (4) model prediction for neutrino emission after accounting for the IceCube effective area and angular resolution; (5) Observed neutrino map in units of statistical significance above background. Figure reproduced from IceCube Collaboration et al. (2023).

flux has been observed in both track events and cascade events. The fluxes measured from the two distinct event morphologies suggest that the flavor ratio is 1:1:1 as expected from distant astrophysical sources due to neutrino oscillation over astrophysical distances.

The distribution of diffuse neutrino flux energy is generally consistent with a power law,

$$\frac{dN}{dE} = \Phi_0 \left(\frac{E}{E_0}\right)^{\gamma} \tag{2.28}$$

A power law energy distribution is predicted by the Fermi acceleration process. The results for single power law fits are summarized in Table 2.6. These statistical constraints on the fit parameters are shown in Figure 2.13.

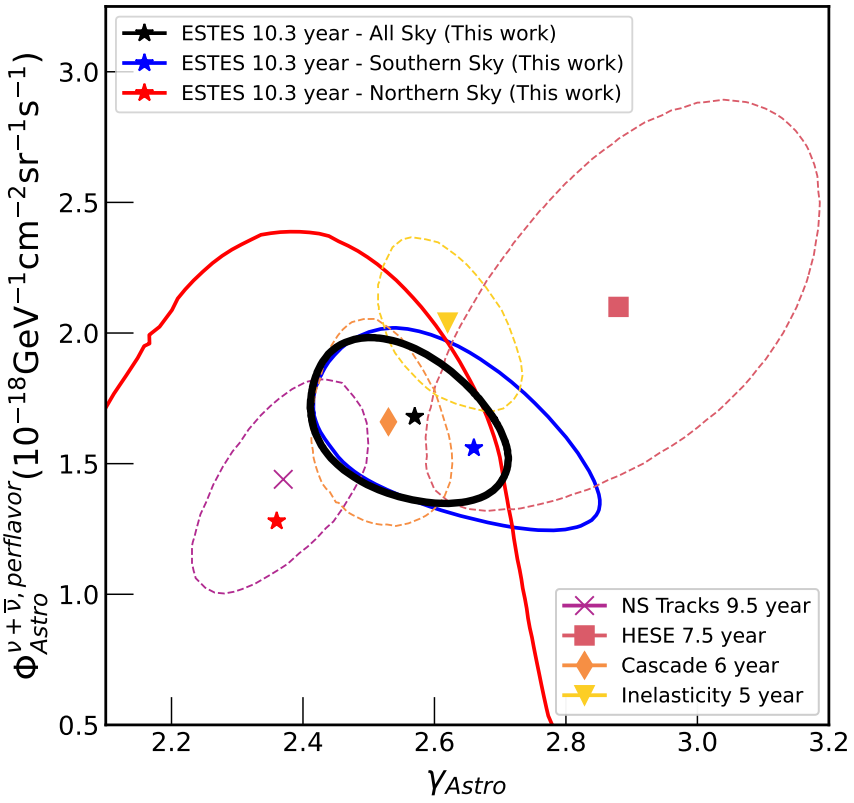

Figure 2.13: **Diffuse Neutrino Flux Power Law Measurements.** The spectral energy distribution of diffuse astrophysical neutrino flux is shown above. The fits are assumed to be single power-laws. Figure reproduced from IceCube Collaboration et al. (2024).

Data set	Φ_{astro} $\text{GeV}^{-1}\ \text{cm}^{-2}\ \text{s}^{-1}\ \text{sr}^{-1}$	γ_{astro}	E_{min} TeV	E_{max} TeV	Reference
ESTES 10.3 yr	1.68	2.58	3	550	IceCube Collaboration et al. (2024)
HESE 7.5 yr	2.12	2.87	60	3000	IceCube Collaboration et al. (2021)
Cascades 6 yr	1.66	2.53	16	2600	IceCube Collaboration et al. (2020)
Tracks 9.5 yr	1.44	2.37	15	5000	IceCube Collaboration et al. (2022b)
Inelasticity 5 yr	2.04	2.62	3.5	2600	IceCube Collaboration et al. (2019)

Table 2.2: **Diffuse Neutrino Single Power Law Measurements from IceCube.**

2.7 Summary

Multi-messenger astrophysics is a relatively new field that combines information from channels other than electromagnetism to reveal the full range of physical processes involved in astrophysical environments. The relevant interactions and radiative processes include thermal radiation, Compton scattering, pp interactions, and $p\gamma$ interactions. Cosmic rays were the first messenger to be studied but are challenging to associate with individual sources because they are deflected by magnetic fields. Neutrinos are produced in hadronic interactions in astrophysical environments. Astrophysical neutrinos have been measured from an unresolved population of faint sources and a few bright sources. These few bright sources are both active galactic nuclei, and it is thought that the remainder of the diffuse neutrinos are from faint AGN.

3 THE LARGE-SCALE STRUCTURE

3.1 Introduction

Measuring the anisotropy of various astrophysical fields is a major focus in cosmology. Anisotropy can be directly linked to different theoretical models in cosmology, so the observed anisotropy in a catalog can be used to infer the physical laws and dynamical history of the universe. For example, the cosmic microwave background was produced when the universe became transparent to light after the era of recombination. The degree of anisotropy observed in the cosmic microwave background is a direct tracer of the mass distribution at that time. Quantifying anisotropy is commonly done using two-point correlation functions. In this chapter, the Euclidean two-point correlation function will be introduced followed by the angular two-point correlation and angular two-point cross correlation.

3.2 Two-Point Correlations

The two-point correlation function is a measure of the clumpiness of a field, or equivalently, the clustering of a catalog. A field can be defined in Euclidean space or on a sphere, but similar tools can be used in each case.

Euclidean Two-Point Correlation

The two-point correlation (properly called the two-point autocorrelation) is used to quantify the measure the degree of clustering in an set of objects or continuous fields(Peebles, 1980). This section will follow the formalism for fields because point-like catalogs are usually binned into spatial pixels which are estimates of the underlying density field.

In Euclidean space, a field is defined as a mapping from space to real numbers,

$$f : \mathbb{R}^n \to \mathbb{R}. \tag{3.1}$$

This field can represent any quantity but is often an estimation of the density of galaxies observed in a survey. The correlation function of a field is defined as the product of the field value at points $\vec{x}$ and $\vec{y}$,

$$\xi(\vec{x}, \vec{y}) = \langle f(\vec{x})\ f(\vec{y}) \rangle \tag{3.2}$$

where the angular brackets indicate the average over all possible field configurations. In the continuous field case, taking this average is difficult, because the averaging is calculated using a functional integral performed over all possible field configurations and weighted by the probability density functional for field configurations,

$$\langle f(\vec{x})\ f(\vec{y}) \rangle = \int \mathcal{D}f\ \mathcal{P}(f)\ f(\vec{x}) f(\vec{y}). \tag{3.3}$$

This average is difficult to compute directly even if the probability density functional of all possible field configurations is known. Typically, this average is estimated from data assuming that regions far separated are essentially independent realizations of the same process. This works because the correlation for cosmologically relevant fields vanishes with radius.

If the field is statistically homogeneous everywhere, then the correlation function only depends on the separation between the two points,

$$\xi(|r|) = \langle f(\vec{x}) f(\vec{x} + \vec{r}) \rangle \tag{3.4}$$

The correlation function describes the clumpiness of fields or, if the fields are taken as the probability density for the position of objects, the degree of clustering of the objects. An uncorrelated field with have $\xi(r) = 0$. This is called a Poisson process. Often, the

correlation function can be described as a power law, $\xi(r) \propto r^n$.

The correlation functions are often described in the Fourier domain because the Fourier transform of the correlation function is diagonal. The Fourier transform is defined as

$$f(\vec{k}) = \int d^3x \; e^{-i\vec{k}\cdot\vec{x}} \; f(\vec{x}) \tag{3.5}$$

and

$$f(\vec{x}) = \int \frac{d^3k}{2\pi} \; e^{i\vec{k}\cdot\vec{x}} \; f(\vec{k}). \tag{3.6}$$

The vector $\vec{k}$ is the three-dimensional wavevector indicating the wavenumber in the direction of each spatial dimension.

The power spectrum is the correlation function of f in Fourier space:

$$\begin{aligned} \langle f(\vec{k}) f(\vec{k}') \rangle &= \int d^3x \; d^3x' e^{-i(\vec{k}\cdot\vec{x} - \vec{k}'\cdot\vec{x}')} \langle f(\vec{x}) \; f(\vec{x}') \rangle \\ &= \int d^3x \; d^3x' e^{-i\vec{k}\cdot\vec{r}} e^{-i(\vec{k}-\vec{k}')\cdot\vec{x}'} \xi(r) \\ &= (2\pi)^3 \delta_D(\vec{k} - \vec{k}') \int d^3r e^{-i\vec{k}\cdot\vec{r}} \xi(r) \\ &= (2\pi)^3 \delta_D(\vec{k} - \vec{k}') \; P(k) \end{aligned} \tag{3.7}$$

The expected value features a Dirac delta function in the wavevectors $\vec{k}$ and $\vec{k}'$, so the individual wave numbers are uncorrelated. This is useful in statistical inference and in solving the dynamical equations of the universe. $P(k)$ is called the power spectrum. Measuring the power spectra of various fields is a primary goal in astrophysics.

The power spectrum can also be written as an integral over the spatial correlation function,

$$\begin{aligned} P(k) &= \int d^3r e^{-\vec{k}\cdot\vec{r}} \xi(r) \\ &= \int dr \; r^2 \frac{\sin(kr)}{kr} \; \xi(r) \end{aligned} \tag{3.8}$$

In the case of a field measured on a finite lattice, the field value at each lattice point

can be written as $\vec{f} = [f_0, f_1, ..., f_N]$. The joint probability of the elements of $\vec{f}$ is called Gaussian if

$$P(\vec{f}) = \frac{1}{\sqrt{(2\pi)^N |C|}} \exp\left(-\frac{1}{2} f_i C_{ij}^{-1} f_j\right) \tag{3.9}$$

where $C_{ij} = \langle f_i f_j \rangle$ is the covariance matrix which I have been calling the correlation function in the continuous case. Recall that the correlation function is diagonalized in Fourier space, so the probability for the Fourier transform of $\vec{f}$ is also a Gaussian distribution with a diagonal covariance matrix given by $P(k)$.

Angular Two-Point Correlation

The Euclidean two-point correlation function is useful when three-dimensional information is available for the field. This is the case for a galaxy catalog with positions and redshifts available for each galaxy. Often, the field of interest is only known through its projection onto a sphere. In this case, a similar clustering measure can be used. It is called the angular correlation function.

The angular two-point correlation for fields defined on a sphere can be defined similarly to the Euclidean case. Define a mapping between points on a sphere to real numbers,

$$f : \mathbb{S}^2 \to \mathbb{R} \tag{3.10}$$

where $\mathbb{S}^2$ is the set of points on a sphere. The correlation function in this case is defined as

$$w(\hat{n}, \hat{n}') = \langle f(\hat{n}) f(\hat{n}') \rangle \tag{3.11}$$

where $\cos(\alpha) = \hat{n} \cdot \hat{n}'$. If the statistical process underlying the generation of the field is rotationally invariant, then the angular correlation function depends only on the angle between the vectors,

$$w(\alpha) = \langle f(\hat{n}) f(\hat{n}') \rangle \tag{3.12}$$

where $\cos(\alpha) = \hat{n} \cdot \hat{n}'$.

Similarly to the Euclidean case, the angular correlation can be expressed in another basis. The spherical harmonics are a set of basis functions that can be used to represent functions on a sphere. In terms of colatitude θ and azimuth ϕ angles, they can be written,

$$Y_{\ell m} = \sqrt{\frac{2\ell+1}{4\pi}\frac{(\ell-m)!}{(\ell+m)!}}\, P_\ell^m(\cos(\theta))\, e^{im\phi} \tag{3.13}$$

The spherical harmonics form a complete basis, so they can be used to represent any well-behaved function on a sphere,

$$f(\hat{n}) = \sum_{\ell=0}^{\infty} \sum_{m=-\ell}^{\ell} f_{\ell m} Y_{\ell m}(\hat{n}). \tag{3.14}$$

The coefficients of this representation are defined by

$$f_{\ell m} = \int d\Omega\; f(\hat{n}) Y^*_{\ell m}(\hat{n}). \tag{3.15}$$

The angular correlation function can be calculated in the spherical harmonic basis. In the case of rotational invariance,

$$\begin{aligned} \langle f^*_{\ell m}\, f_{\ell' m'} \rangle &= \int d\Omega\, d\Omega'\, Y^*_{\ell m}(\hat{n})\, Y_{\ell' m'}(\hat{n}') \langle f^*(\hat{n}) f(\hat{n}') \rangle \\ &= \int d\Omega\, d\Omega'\, Y^*_{\ell m}(\hat{n})\, Y_{\ell' m'}(\hat{n}')\, w(\alpha) \\ &= C_\ell\, \delta_{\ell \ell'}\, \delta_{m m'} \end{aligned} \tag{3.16}$$

C_ℓ is called the angular power spectrum of the field. The angular power spectrum only depends on the angular scale ℓ and each C_ℓ is uncorrelated with every other C'_ℓ.

Angular Two-Point Cross Correlation

The clustering of two fields can also be evaluated using a similar measure. The cross-correlation describes the excess clustering of two fields. Define two fields which both map the sphere to real numbers,

$$\begin{aligned} f &: \mathbb{S}^2 \to \mathbb{R} \\ g &: \mathbb{S}^2 \to \mathbb{R}. \end{aligned} \tag{3.17}$$

The cross-correlation function of these two fields is defined as

$$w^{fg}(\hat{n}, \hat{n}') = \langle f(\hat{n})\, g(\hat{n}') \rangle. \tag{3.18}$$

Under the same rotational invariance assumption used for the angular correlation function, the angular cross-correlation function only depends on the angle between $\hat{n}$ and $\hat{n}'$,

$$w^{fg}(\alpha) = \langle f(\hat{n})\, g(\hat{n}') \rangle. \tag{3.19}$$

Using the same technique as Equation 3.16,

$$\langle f_{\ell m} g^*_{\ell m} \rangle = C_\ell^{fg} \delta_{\ell \ell'} \delta_{m m'}. \tag{3.20}$$

The ensemble average of the correlation function depends only on the multipole ℓ.

3.3 Large-Scale Structure

The cosmological history of the universe evolved from fluctuations in the matter and radiation fields in the early universe to the structure that is observed today. The observed large-scale structure can be seen in galaxy catalogs such as the one shown in Figure 3.3. Calculating the large-scale structure at the large scales that I am interested in requires

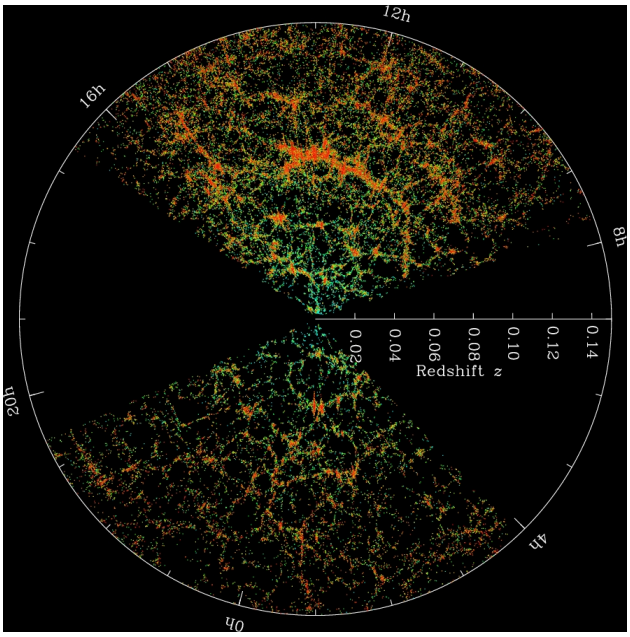

Figure 3.1: **Sloan Digital Sky Survey Large Scale Structure.** Galaxies observed by the Sloan Digital Sky Survey (SDSS) are tracers of the large-scale mass distribution in the universe. Each dot is a galaxy and the color represents the local galaxy density.

solving the Boltzmann equation with linear perturbation theory. While this is well beyond the scope of this thesis, the currently observed large-scale structure is described in this section.

The density of dark matter and its collapse into dark matter halos controls the formation of galaxies. The density of dark matter $\phi(\vec{x})$ can be written in terms of its overdensity,

$$\rho(\vec{x}) = \bar{\rho}(1 + \delta(\vec{x})). \tag{3.21}$$

The overdensity $\delta(\vec{x})$ can be rewritten in in the Fourier domain,

$$\tilde{\delta}(\vec{k}) = \int d^3x \, e^{\vec{k}\cdot\vec{x}} \, \delta(\vec{x}). \tag{3.22}$$

The power spectrum can be obtained from the field by

$$\langle \tilde{\delta}(\vec{k})\tilde{\delta}(\vec{k'})\rangle = (2\pi)\delta_{\text{Dirac}}(\vec{k} - \vec{k'})P_k \tag{3.23}$$

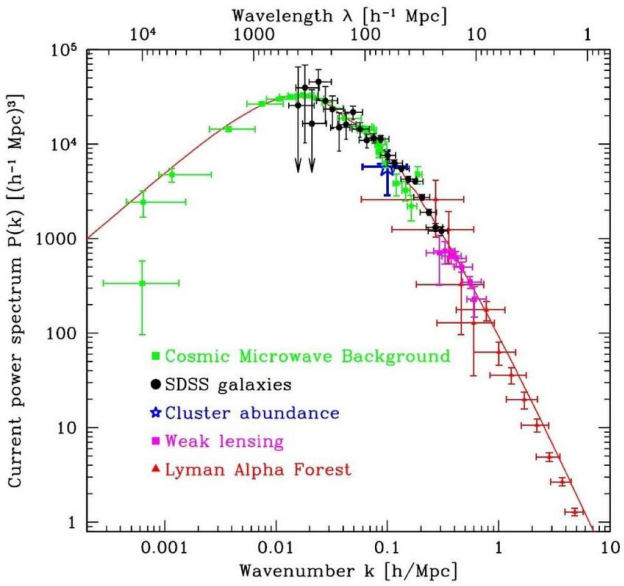

Figure 3.2: **Matter Power Spectrum.** The matter power spectrum measured by various probes. The figure is taken from Tegmark et al. (2004).

where P_k is the Fourier transform of $\xi(r)$. The matter power spectrum P_k is one of the principle observables used in cosmology to constrain cosmological models.

A current fit of the galaxy power spectrum is shown in Figure 3.3. At large scales (small k), the angular power spectrum grows until a peak at 0.02 h^{-1} Mpc. At larger scales than this, the growth of overdensities must compete with the expansion of the universe. Above the peak wavenumber, the growth of overdensities is inhibited by gas pressure preventing collapse at the smallest scales.

The angular correlation function can be obtained by integrating the power spectrum along the line of sight. The theoretical angular correlation can be calculated from this distribution and the known three-dimensional power spectrum (Dodelson & Schmidt, 2021). The distribution of a catalog with respect to comoving distance (or equivalently redshift) can be written as

$$W(\chi) = \frac{1}{N}\frac{dN}{d\chi}. \tag{3.24}$$

The projected overdensity of galaxies on the sphere can be written as

$$\Delta_g(\vec{n}) = \int_0^\infty d\chi W(\chi)\delta_g(\vec{x} = \vec{n}\chi, \eta = \eta_0 - \chi) \tag{3.25}$$

where δ_g is the three-dimensional overdensity, $\vec{n}$ is the observing direction unit vector, $\vec{x}$ is the three-dimensional position vector, and η is the time.

The ensemble average angular correlation can be written as,

$$\langle \Delta_{g,\ell m} \Delta^*_{g,\ell' m'} \rangle = \delta_{\ell\ell'}\delta_{mm'}C_\ell^{gg} \tag{3.26}$$

where

$$C_\ell^{gg} = \frac{2}{\pi}\int k^2\, dk \int_0^\infty d\chi W(\chi) j_\ell(k\chi) \int_0^\infty d\chi' W(\chi') j_\ell(k\chi') P(\vec{k}, \eta(\chi), \eta(\chi')), \tag{3.27}$$

P is the three-dimensional matter power spectrum, and j_ℓ is the Bessel function. See section 11.2 of Dodelson & Schmidt (2021) for a full derivation. This integral can be simplified using an approximation known as the Limber approximation. On small scales ($\ell \gg 1$, the galaxy pairs contributing to the cross-power spectrum span a small angle in the sky. The Bessel functions damp the integral at larger angular separations. In this case, Equation 3.27 can be simplified to

$$C_\ell^{gg} = \int \frac{d\chi}{\chi^2} W^2(\chi) P\left(k = \frac{\ell + \frac{1}{2}}{\chi}, \eta(\chi)\right) \tag{3.28}$$

A similar relationship exists for the angular cross-power spectrum. The distribution of galaxies and neutrinos with respect to comoving distance are written $W_g(\chi)$ and $W_\nu(\chi)$. The ensemble average angular cross-correlation can be written as,

$$\langle \Delta_{g,\ell m} \Delta^*_{\nu,\ell' m'} \rangle = \delta_{\ell\ell'}\delta_{mm'}C_\ell^{g\nu} \tag{3.29}$$

where

$$C_\ell^{g\nu} = \frac{2}{\pi}\int k^2\, dk \int_0^\infty d\chi W_g(\chi) j_\ell(k\chi) \int_0^\infty d\chi' W_\nu(\chi') j_\ell(k\chi') P(\vec{k}, \eta(\chi), \eta(\chi')). \tag{3.30}$$

The Limber approximation can also be used on this integral,

$$C_\ell^{g\nu} = \int \frac{d\chi}{\chi^2} W_g(\chi) W_\nu(\chi) P\left(k = \frac{\ell + \frac{1}{2}}{\chi}, \eta(\chi)\right). \tag{3.31}$$

Both equations 3.28 and 3.31 can be calculated for a given matter power spectrum. In practice, the Limber approximation is used above the multipole threshold, and the full expressions, equations 3.27 and 3.30 are calculated numerically for small multipoles.

Experimental Effects

Beam Function and Noise

Real experiments have a finite angular resolution and noise. Point-like objects appear blurred to finite size due to detector imperfections. This effect is described using a point spread function (PSF) in the spatial domain. The PSF, denoted by $B(\hat{n}, \hat{n}')$, describes how signal from $\hat{n}$ leaks into $\hat{n}$ and $\eta(\hat{n})$ is the noise. The observed signal is a convolution of the true signal with the PSF,

$$f^{\text{obs}}(\hat{n}) = \int d\Omega' f(\hat{n'}) B(\hat{n}, \hat{n}') + \eta(\hat{n}). \tag{3.32}$$

The observed spherical harmonics are

$$f_{\ell m}^{\text{obs}} = \int d\Omega\, Y_{\ell m}^*(\hat{n})\; f^{\text{obs}}(\hat{n}). \tag{3.33}$$

Combining Equations 3.32 and 3.33 and evaluating the integrals results in an expression for the effect of the beam function on the observed field in spherical harmonics,

$$f_{\ell m}^{\text{obs}} = \sum_{\ell'=0}^{\infty} \sum_{m'=-\ell}^{\ell} B_{\ell m \ell' m'} f_{\ell' m'} + \eta_{\ell m}. \tag{3.34}$$

If the beam is constant in the sky and the same in every direction,

$$f_{\ell m}^{\text{obs}} = B_\ell \; f_{\ell m} + \eta_{\ell m}. \tag{3.35}$$

If the noise is Gaussian or Poissonian,

$$\langle \eta_{\ell m} \; \eta_{\ell m}^* \rangle = N_\ell \delta_{\ell \ell'} \delta_{m m'}. \tag{3.36}$$

N_ℓ is called the noise power spectrum. If the noise follows a Poisson distribution as in a galaxy catalog,

$$\langle \eta_{\ell m} \; \eta_{\ell m}^* \rangle = \frac{4\pi f_{\text{sky}}}{n} \tag{3.37}$$

where n is the number of observed and f_{sky} is the fraction of the sky observed. This is independent of multipole. The unbiased estimator of the angular power spectrum is

$$C_\ell = \frac{1}{B_\ell^2} \left(\frac{1}{2\ell + 1)} \sum_{m=-\ell}^{\ell} |f_{\ell m}^{\text{obs}}|^2 - N_\ell \right). \tag{3.38}$$

The variance of this estimator is

$$\text{Cov}\left[C_\ell, C_{\ell'}\right] = \frac{2}{2\ell + a} \left(C_\ell + \frac{N_\ell}{B_\ell^2} \right)^2 \delta_{\ell \ell'}. \tag{3.39}$$

The angular cross-power spectrum is treated similarly. The field g is defined the same as f

$$g^{\text{obs}}(\hat{n}) = \int d\Omega' g(\hat{n'}) B^g(\hat{n}, \hat{n}') + \eta^g(\hat{n}). \tag{3.40}$$

If the fields are uncorrelated, then

$$\langle \eta^f_{\ell m} {\eta^g_{\ell m}}^* \rangle = 0. \tag{3.41}$$

The unbiased estimator of the angular cross-power spectrum is

$$C_\ell^{fg} = \frac{1}{B_\ell^f B_\ell^g} \frac{1}{2\ell+1} \sum_{m=-\ell}^{\ell} |f^{\text{obs}}_{\ell m} g^{\text{obs}*}_{\ell m}|^2. \tag{3.42}$$

The variance of this estimator is

$$\text{Cov}\left[C_\ell^{fg}, C_{\ell'}^{fg}\right] = \frac{1}{2\ell+1}\left({C_\ell^{fg}}^2 + C_\ell^{ff}\ C_\ell^{gg}\right)\delta_{\ell\ell'}. \tag{3.43}$$

Masking and Mode Coupling

The covariance for the angular power spectrum and angular cross power spectrum are both diagonal when the full sky is observed. With a full sky observation, each power spectrum mode can be inferred without reference to the others because they are statistically independent. This is not true when a spatial mask is used. Frequently a spatial mask is needed to remove the effect of some undesirable foreground. The estimators themselves also become biased. As a first correction, the estimators can be multiplied by the fraction of the sky unmasked,

$$C_\ell^{\text{biased}} \approx f_{\text{sky}} C_\ell^{\text{biased}}. \tag{3.44}$$

A simple mask denoted $W(\hat{n})$ is an indicator function for each point in the sky (or pixel). If the mask has a value of one, that region should be included. The spherical harmonic transform of this mask is

$$w_{\ell m} = \int d\Omega\, W(\hat{n})\, Y^*_{\ell m}(\hat{n}) \tag{3.45}$$

with power spectrum

$$W_\ell = \frac{1}{2\ell+1} \sum_{m=-\ell}^{\ell} |w_{\ell m}|^2. \tag{3.46}$$

The masked field can be decomposed into spherical harmonics,

$$\begin{aligned} f_{\ell m} &= \int d\Omega\, f(\hat{n})\, W(\hat{n})\, Y^*_{\ell m} \\ &= \sum_{\ell=0}^{\infty} \sum_{m=-\ell}^{\ell} \int d\Omega\, Y_{\ell' m'}(\hat{n})\, W(\hat{n})\, Y^*_{\ell m}(\hat{n}) \\ &= \sum_{\ell=0}^{\infty} \sum_{m=-\ell}^{\ell} f_{\ell' m'}\, K_{\ell m \ell' m'}. \end{aligned} \tag{3.47}$$

$K_{\ell m \ell' m'}$ is called the coupling kernel Although this integral can be evaluated analytically, the coupling kernel may also be estimated through forward modeling. The forward modeling approach is taken in this thesis. The computation of the Cov $[C_\ell, C_{\ell'}]$ is done numerically by simulating realistic data sets although, in principle, it could be evaluated through the coupling kernel.

3.4 Summary

The universe is not homogenous; there are weak anisotropies across a wide range of scales. The large-scale mass distribution of the universe is relevant to this thesis. Primordial density fluctuations evolve according to the Boltzmann equation. Small perturbations grow in size eventually forming dark matter halos where galaxies can form. Neutrino sources likely live within these dark matter halos. The large-scale structure can be traced by galaxies. Except on the smallest scales, the density of galaxies is a linear tracer of the underlying mass density. The three-dimensional matter power spectrum is related to the angular power spectrum through the projection on to the celestial sphere.

Measuring angular correlation functions is straightforward but requires some care to account for experimental effects. The finite angular resolution is described by a beam function which is effectively a smearing on the celestial sphere. It is often useful to remove regions of the sky that are contaminated by background noise sources; however, this causes correlations between the different multipoles which must be accounted for by using a

covariance matrix in any likelihood formulation.

4 ICECUBE NEUTRINO OBSERVATORY

4.1 Introduction

The virtue of neutrinos as an astrophysical messenger is also their vice for observational efforts: Neutrinos rarely interact with matter. The mean free path (or interaction length) of a neutrino in ice is defined as

$$\lambda = \frac{1}{\sigma N} \tag{4.1}$$

where $N = \frac{\rho N_A}{M}$ is the number density, ρ is the mass density, N_A is Avogadro's number, and $M \approx 18$ g mol^{-1} is the molar mass of ice. The interaction cross section for neutrino interaction is approximately 10^{-33} cm^2 at 1 PeV. In ice, the interaction length of a neutrino is 3.2×10^8 meters or 51 Earth radii. To detect such rare events, a detector with a large interaction volume is needed. Fortunately, the observed neutrino flux is large, of the order of 10^6 cm^{-2} s^{-1}.

When neutrinos interact, they will produce charged particles which will emit Cherenkov radiation. This radiation can propagate through ice and be detected by light detectors like photomultiplier tubes embedded in the ice. If many photomultiplier tubes detect light, the spatial arrangement of the detectors and the timing of light detection can be used to reconstruct the event morphology. If the event morphology and energy is reconstructed well, it may provide information about the origin of the neutrino.

4.2 Neutrino Interactions

Neutrinos rarely interact with other matter. When they do, neutrinos interact through the weak force. They are electrically neutral, so they do not interact electromagnetically, nor do they interact through the strong force. The basic vertices of weak interactions involving neutrinos exploit the exchange of a charged $W^{\pm}$ boson or neutral Z boson. These are shown in Figure 4.2. The $W^{\pm}$ and Z bosons couple to all fermions, so neutrinos can interact with

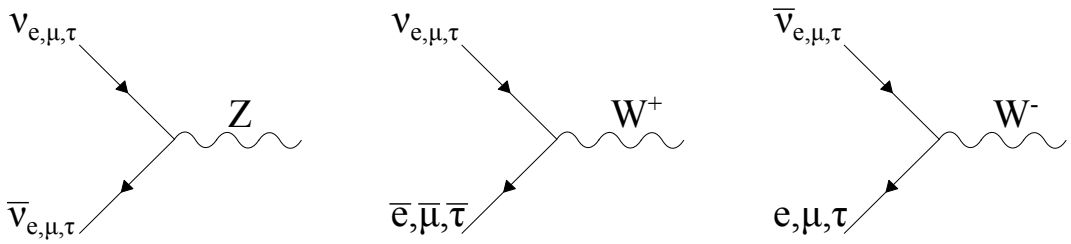

Figure 4.1: **Weak Interaction Vertices for Neutrinos.** These Feynman diagrams form the basic vertices for neutrino interactions. These vertices hold for other fermions as well.

baryons through these exchanges.

IceCube is sensitive to interactions between neutrinos and nucleons in the ice. At high energy, this is called neutrino-nucleon deep inelastic scattering (DIS). In DIS, neutrinos interact with one of the quarks within a single nucleon. After the interaction occurs, the nucleon is destroyed, and the free quarks form a variety of unstable hadrons. These hadrons decay and produce a shower of charged hadrons which may be detected later. DIS can occur through two channels by exchange of a Z boson or a $W^{\pm}$ boson.

If the interaction is mediated by a Z boson, it is called a neutral current interaction. Neutral current interactions are named as such because there is no exchange of electric charge. This process is illustrated in Figure 4.2. In this process, a neutrino exchanges a Z boson with a quark within a nucleon. This process is summarized by

$$\begin{aligned} p + \nu_\ell &\rightarrow \nu_\ell + X \\ p + \bar{\nu}_\ell &\rightarrow \bar{\nu}_\ell + X \\ n + \nu_\ell &\rightarrow \nu_\ell + X \\ n + \bar{\nu}_\ell &\rightarrow \bar{\nu}_\ell + X \end{aligned} \tag{4.2}$$

where ℓ is the appropriate lepton flavor and X can be a variety of hadrons. The quark and neutrino retain their identity, but the quark is freed from the nucleon. The nucleon

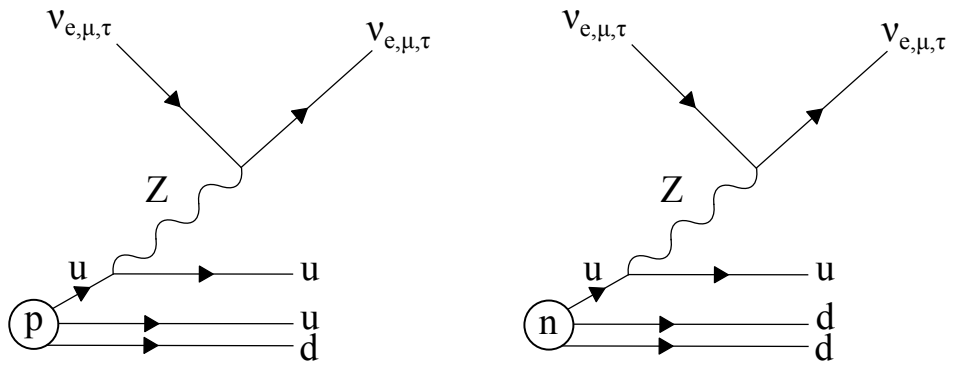

Figure 4.2: **Neutral Current Interaction.** DIS neutral current interactions occur when a neutrino and quark within a proton or neutron exchange a Z boson. Neutrinos are shown in the Feynman diagram above, but antineutrinos undergo this process equally. The scattering may occur with the up or down quark.

disintegrates and produces a shower of secondary particles.

Charged current interactions involve the exchange of a $W^{\pm}$ boson; there is a net electromagnetic charge exchange. Because the neutrino is neutral and the charge is exchanged, the outgoing particle must have a different identity. Lepton number and electric charge must be conserved, so a neutrino will always produce a lepton of the same flavor and charge parity. To conserve electric charge, a neutrino will exchange a W^{-} with a nucleon. An antineutrino will exchange a W^{+} because it needs to create antileptons. Similar interactions will occur for neutrons. These interactions are defined by

$$\begin{aligned} p + \nu_\ell &\rightarrow \ell + X \\ p + \bar{\nu}_\ell &\rightarrow \bar{\ell} + X \\ n + \nu_\ell &\rightarrow \ell + X \\ n + \bar{\nu}_\ell &\rightarrow \bar{\ell} + X. \end{aligned} \tag{4.3}$$

The newly produced leptons may travel some distance before interacting. Electrons and muons will lose most of their energy through ionization. Electrons will dissipate their energy quickly. Muons will be minimum ionizing particles. They will create a trail of ionization which is not likely to be directly detectible; however, they will also emit Cherenkov

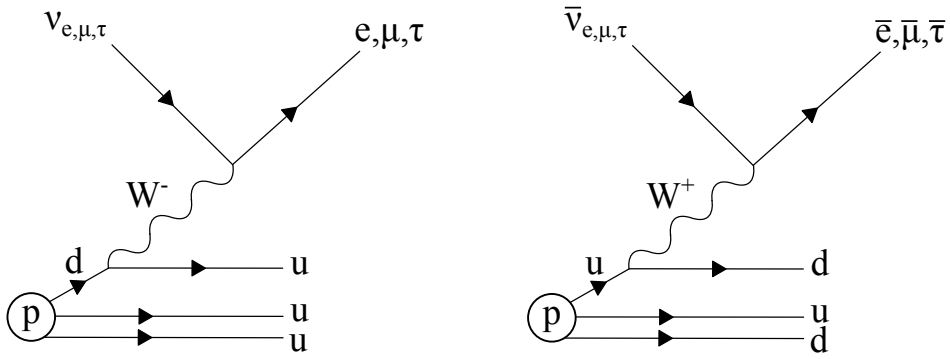

Figure 4.3: **Charged Current Interaction.** DIS charged current interactions occur when a neutrino and quark within a proton or neutron exchange a $W^{\pm}$ boson. Lepton number and electric charge must be conserved, so a neutrino will create a lepton of the same flavor and charge parity through the exchange of W^{+} and the opposite will happen for an antineutrino. The scattering may occur with the up or down quark.

radiation. Most muons exit the detector volume without dissipating all their energy. This Cherenkov radiation allows better reconstruction of neutrino arrival direction. Tau leptons may travel some distance before decaying and producing another hadronic shower.

4.3 The IceCube Detector

The IceCube Neutrino Observatory is designed to detect Cherenkov light from energetic secondary particles emitted by neutrino interactions with ice.

The Digital Optical Modules (DOMs) are the basic detector unit that detects Cherenkov light. A schematic of the DOM design is shown in Figure 4.6. Each DOM is contained in a 30cm diameter spherical glass pressure vessel. Inside the glass pressure vessel is a large photomultiplier tube. Photomultiplier tubes contain a ladder of cathodes with increasingly positive voltages arranged so that there is a clear trajectory from one cathode to the next in the ladder. When a photon enters the photomultiplier tube, it may collide with a metal cathode and free an electron through the photoelectric effect. The newly free electron will be pulled toward the next cathode and accelerated toward it by the cathode electric field. When the electron collides with the cathode, it can free multiple electrons which will all

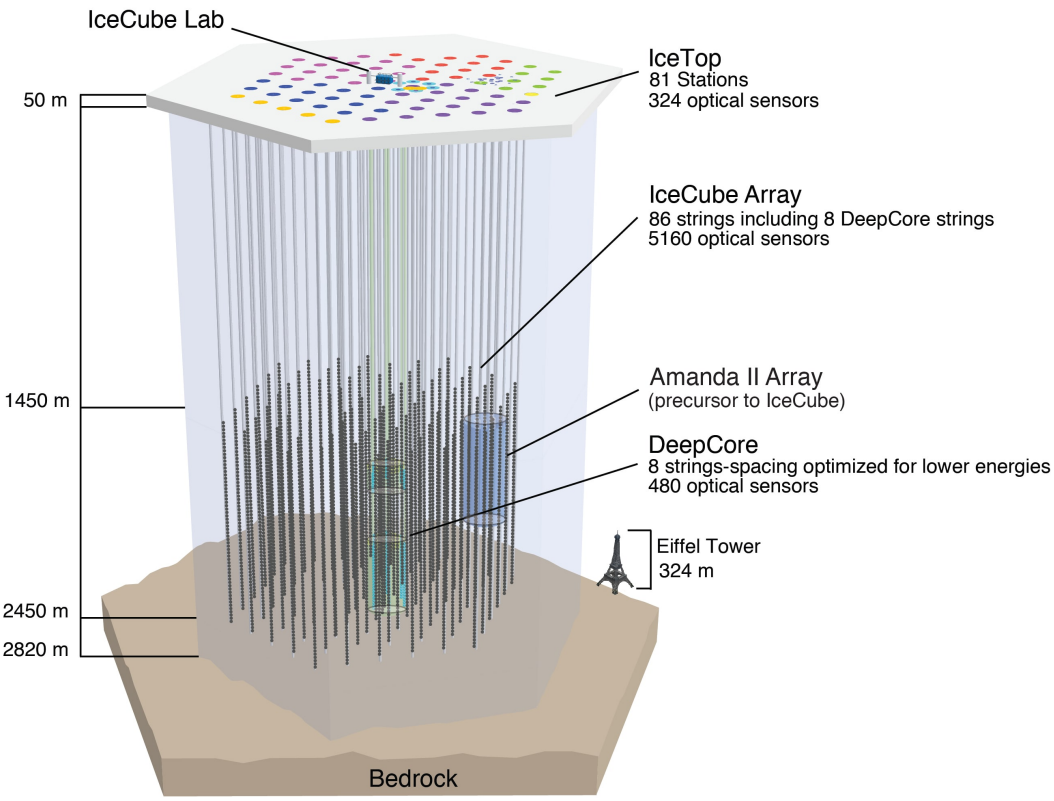

Figure 4.4: **IceCube Detector Schematic.** The IceCube detector consists of 86 strings carrying a total of 5160 optical sensors. The neutrino events can be reconstructed based on the intensity and timing of light observed in all the optical sensors.

proceed to the next cathode in the ladder. This exponential process produces a gain which is collected in a final readout cathode. The current through the readout cathode is passed through several amplifiers and postprocessing circuits within the DOM. If the current meets several trigger conditions, then the full waveform is communicated to the IceCube lab through data cables contained in the string.

The DOMs also contain LED flashers for calibration. Event reconstruction requires precise knowledge of the three-dimensional position of each DOM relative to all the other DOMS. The LED flashers on a single DOM can be triggered and the adjacent DOMS can be monitored for the time when the recieve the signal. The LED flashers can also be used to calibrate ice properties.

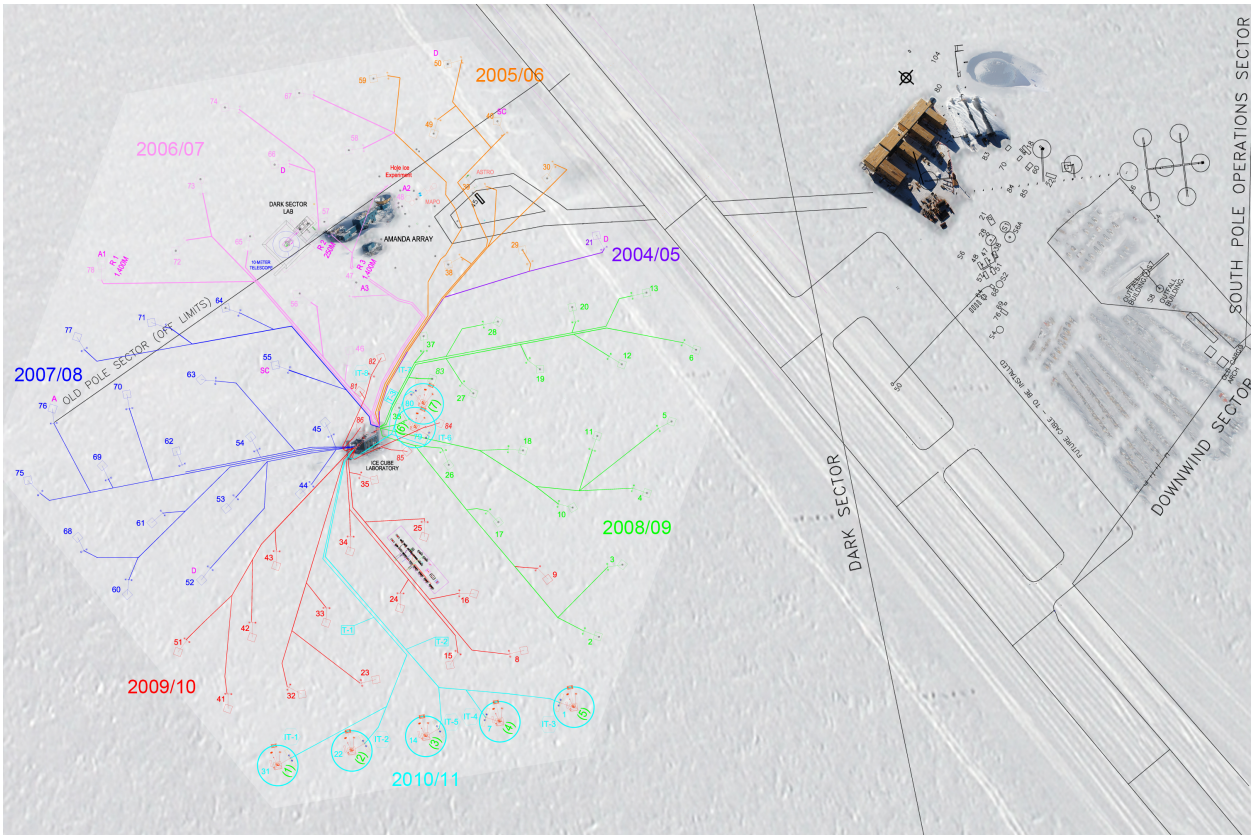

Figure 4.5: **IceCube String Layout.** This ariel photo shows the layout of the IceCube strings. The strings are separated by approximately 100 meters.

The DOMs communicate data through the strings to the IceCube lab. The IceCube lab is a permanent facility on the ice surface containing computing resources required to monitor and readout the DOMs. Data is stored here and relayed to the north by satellite and the full data is stored on disk for transport to the north by plane.

The glacial ice that is instrumented by the IceCube DOMs is both the interaction medium for neutrinos and affects the propagation of Cherenkov light. Although the ice at the South Pole is the clearest natural ice in the world, it contains impurities, air bubbles, and microscopic crystal structures that can attenuate and scatter visible light. The attenuation length in the ice is approximately 50 meters. There is also an ice layer approximately horizontal 2.1 km below the surface that is contaminated by dust from prehistoric volcanic activity. This dust layer attenuates light and must be modeled. Additionally, the boreholes

that the IceCube strings are deployed in are backfilled with water after completion. The water freezes quickly but contains many air bubbles which can scatter light. This "hole ice" is a major systematic uncertainty in IceCube analysis.

Although the full waveform data is preserved and eventually transported from the South Pole to data centers in the Northern hemisphere by plane, the interest in realtime analysis requires on-site filtering and transmission by satellite. Waveform noise is dominated by thermal noise and radioactive decays within the pressure vessel glass. The IceCube Data Acquisition System monitors the raw waveforms to identify potentially interesting neutrino events (Kelley & IceCube Collaboration, 2014). The foundational trigger is the Hard Local Coincidence (HLC) hit. The HLC trigger monitors for waveforms in adjacent DOMs to surpass a critical voltage within $1\mu s$ of each other. If there are eight HLC hits within 5μs, the simple multiplicity trigger (SMT8) trigger is activated which causes the waveforms to be read out from all DOMs. The SMT8 trigger occurs with a rate of 2100 kHz. This triggering process reduces the data volume from 1 TB to 100 GB per day.

4.4 Event Morphology

The physics of the underlying DIS interaction channel and the configuration of the detector determine the appearance of events observed by IceCube. There are two commonly observed event morphologies: cascades and tracks. Additional morphologies are possible, including double bangs and starting tracks. These rare events do not contribute significantly to the results presented in this thesis. The relationship between neutrino flavor and event morphology is sketched in Figure 4.4.

Cascade events occur in most interactions with all neutrino types. The cascades are essentially hadronic showers that are contained within the detector volume. Typically a cascade is ellipsoidal with major and minor axis radii approximately equal to a few string spacings. When a neutrino of any flavor undergoes a neutral current interaction, one of

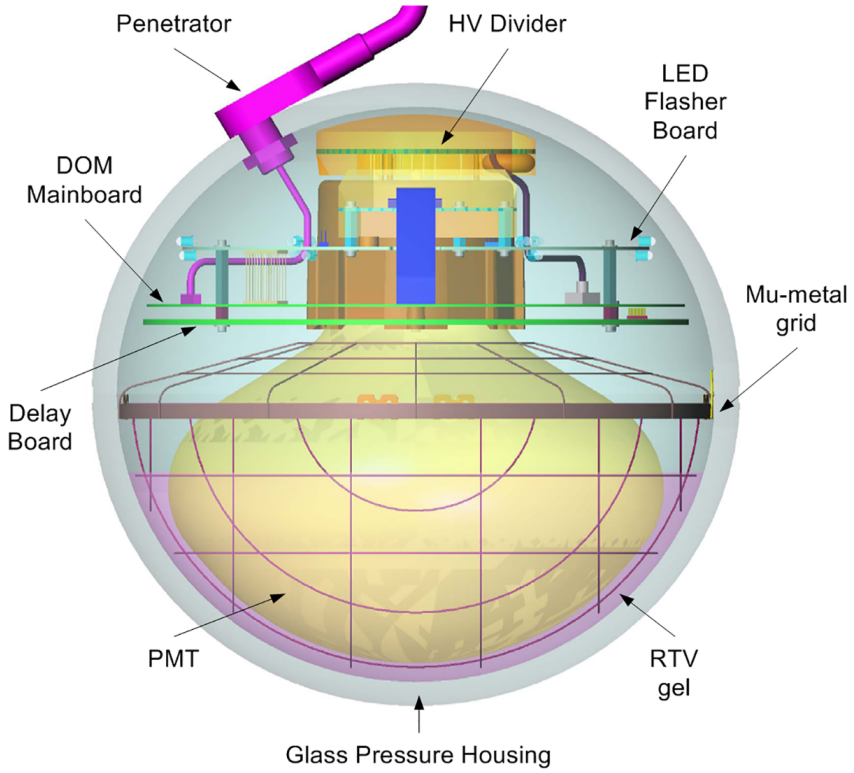

Figure 4.6: **Digital Optical Module Engineering Diagram.** The diagram shows the major components of the IceCube Digital Optical Module. At the simplest level, the DOM is a large light collector and electronics to power and read out the light collector contained in a spherical pressure vessel.

the output products is a neutrino of the same flavor. It is rare for that neutrino to interact within the detector volume again. A hadronic shower is produced by DIS products. If the neutrino is an electron neutrino, the outgoing electron will lose its energy within a string spacing length, so it cannot be distinguished from the hadronic shower. If the neutrino is a tau neutrino, the tau lepton can escape, or it can decay within the detector volume. If it escapes, the event will appear as a single cascade. The hadronic shower produced in that interaction produces hadrons which decay into lighter particles and emit Cherenkov radiation as the shower develops. When the entire shower is fully contained, the energy can be reconstructed well. The directional information is more difficult to infer. Hadronic showers tend to develop widely, so the event major and minor axis radii are similar. The major axis will point toward the momentum vector of the incident particle, but it can be

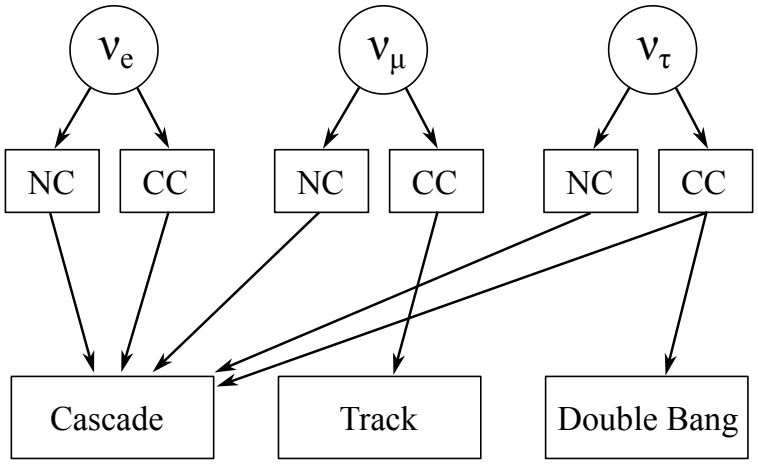

Figure 4.7: **Neutrino Flavor and Event Morphology.** The relationship between neutrino flavor and event morphology is shown below. Most neutrinos will produce cascades. The same relationships are true for antineutrinos. Only charged current interactions of muon neutrinos can produce track events. Similarly, only tau neutrinos can produce the double bang morphology.

difficult to reconstruct precisely. Angular localization uncertainties are typically a few to tens of degrees. If the tau lepton decays within the detector volume, it will produce a second hadronic shower. These events are rare but have been occasionally observed.

Track events are easier to localize. When a ν_μ undergoes a charged current interaction, a muon will be produced. Muons produced in this way lie in the minimum of the Bethe-Block equation. Their energy loss is dominated by ionization, but they lose only a little energy while traversing the detector volume. They emit Cherenkov light along their linear trajectory, and this linear pattern makes the spatial localization much more precise than cascades. Track events typically have angular uncertainty of 0.25 to 1 degree. Track events usually begin outside of the detector volume and pass through, so the energy of the original neutrino is not well known. Some track events do originate within the detector volume. These are called starting events, and they combine the directional precision of tracks with the energy precision of cascades.

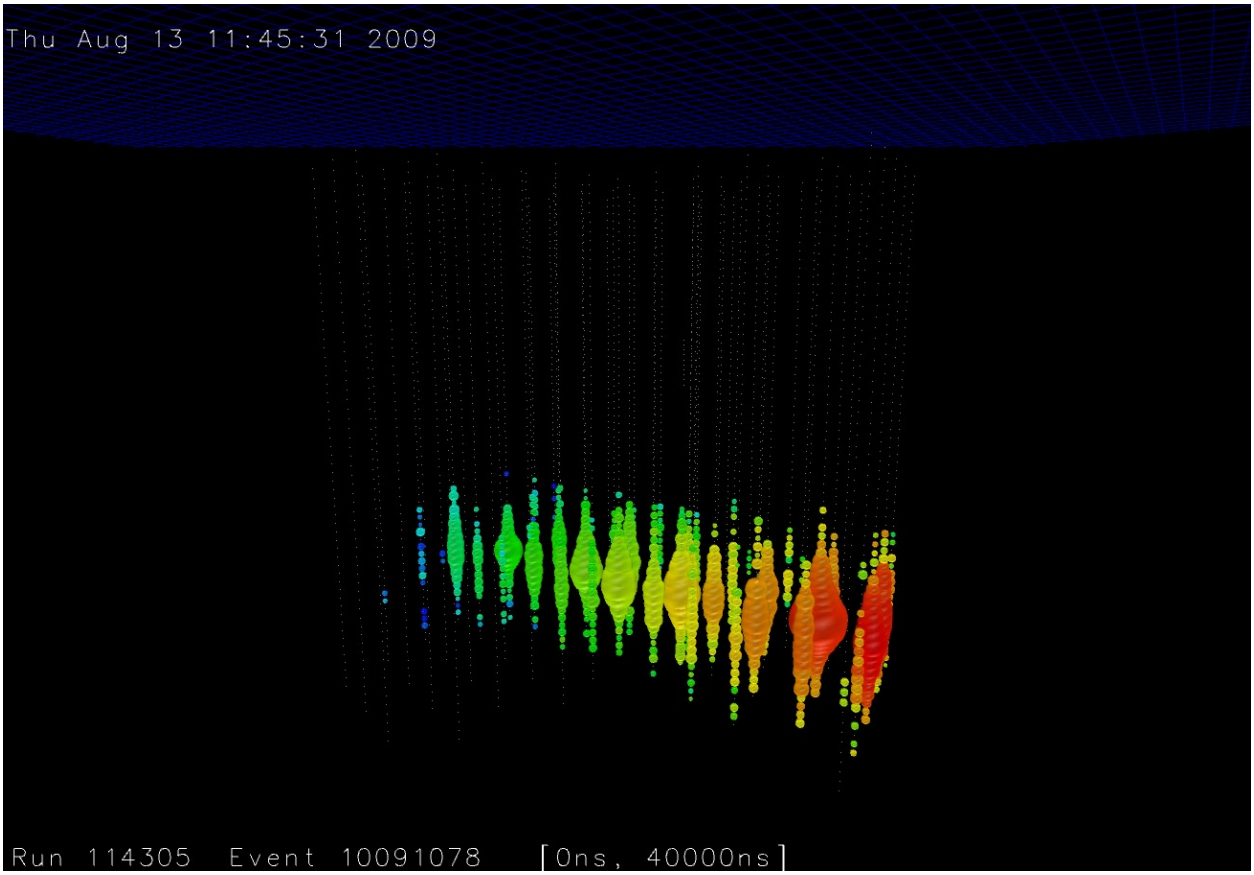

Figure 4.8: **IceCube Track Event.** The event display above shows an example of a track event in IceCube. Each sphere represents one DOM. The size of the DOMs indicates the intensity of Cherenkov light observed by that DOM and the color indicates the time of light arrival. This muon traversed the detector from left to right at a nearly horizontal angle.

4.5 Northern Tracks Data Set

The work presented in this dissertation uses a data set designed for neutrino astronomy. Internally, the data set is referred to as "Northern Tracks" because it is designed to select track-like events coming from the northern sky (IceCube Collaboration et al., 2022b). As suggested before, the track-like event directions can be reconstructed with ~ 0.25 degree precision. Track-like events are produced by muon neutrinos, but the origin of those muons cannot be inferred from the event alone. IceCube primarily observes muon neutrinos from three sources.

1. **Astrophysical Neutrinos:** The first muon neutrino production channel occurs when

neutrinos originally produced within astrophysical environments interact with the ice or the Earth and the resulting muon traverses through the detector. These are the signals that one is generally looking for when doing neutrino astronomy.

2. **Atmospheric Neutrinos:** When a cosmic ray collides with the atmosphere, it may produce a neutrino along with a shower of other particles. The atmospheric neutrino can traverse through the Earth and produce a muon just like an astrophysical neutrino. These muons are the dominant background in the Northern Tracks data set.

3. **Atmospheric Muons:** These muons are produced when cosmic rays collide with the atmosphere and can appear as track-like events to IceCube. The muons that come from the northern sky cannot traverse through the bulk of the Earth; they lose energy to ionization and are heavily attenuated before reaching IceCube. The attenuation of atmospheric muons is the primary driver for selecting neutrinos coming from the northern sky.

The Northern tracks data selects only events with reconstructed directions that appear to traverse the Earth. This eliminates virtually all of the atmospheric muons. The astrophysical events cannot be distinguished from atmospheric events except on a statistical level. The primary distinguishing factor is the event energy; higher energy events are more likely to be astrophysical. The Northern Tracks data set used in this study contains data collected between 2010 and 2020. The data set filters events that occur in a small detector volume. This removes cascade events. Events with a zenith angle greater than 80°are excluded. The atmospheric muons are removed with 99.8% efficiency.

The track direction is reconstructed using the MPE algorithm Ahrens et al. (2004). The MPE reconstruction is a maximum likelihood method that attempts to identify the most likely origin for the neutrino given the timing and intensity of light observed by the DOMs. The propagation of the Cherenkov light cone is calculated through a tabulated ice model to calculate the likelihood of the data observed by all the DOMs given a propagation vector.

This process is repeated for different propagation vectors until the maximization process converges.

The muon energy is reconstructed using the truncated energy described in Abbasi et al. (2013). The muon energy loss is expected to be approximately 1 GeV per meter; however, there are large stochastic deviations from this process. The Cherenkov light intensity is directly proportional to the energy loss rate. The muon energy is estimated by dividing the best-reconstructed track into sub-track segments and excluding energy loss events with very high $\frac{dE}{dx}$. The muon energy is a lower limit on the neutrino energy due to energy losses outside the detector volume. The energy resolution is $\frac{\delta \log(E)}{\log(E)} = 22\%$.

4.6 Summary

The IceCube Neutrino Observatory is an ice Cherenkov detector at the South Pole. The detector consists of 5160 digital optical modules that detect Cherenkov light from charged secondary particles as they traverse the ice. Neutrinos can produce track-like and cascade-like morphologies. The track-like morphologies are most useful for neutrino astronomy because they can be reconstructed with degree-scale angular precision. The Northern Tracks data set is a data selection designed for neutrino astronomy in the northern sky.

5 ICECUBE CROSS-CORRELATION: METHODS AND RESULTS

5.1 Introduction

The origin of the diffuse neutrino flux observed by IceCube is unknown. Some clues may be found by searching for the clustering of these neutrinos with other catalogs of astrophysical objects. In this section, the methods used for performing a two-point angular cross-correlation of IceCube track-like neutrino events and an infrared galaxy catalog are described. The statistical significance of the clustering is evaluated using a log-likelihood ratio test, and no statistically significant clustering is found.

5.2 unWISE-2MASS Galaxy Catalog

WISE and unWISE

The Wide Field Infrared Explorer (WISE) is an orbital far-infrared observatory. As the name suggests, WISE is a wide-field observatory and has performed a systematic survey of nearly the entire sky since launch in 2009. WISE observes in four distinct infrared filters called W1, W2, W3, and W4 with effective wavelengths 3.368, 4.618, 12.082 and 22.194 μm respectively. The spectral response of these filters is shown in Figure 5.1[1]. During the WISE primary mission, the telescope surveyed the sky in all four bands. After the primary mission ended and the coolant required for the longer wavelength bands was completely consumed, the WISE mission was reactivated and tasked with searching for near-Earth asteroids in a mission called NEOWISE (Mainzer et al., 2011). The telescope continued to survey the sky in the shorter wavelength bands, W1 and W2.

The WISE observations from the primary and reactivated mission were reprocessed to produce the unWISE catalog (Schlafly et al., 2019). The unWISE catalog is a source catalog derived from all publicly available W1 and W2 observations. The catalog contains

[1]Filter data for WISE and 2MASS obtained from http://svo2.cab.inta-csic.es/theory/fps/

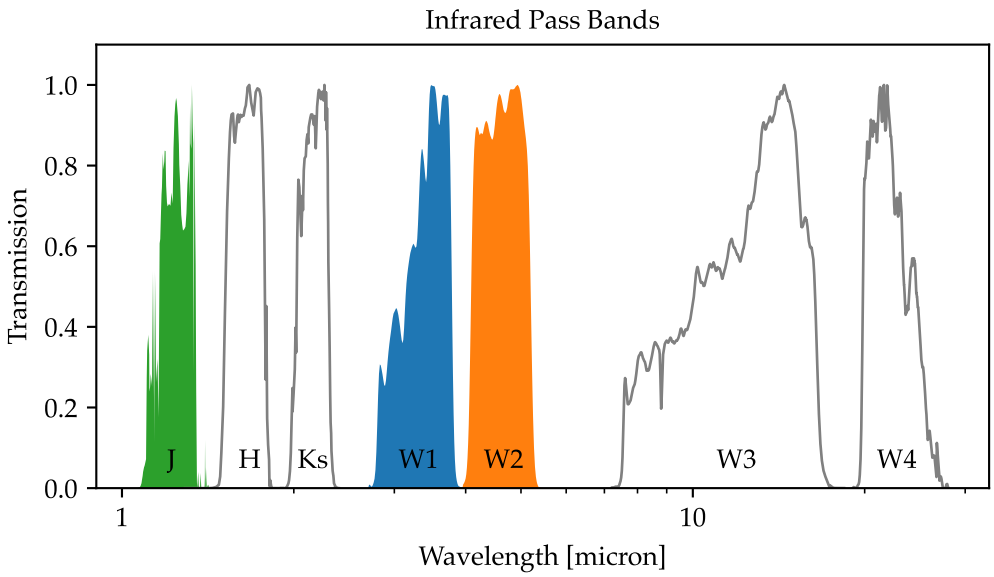

Figure 5.1: **WISE and 2MASS Passbands.** The colored and filled-in filters are used for the color and magnitude cuts used to construct the unWISE-2MASS catalog. The $W1$ and $W2$ filters are taken from the unWISE catalog and the J filter is taken from the 2MASS point source catalog.

photometry and astrometry (ie. brightness and positions) for roughly two billion sources galactic and extra-galactic sources spanning the entire sky in the W1 and W2 bands.

2MASS

The 2 Micron All Sky Survey was performed by a pair of ground-based near-infrared telescopes located at Mt. Hopkins Arizona and Cerro Tololo, Chile (Skrutskie et al., 2006). The two telescopes observed effectively the entire sky in three filters: H, J, K_s corresponding to wavelengths 1.25, 1.65, and 2.16 μm. The passbands observed by 2MASS are shown in Figure 5.1. 2MASS produced an all-sky catalog containing photometry and astrometry for 471 million sources.

unWISE-2MASS Catalog

Both the unWISE and 2MASS catalogs contain galactic and extra-galactic sources. To build a catalog that traces the cosmological large-scale matter distribution, the galactic sources must be removed. The galactic sources are primarily stars and white dwarfs which have a hotter temperature than the galaxies that we target, so their color will be bluer on average than the galaxies. Kovács & Szapudi (2015) identify a strategy based on simple color and magnitude cuts that effectively discriminate between galaxies and stars. The authors use the WISE source cross-matching provided with the original WISE point source catalog to obtain J magnitudes for the WISE sources. The authors attempted several different color and magnitude cuts as well as cuts obtained by a support vector machine classifier. The criteria that the authors suggest is to exclude sources with $W1 - J < -1.7$ to identify and eliminate galactic sources. They also apply magnitude cuts of $W1 \leq 15.2$ and $J < 16.5$ to improve the spatial uniformity of the catalog by excluding the faintest sources. Even with these cuts, the stellar contamination near the galactic plane remains high, so the authors apply a galactic plane mask derived from dust emission from Schlegel et al. (1998). The resulting galaxy catalog contains 2.4 million sources distributed across 21,200 square degrees or 51% of the sky. The authors estimate the completeness of the catalog by identifying a subset of sources with spectroscopically confirmed classifications as galaxies or stars. The authors find that the catalog contains 70% of the spectroscopically confirmed galaxies with only 1.2% contamination by stars.

Since the original WISE-2MASS catalog was first released, the unWISE catalog was published. The unWISE catalog makes several improvements over prior data releases:

- Including observations from the extended NEOWISE mission which increases the total exposure by a factor of five relative to the prior catalog release.
- Improved modeling of crowded sources which are now visible due to the increased exposure.

The original WISE-2MASS catalog used the previously released WISE catalog, so I reproduced this catalog using unWISE to obtain a catalog that more with higher completeness. The unWISE catalog does not include cross-matched 2MASS magnitudes, so I perform the cross-matching. For each source in the unWISE catalog, I identify the nearest 2MASS source and consider these sources associated in the final catalog if the sources are within 3″ of each other. I apply the color and magnitude cuts suggested by Kovács & Szapudi (2015) to arrive at the final catalog. The sources are included if all the following conditions are met:

- W1 - J $<$ -1.7
- W2 $<$ 15.5
- J $<$ 16.5

I apply a galactic plane mask derived from the Planck dust map (Aghanim et al., 2020) as well as masking sources with galactic latitudes less than 10 degrees. The Large and Small Magellanic Clouds are extended infrared sources which themselves contain stars that may be resolved by WISE and 2MASS. I mask a 0.5-degree radius circle surrounding both the LMC and SMC.

To interpret the significance of the cross-correlation, the galaxy catalog must be well understood. I estimate the redshift distribution of the galaxies by cross-matching the unWISE-2MASS catalog with another galaxy catalog featuring spectroscopically measured redshifts. The Galaxy and MASS Assembly (GAMA) survey contains spectroscopic redshifts for galaxies spanning approximately 250 square degrees (Driver et al., 2022). This corresponds to only 0.6% of the sky. For each source in the unWISE-2MASS catalog, I search for a GAMA source within 3″. If there is one, I assign the GAMA sources redshift to the unWISE-2MASS source.

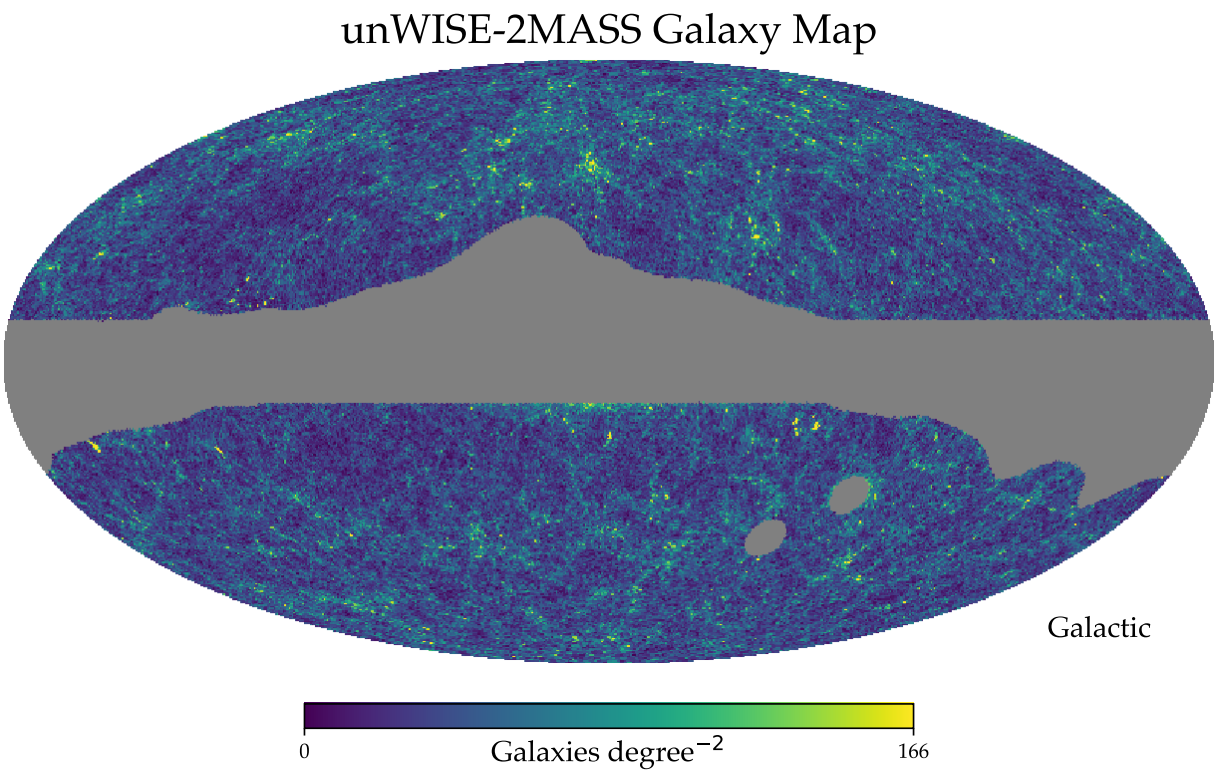

Figure 5.2: **unWISE-2MASS Galaxy Density.** The density of unWISE-2MASS galaxies on the sky. The galactic plane is masked as well as the Large and Small Magellanic Clouds.

unWISE-2MASS Angular Power Spectrum

The strength of the clustering of a tracer of large-scale structure is linearly related to the true matter-matter angular power spectrum on large scales,

$$C_\ell^{gg} = b_g^2 \, C_\ell^{mm}. \tag{5.1}$$

The bias parameter b_g arises from the formation of galaxies in overly dense regions in the underlying matter density field. Abell (1958) found that the clustering of galaxy clusters was stronger than expected due to this effect, and this effect is universal to any large-scale structure tracer whose formation depends on the underlying density. At scales much larger than the objects themselves, the clustering does not depend on scale, so it is a constant linear bias. At small scales, the bias depends on the scale because of the physical details of

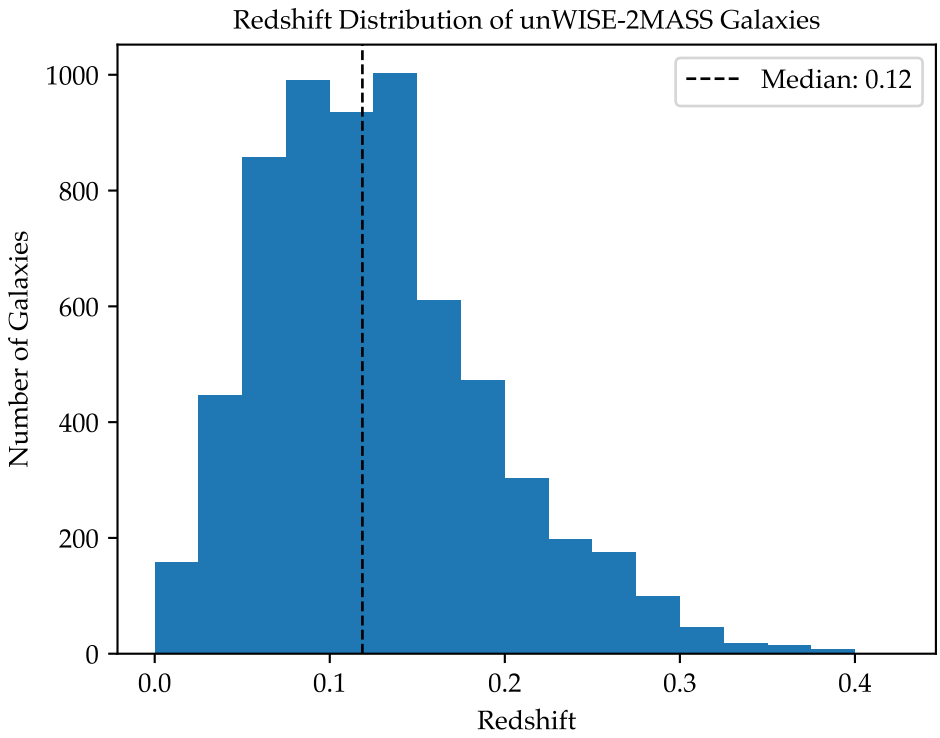

Figure 5.3: **unWISE-2MASS Redshift Distribution.** The redshift distribution of the unWISE-2MASS catalog found by cross-matching sources with the GAMA redshift catalog. The GAMA redshifts are spectroscopically measured, so they are precise enough to neglect their uncertainty.

galaxy and halo formation.

It is straightforward to estimate the bias parameter using the redshift distribution derived above and a model for the angular matter power spectrum. The true matter-matter angular power spectrum for the redshift distribution measured in Section 5.2 can be calculated using the Core Cosmology Library (CCL) (Chisari et al., 2019). The angular power spectrum of the unWISE-2MASS catalog was calculated using the Healpy routine `anafast`. The galaxy overdensity was calculated by binning the galaxies into a Healpix map then subtracting and dividing by the mean, ie.

$$\delta_g(\vec{x}) = \frac{n(\vec{x}) - \langle n \rangle}{\langle n \rangle}. \tag{5.2}$$

The angular power spectrum is shown in Figure 5.4. The uncertainty on the angular power spectrum was estimated using the analytic equation for the analytic uncertainty, Equation 3.39 (Zhang & Beacom, 2004). The Poisson noise was subtracted from the power spectrum by subtracting the analytic estimate for the Poisson noise in Equation 3.37.

The fit was performed using a likelihood maximization method, where the likelihood was assumed to be Gaussian and each multipole is independent,

$$\log \mathcal{L}(b_g) = \sum_{\ell=1}^{768} \left(\frac{C_\ell^{gg} - b_g^2 \, C_\ell^{mm}}{\sqrt{2}\sigma_\ell} \right)^2 + \text{constant.} \tag{5.3}$$

This likelihood was maximized with respect to b_g numerically. The best fit value of the bias parameter is $b_g = 1.23 \pm 0.01$. The uncertainty is estimated from the profile of the log-likelihood and represents the statistical uncertainty of the fit only. It does not include any systematic uncertainty. This could possibly include systematic uncertainty due to the measurement of the redshift distribution or numerical effects from the calculation of the model power spectrum. The value of b_g is consistent with the bias expected for a galaxy catalog. The χ^2 goodness of fit is 732.6 with 764 degrees of freedom indicating that the fit is a good description of the data.

5.3 Neutrino Mapmaking

Similarly to the galaxy autocorrelation, the cross-correlation is computed using pixelized sky maps. The sky is pixelized with the Healpix pixelization scheme with an "NSIDE" parameter equal to 128. This degree of pixelization corresponds to approximately a 0.5° pixel size. The IceCube point source function has a full-width half max greater than this, so there is no benefit to further pixelization which would increase computation time. A cross-correlation power spectrum scales linearly with the product of the beam functions of both catalogs, so it is not useful to pixelize one catalog more finely than the coarser of the two. Both WISE and 2MASS have PSF that is practically perfect compared to IceCube. The

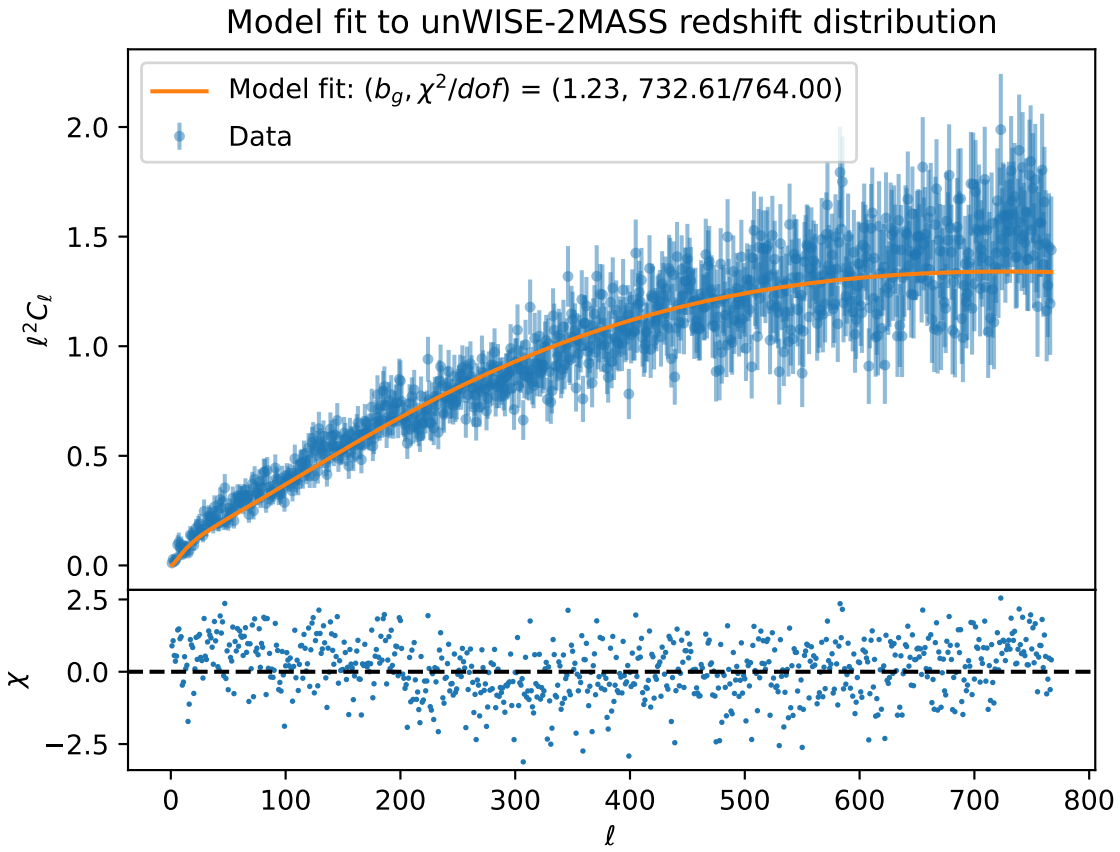

Figure 5.4: **unWISE-2MASS Angular Power Spectrum.** The two-point auto-correlation power spectrum is shown above with a model fit. The distribution of galaxies with respect to redshift is derived from the GAMA cross-matching. The best fit bias parameter is $b_g = 1.23$.

choice of coordinates does not matter; the cross-power spectrum is rotationally invariant. Because we must choose one, I create maps in equatorial coordinates.

The IceCube map is constructed similarly to the galaxy map but includes an additional weighting to correct the declination dependent exposure. First, a Healpix map containing counts is constructed by counting the number of neutrinos with reconstructed right ascension and declination in each pixel. The weight map $w(\vec{x})$ is designed to make a coarse estimate of the flux incident on the detector given the observed counts, eg $\phi(\vec{x}) \approx w(\vec{x})n(\vec{x})$ where $\vec{x}$ is the unit vector corresponding to a point on the celestial sphere and $\phi(\vec{x}) = \frac{dN}{dE}$ is the flux normalization assuming a power law spectrum. We do not know the power law

spectral index and the combined astrophysical and atmospheric flux will not be exactly a power law. Therefore, I average over the spectral index. The weight map is constructed using simulated IceCube events and their associated 'oneweight'. The 'oneweight' value is a weight assigned to each simulated IceCube event such that the event can be reweighted to produce whatever spectrum is desired with the weight indicating the rate of events at their true declination and energy. In other words, if one wished to create a sample of events following a power law spectrum with spectral index γ taking into account the IceCube effective area, one would draw samples from the pool of simulated events with weights equal to *oneweight* $\times$ *True Energy*$^{\gamma}$. The weight maps are defined similarly. We construct a histogram of simulated events weighted with a power law spectral index in declination bands in steps of equal $\sin(\delta)$ and divide the histogram value by the solid angle corresponding to that declination band, $2\pi\ \Delta\delta$. Practically, this stage is done using an IceCube internal software package called `csky`. From this, we compute a Healpix map by looking up the value of each pixel in the histogram. We smear this map with a 5° Gaussian kernel to remove the discrete bands. We compute such maps for an equally spaced grid of spectral indices and take the mean over the spectral index. Finally, the weight maps are computed as the multiplicative inverse of the acceptance maps. The acceptance maps $A(\vec{x})$ are shown in Figure 5.5. The counts maps are calculated as

$$\delta_{\nu}(\vec{x}) = \frac{n(\vec{x})/A(\vec{x}) - \langle n/A \rangle)}{\langle n/A \rangle} \tag{5.4}$$

5.4 Simulated Data Set Generation

The IceCube Collaboration maintains a data blindness policy. This policy requires that any analysis or statistical method is approved by the collaboration before the analyzer is allowed to run their analysis on the data. To demonstrate the performance of a statistical method, the IceCube Collaboration has developed tools for simulating realistic data sets.

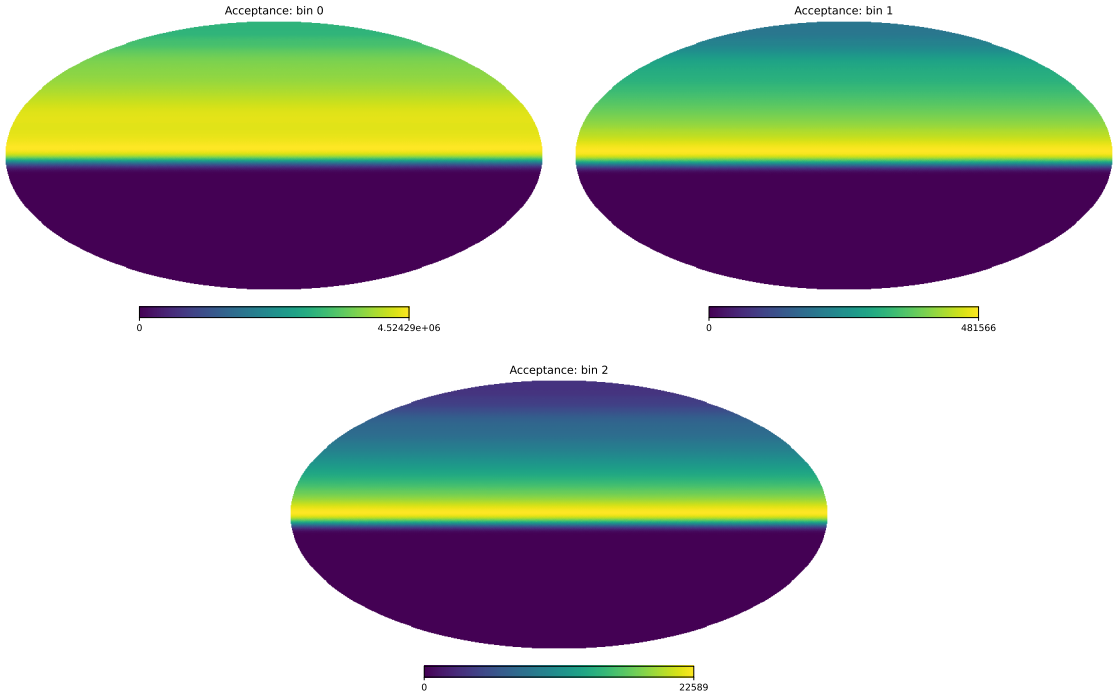

Figure 5.5: **Inverse IceCube Weight Maps.** The weight maps that are applied to the IceCube neutrino counts map are inspired by the effective area. Dividing the neutrino maps by the above maps gives an approximation to the spatial distribution of the incident neutrino flux. The IceCube response is more isotropic at low energy and increases at the horizon at high energy.

These tools are based on simulations of the detector performance or on real data that has been "scrambled" such that the spatial information is destroyed.

Signal neutrino sets can be generated using purely simulated neutrinos. First, an ensemble of neutrino events are sampled from a uniform distribution on the celestial sphere and following a flat energy distribution. Each neutrino is assigned a weight called "oneweight" which allows the events to be reweighted to whatever spectrum is desired. Further weights are multiplied with the "oneweight" value to describe the probability of seeing that event under a specific signal hypothesis. For a point source, the weight is the Gaussian profile located at a source hypothesis location with a width equal to the reconstruction error of that signal event. For a template source, the weight is the template after blurring with a PSF corresponding to the reconstruction error of that event. After

each event has been assigned a weight, the events can be randomly drawn with probability proportional to the weights.

Atmospheric neutrino sets can be created similarly. The events are given a weight corresponding to their probability as inferred from MCEq (Fedynitch et al., 2015). These weights can be used to sample simulated events. The number of simulated events to draw from the ensemble is set equal to the observed events in the real data because the real data is dominated by atmospheric neutrinos.

Alternatively, the real data can be used to generate realistic data sets. IceCube is located at the South Pole and the design of IceCube produces an effective area which depends only on the angle of the neutrino above the horizon. These two facts allow a convenient method of randomizing real data while preserving the detector response to each event. The right ascension of each real event is given a random offset between 0 and 2π. This offset does not affect the declination or energy, so the detector response to an event like that one is unchanged. This right ascension scrambling destroys the spatial information.

5.5 Cross Correlation Likelihood Formalism

The cross-power spectra are related to the true power spectra of the large-scale matter distribution, C_ℓ^{mm}, by linear bias factors,

$$C_\ell^{gg} = b_g^2 \, C_\ell^{mm} \tag{5.5}$$

$$C_{\ell\, i}^{g\nu,\,\mathrm{corr}} = b_\nu \, b_g \, C_\ell^{mm} \tag{5.6}$$

$$C_{\ell\, i}^{\nu\nu,\,\mathrm{corr}} = b_\nu^2 \, C_\ell^{mm} \tag{5.7}$$

The bias parameters are typically $\mathcal{O}(1)$. Substituting Equation 5.5 into Equation 5.6 finds that

$$C_{\ell\, i}^{g\nu,\,\mathrm{corr}} = \frac{b_\nu}{b_g} C_\ell^{gg}. \tag{5.8}$$

The "corr" in the superscript refers to the fact that the IceCube data set contains both astrophysical events which are follow the matter power spectrum and background events which are uncorrelated. In the case of IceCube, the neutrino catalog is composed of three populations, astrophysical neutrinos which are correlated with the large-scale structure, astrophysical neutrinos that are not correlated with the large-scale structure, and the atmospheric neutrinos which will have their anisotropic spatial distribution determined by the interaction of cosmic rays with the Earth's atmosphere. The correlated astrophysical neutrinos are produced in sources that exist in the same redshift range as the unWISE-2MASS catalog. The uncorrelated astrophysical neutrinos may be produced outside the redshift range traced by the unWISE-2MASS catalog, or they might be produced following some other spatial distribution. Both of these source distributions will also be affected by the declination-dependent effective area of IceCube, but the weight map removes this effect.

Fang et al. (2020) have shown that the power spectrum of a multi-component population of events in reconstructed energy bin i can be decomposed additively,

$$C_{\ell i}^{g\nu} = f_{\text{corr},i}\, C_{\ell i}^{g\nu,\,\text{corr}} + f_{\text{uncorr},i}\, C_{\ell i}^{g\nu,\,\text{uncorr}} + f_{\text{atm},i}\, C_{\ell i}^{g\nu,\,\text{atm}}. \tag{5.9}$$

The parameters $f_{\text{corr},i}$, $f_{\text{uncorr},i}$, and $f_{\text{atm},i}$ refer to the fraction of neutrinos coming from sources which are correlated with the unWISE-2MASS catalog, uncorrelated with the catalog but still astrophysical, and follow an atmospheric distribution. These fractions are constrained to

$$f_{\text{corr},i} + f_{\text{uncorr},i} + f_{\text{atm},i} = 1. \tag{5.10}$$

By definition, $C_{\ell i}^{g\nu\ \text{uncorr}} = 0$, so Equation 5.9 simplifies to For simplicity and lack of further information, we fix $b_\nu = b_g$. Deviations from that assumption will be discussed in the interpretation.

$$C_{\ell i}^{g\nu} = f_{\text{corr},i}\, C_{\ell i}^{g\nu,\,\text{corr}} + f_{\text{atm},i}\, C_{\ell i}^{g\nu,\,\text{atm}}. \tag{5.11}$$

Equation 5.11 applies to each energy bin individually. All the energy bins will be treated together within the likelihood to maximize the statistical significance, so Equation 5.11 will be reparameterized in terms of a single correlation strength, f_{corr}, and spectral index, γ, assuming the astrophysical events follow a power law distribution. Thus,

$$C_{\ell i}^{g\nu} = f_{\text{corr}}\, \kappa_i(\gamma)\, C_{\ell}^{gg} + f_{\text{atm},i}\, C_{\ell i}^{g\nu,\,\text{atm}} \tag{5.12}$$

where $\kappa(\gamma)$ is the ratio of detector acceptance in the given energy bin for a given spectral index ($A_i(\gamma)$) divided by the acceptance across the entire energy range for the same spectral index ($A(\gamma)$), ie, $\kappa(\gamma) = \frac{A_i(\gamma)}{A(\gamma)}$ and

$$f_{\text{corr}} \equiv \frac{b_\nu}{b_g} \frac{n_{\text{corr}}}{n_{\text{total}}}. \tag{5.13}$$

Equation 5.13 is exactly true when the astrophysical neutrinos are Poisson sampled from the unWISE-2MASS galaxies. The cross-power spectra in different energy bins are linked by a single correlation strength and spectral index.

At large ℓ, $C_{\ell}^{g\nu,\,\text{atm}} \approx 0$, reflecting the smooth distribution of atmospheric neutrinos and the IceCube effective area. At small angular scales, the anisotropy of the atmospheric neutrinos can be neglected. For $\ell < 50$, the anisotropy of the atmospheric neutrinos cannot be neglected and must be included in any model. Because IceCube has a $\sim 1^\circ$ PSF, much of the power is already attenuated above $\ell > 50$. To maximize the sensitivity, information at large scales must be included. This is addressed in Section 5.7.

Because this study is focused on searching for the sources of astrophysical neutrinos rather than a high-fidelity cosmology study, we do not attempt to determine the true cross-power spectrum. Instead, we adopt a forward-modeling approach in the statistical evaluation of the cross-power spectrum, thus all the cross-power spectra referred to below are to the textitobserved quantities which point spread function rather than the *true* quantities.

We assume that the measured cross-power spectra follow a multivariate normal distribution. The use of a mask causes the individual multipoles in the cross power spectrum to be coupled. The PSF and atmospheric event distribution depend on energy, so the events are binned into three bins of reconstructed energy, labeled with index i.

$$\log\left(\mathcal{L}\right) = \sum_i -\frac{1}{2}\,\vec{x}_i^{\,T}(\vec{\theta})\,\Sigma^{-1}\,\vec{x}_i(\vec{\theta}) + \text{constant} \tag{5.14}$$

where $\vec{\theta} = (f_{\text{corr}}, \gamma, f_{\text{atm},1}, f_{\text{atm},2}, f_{\text{atm},3})$ and

$$\vec{x}_i(\vec{\theta}) = C_{\ell\,i}^{g\nu} - \left(f_{\text{corr}}\,\kappa_i(\gamma)\,C_{\ell\,i}^{gg} + f_{\text{atm},i}\,C_{\ell\,i}^{g\nu,\,\text{atm}}\right) \tag{5.15}$$

and Σ^{-1} is the inverse covariance matrix.

5.6 Astrophysical Model Estimation

A model for the expected astrophysical signal in each bin $C_{\ell,i}^{g\nu}$ is necessary to fit the degree of correlation between the two catalogs. The mapping between the true cross-power spectrum and the observed cross-power spectrum would typically be described by $C_\ell^{g\nu,\text{obs}} = B_\ell^g\,B_\ell^\nu C_\ell^{g\nu,\text{true}}$ where B_ℓ^g and B_ℓ^ν are the beam functions (related to the point spread functions and pixelization) of the galaxy and neutrino maps assuming a PSF which is radially symmetric about the source and the same in every direction. See Chapter 3 for more details. In the formalism above, we would find the observed $C_\ell^{g\nu,\text{corr}} = B_\ell^g\,B_\ell^\nu C_\ell^{gg}$. The PSF of the galaxy catalog is essentially perfect at the scales used in this analysis, but the pixelization needs to be taken into account. The IceCube PSF is not the same at every latitude, so more careful modeling is necessary. We directly estimate the observed C_ℓ^{gg} in each energy bin through Monte Carlo sampling. The IceCube collaboration has created detailed simulations of the detector response to an impulse flux which can be reweighted to match whatever spatial distribution and energy spectrum is desired. We use these

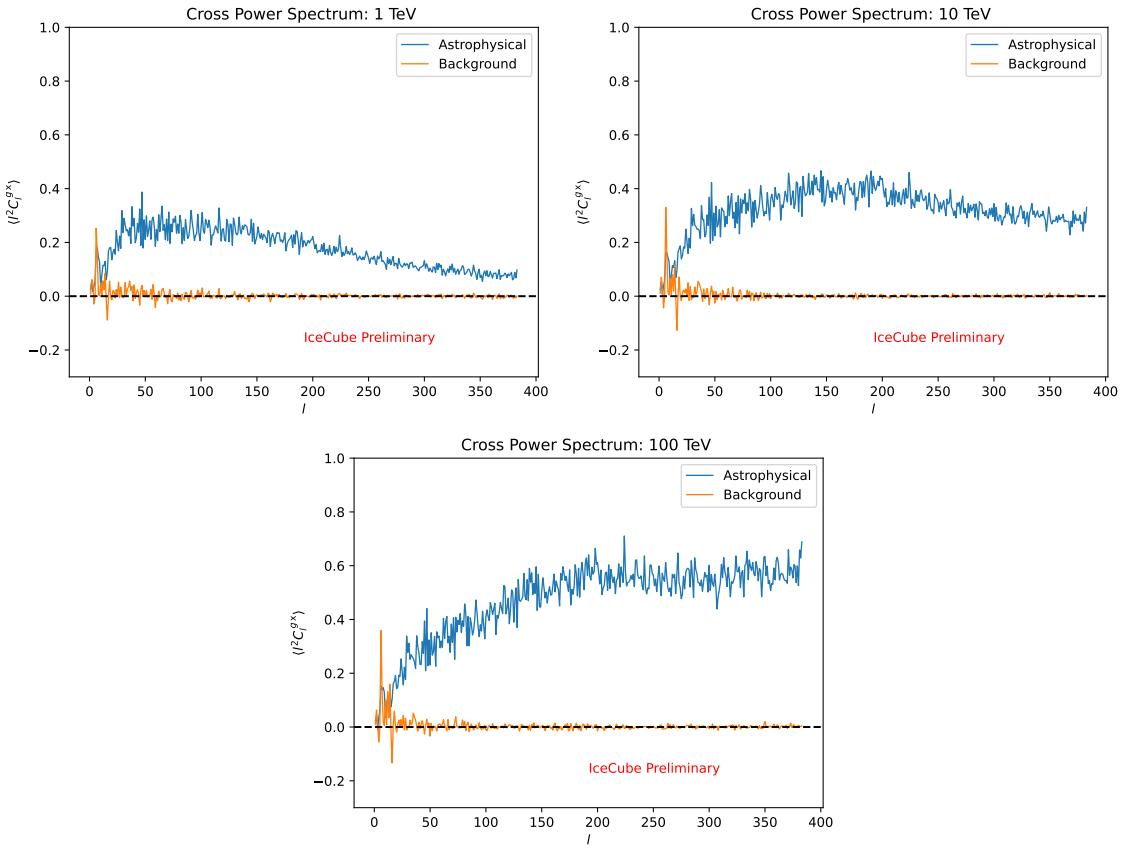

Figure 5.6: **IceCube unWISE-2MASS Cross-Correlation Model Templates.** The model expectations for a purely astrophysical (blue) and purely atmospheric sample (orange) in each energy bin are shown above.

simulations to construct 1000 purely astrophysical neutrino data sets which are Poisson sampled from the unWISE-2MASS template including the effects of the IceCube point spread function and sky pixelization. In these simulations, we use a neutrino energy spectrum following a power law with an index equal to 2.5. Although we later fit the energy spectrum as a free parameter, the choice of energy spectral index in each energy bin has a negligible effect. We plotted the model template for different spectral indices between 2.0 and 3.0. The models were indistinguishable. The model astrophysical $C_\ell^{g\nu,\,\mathrm{corr}}$ are shown in Figure 5.6. The blue models in this figure can be compared with the galaxy autocorrelation shown in Figure 5.4 to get a sense of the effective beam function.

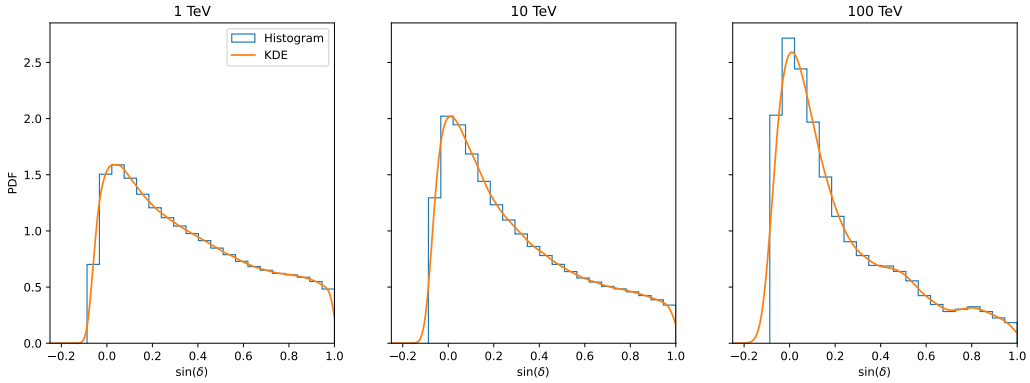

Figure 5.7: **Kernel Density Estimate of Atmospheric Neutrinos.** The kernel density estimate of atmospheric neutrinos is used to estimate the background model by applying the value of the function to a HEALPix map and computing the cross-correlation with the unWISE-2MASS catalog.

5.7 Atmospheric Model Estimation

A model for the atmospheric contribution to the cross-correlation is necessary when using multipoles with $\ell < 50$. The model can be generated similarly to the atmospheric model; however I generate it in two ways to serve as a cross check on the accuracy of the model. The first uses real data that has been scrambled in right ascension. A Gaussian kernel density estimate over the sine of the declination is calculated to form a continuous function as a function of declination. The value of this KDE of declination is then applied to every pixel in a HEALPix map, and that map is cross-correlated with the unWISE-2MASS map. The resulting cross-spectrum is the model template for the atmospheric neutrinos. These models are shown in Figure 5.6 in orange. Additionally, the model was estimated using Monte Carlo simulated data following the same KDE procedure. The KDE and data histogram are shown in Figure 5.7. The comparison of the data-driven and MC atmospheric models is shown in Figure 5.8.

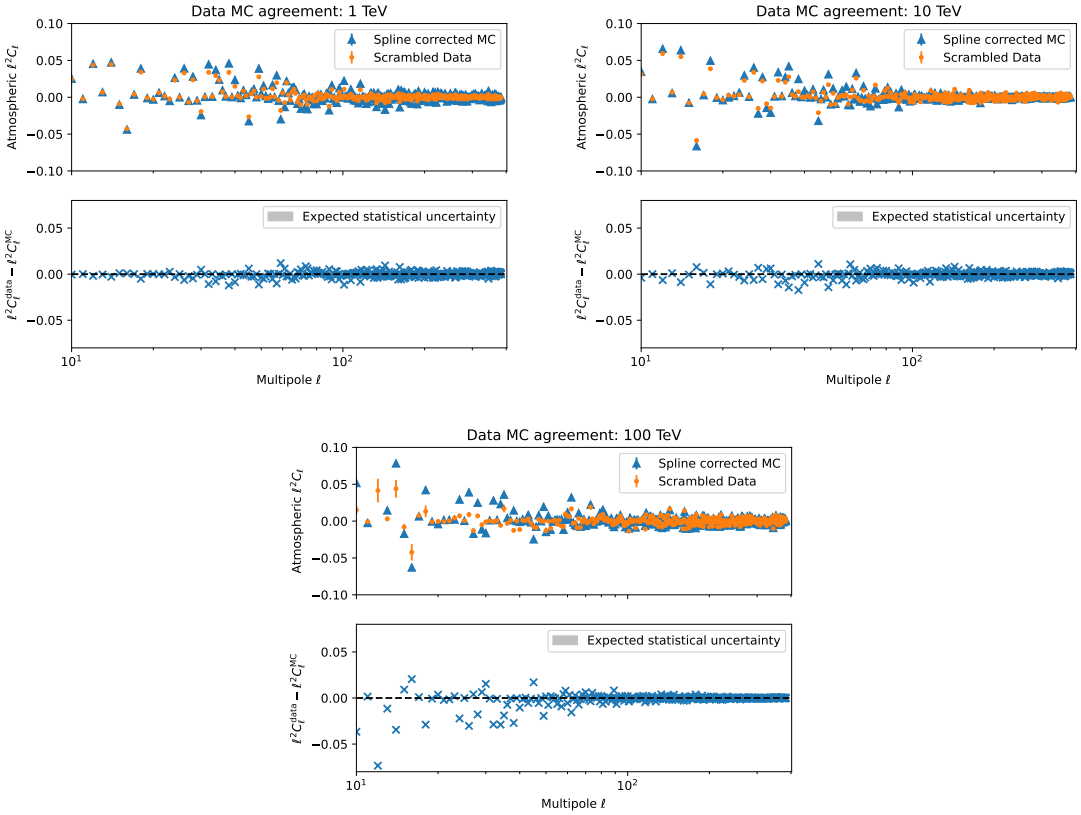

Figure 5.8: **Atmospheric Model Template MC-Data Agreement.** The atmospheric model template is calculated in two ways: (1) from data and (2) from Monte Carlo simulations. The atmospheric model is calculated for both and compared with the expected statistical uncertainty of the cross-correlation measurement (gray region). In all energy bins, the statistical uncertainty is larger than the systematic difference between the data-driven and MC models.

5.8 Covariance Matrix Estimation

The use of a sky mask causes mode-coupling, so we need to estimate the covariance between multipoles. Although an analytic expression for the covariance is shown in Chapter 3, the expression is cumbersome to evaluate. It is more straightforward to estimate the covariance using numerical simulations. The covariance is dominated by atmospheric neutrinos. The covariance matrix is estimated by creating 10^5 sets of atmospheric-only data similar to 5.7. The cross-correlation is computed using these synthetic data sets, and then the covariance is calculated for each mode in each energy bin. Energy bins are assumed to be independent.

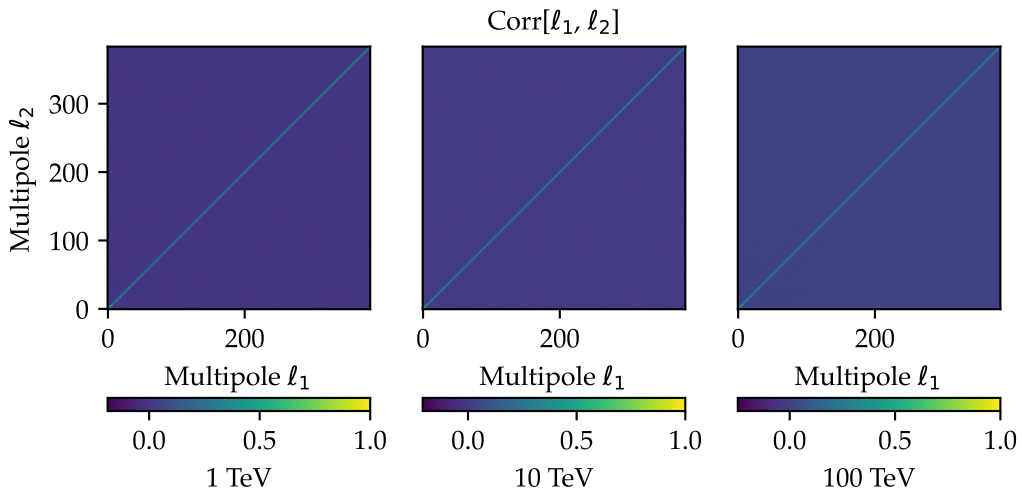

Figure 5.9: **unWISE-2MASS Multipole Correlation Matrix.** The correlation matrix $\mathrm{Corr}[\ell_1, \ell_2] = \frac{\mathrm{Cov}[\ell_1,\ell_2]}{\sigma_{\ell_1}\sigma_{\ell_2}}$ between the multipoles for each energy bin is shown above. The off-diagonal elements are small but not negligible.

The correlation matrices derived from these covariance matrices are shown in Figure 5.9.

5.9 Hypothesis Testing

The statistical analysis used in Chapter 5 follows the standard procedure for frequentist hypothesis testing. The hypothesis testing procedure is described in Appendix A. The test hypothesis in this analysis is that there is a correlated astrophysical component in the IceCube data. This corresponds to the statement $f_{\mathrm{corr}} > 0$. The complement to this hypothesis is the test hypothesis: $f_{\mathrm{corr}} = 0$. In the test hypothesis, I also allow γ to remain a free parameter within the range $1 \leq \gamma \leq 4$ in the test hypothesis only. The remaining parameters are nuisance parameters, so they are allowed to vary in both the test and null hypothesis fits. It is theoretically possible to measure a negative correlation. An anti-correlation would suggest that neutrinos preferentially arrive from directions that correspond to voids in the large-scale structure. This would likely require some beyond-standard-model physics to explain. Because there have been neutrinos observed from AGN, and that AGN are correlated with the large-scale structure, the anti-correlation hypothesis

is excluded.

The test statistic used in this analysis is the log-likelihood ratio:

$$\text{TS} = 2\log\left(\frac{\mathcal{L}(\{C_{\ell i}^{g\nu}\}|\hat{f}_{\text{corr}}, \hat{\gamma}, \hat{f}_{\text{atm},1}, \hat{f}_{\text{atm},2}, \hat{f}_{\text{atm},3})}{\mathcal{L}(\{C_{\ell i}^{g\nu}\}|0, 0, \hat{f}_{\text{atm},1}, \hat{f}_{\text{atm},2}, \hat{f}_{\text{atm},3})}\right). \tag{5.16}$$

The hats indicate that the parameter is the value that maximizes the likelihood. As discussed in Section 5.5 and the following sections, the likelihood $\mathcal{L}$ is a multivariate Gaussian distribution. The optimization of the atmospheric parameters is performed independently for the test and null hypotheses.

The next step is to derive the test statistic distribution under the null hypothesis,

$$P(\text{TS}|\text{null}) = P(\text{TS}|0, 0, \hat{f}_{\text{atm},1}, \hat{f}_{\text{atm},2}, \hat{f}_{\text{atm},3}). \tag{5.17}$$

The two astrophysical parameters are bounded, and the null hypothesis lies on the boundary of the fit space for f_{corr}, so these hypotheses do not meet the criteria for Wilke's theorem (Wilks, 1938). In this case, I numerically simulate background-only data sets and evaluate the test statistic for each one to obtain a null hypothesis test statistic distribution. The test statistic distribution is shown in Figure 5.16. This obtained test statistic is shown on the abscissa of Figure 5.16.

5.10 Estimator Bias

For any inference problem, it is important to validate that the estimators are unbiased or to be able to correct for any bias. Recall that

$$f_{\text{corr}} = \frac{b_\nu}{b_g}\frac{n_{\text{corr}}}{n_{\text{total}}}. \tag{5.18}$$

when neutrinos are sampled from the unWISE-2MASS galaxies. The bias parameters are not constrained, but generally $b_g \approx b_\nu$ in most cross-correlation problems. The estimator bias is measured using numerical simulations where a realistic background and signal are generated from Monte Carlo events. The astrophysical signal is Poisson sampled from the galaxy template, so the bias parameters are equal by design. The background is held fixed while the number of correlated neutrinos injected, n_{inj}, is increased. The injected spectral index γ_{inj} is held fixed. The likelihood maximization is performed for several such trials to estimate the distribution of estimators averaged over data.

The bias of the estimators for the number of correlated neutrinos and the correlated neutrino spectral index is shown in Figure 5.10. For harder spectral indices (ie. smaller values for γ_{inj}), the estimators are relatively unbiased. The number of correlated neutrinos is unbiased except for very weak signals. The spectral index is biased at low signal injection and recovers at higher injection. At softer spectral indices, the bias has the same trend in both estimators but has a larger impact. This is likely due to the soft spectral index of the atmospheric neutrinos. Atmospheric neutrinos follow a roughly $\gamma_{\text{atm}} = 3.7$, so there may be some confusion between astrophysical and atmospheric neutrinos.

5.11 Systematic Uncertainties

Systematic uncertainty arises from various unmodeled or mismodeled effects that can affect the inference process. Often, systematic uncertainty can be mitigated using data-driven methods. The atmospheric model used in the cross-correlation has been compared with an atmospheric model generated using simulated events. The resulting models are consistent with the expected statistical uncertainty of the cross-correlation. The systematic effect of the detector calibration on the entire analysis pipeline was evaluated using simulated data sets. The simulated data sets were created with the nominal simulated data set and the fit was performed with models generated with simulated data sets with detector configuration

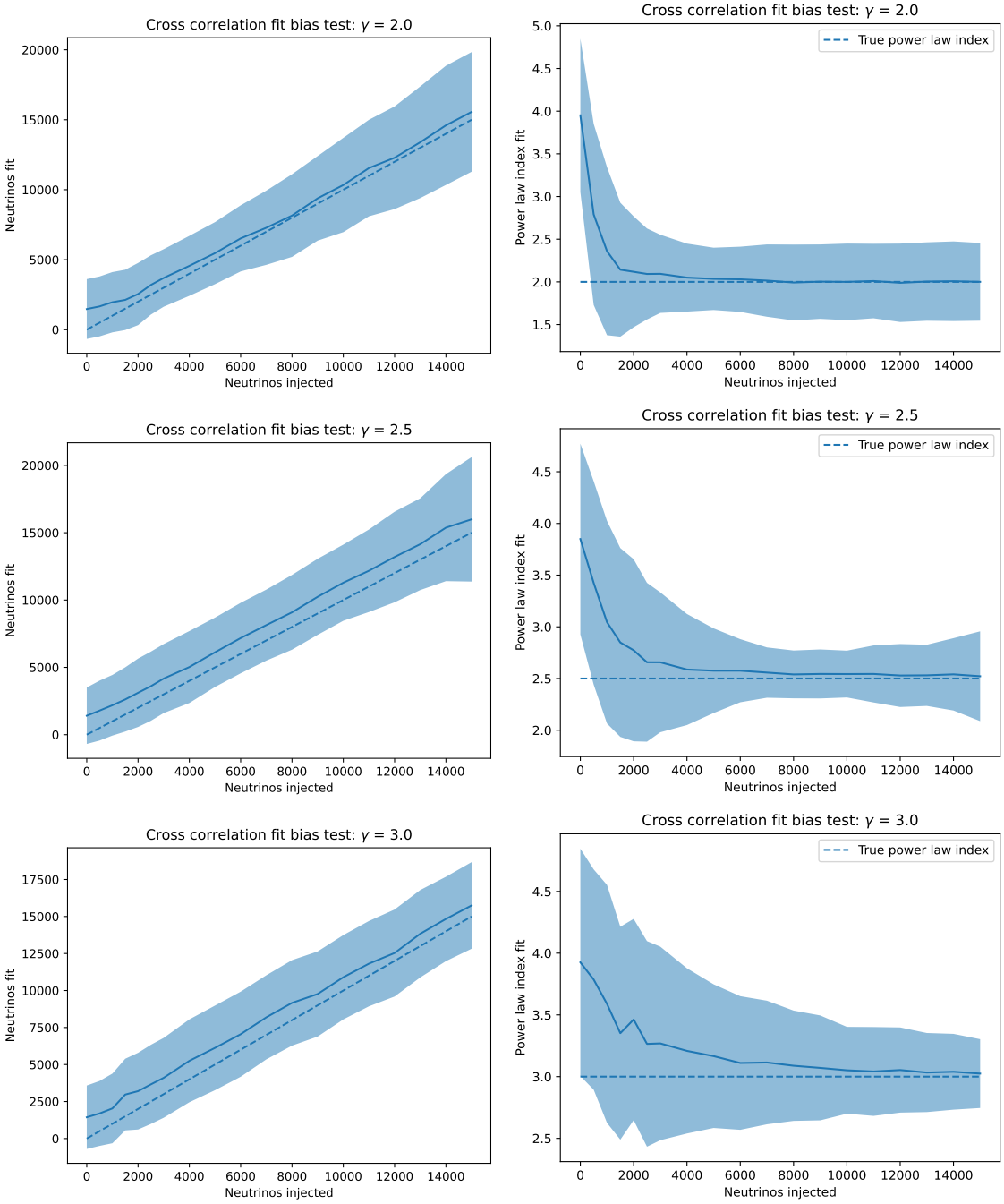

Figure 5.10: **Bias of Astrophysical Fit Parameters.** The distribution of the astrophysical parameter estimators is shown as a function of the injected signal. The astrophysical correlation strength is related to the number of correlated neutrinos by Equation 5.18. The correlation is slightly biased for softer spectral indices. The spectral index is biased for weak signal strengths.

Systematic varied	Value	Description
DOM Efficiency	$\pm 10\%$	Ratio observed and simulated DOM photoelectrons
Hole Ice P0	± 1	Hole ice scattering parameter
Ice scattering	$\pm 5\%$	Scattering of photons in ice
Ice absorption	$\pm 5\%$	Scattering of photons in ice

Table 5.1: **Parameters Varied in Systematic Uncertainty Estimation.** Variations in these parameters were considered while estimating systematic uncertainty in the fit results.

and ice properties varied. Two tests were run. The first used simulated data sets with only atmospheric neutrinos. The second used a realistic level of signal injection, about 2500 correlated neutrinos. The simulated data sets are summarized in Table 5.1.

The systematic uncertainty is defined as

$$\sigma_{f,\text{sys}} = \max_i(|f_i - f_{\text{nominal}}|) \tag{5.19}$$

and

$$\sigma_{\gamma,\text{sys}} = \max(|\gamma_i - \gamma_{\text{nominal}}|) \tag{5.20}$$

where i indexes the set of MC systematic data sets. The histogram of fractional uncertainties from the simulated data sets is shown in Figure 5.11. The average fractional systematic uncertainty on the correlation strength is approximately 20% and the average fractional systematic uncertainty on the spectral index is approximately 5%.

5.12 Goodness of Fit

The consistency of the model with the data can be quantified by measures of the goodness of fit. The most common goodness of fit measure is the χ^2. The χ^2 goodness of fit including a covariance matrix is defined as

$$\chi^2 = \sum_{i=1}^{3} \vec{x}_i(\vec{\theta})^T \, \Sigma^{-1} \, \vec{x}_i(\vec{\theta}). \tag{5.21}$$

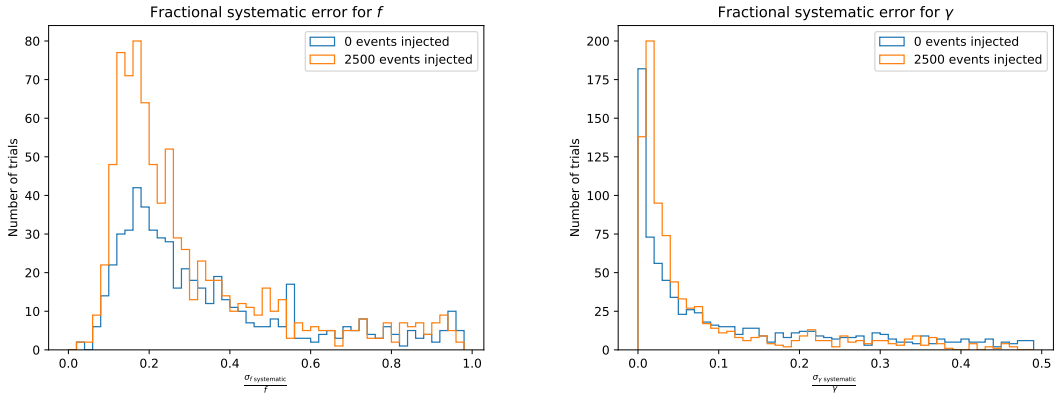

Figure 5.11: **Fractional Systematic Uncertainty.** The histogram of fractional systematic uncertainty for all trials run with and without signal injection. The fractional uncertainty on the normalization is approximately 20% and the spectral index is approximately 5%.

If the model is consistent with the data, the χ^2 defined in Equation 5.21 will be distributed following a χ^2 distribution with 1114 degrees of freedom because there are three energy bins with 373 multipoles each and five free parameters. Simulated data sets were created with only atmospheric events and the goodness of fit was evaluated for each one. The histogram of the goodness of fits is shown in Figure 5.12. The goodness of fit is nearly consistent with the expected distribution. There is a slight bias towards larger values. This is likely due to the noise in the signal and atmospheric model templates.

5.13 Stress Tests

The cross-correlation should be robust to uncorrelated neutrino backgrounds; however, it is useful to verify these assumptions. There are several different background that could potentially cause some degree of confusion between the desired signal and undesired backgrounds. Three backgrounds are explored in this section.

1. Individual bright neutrino point sources like NGC 1068

2. Isotropic neutrino diffuse background

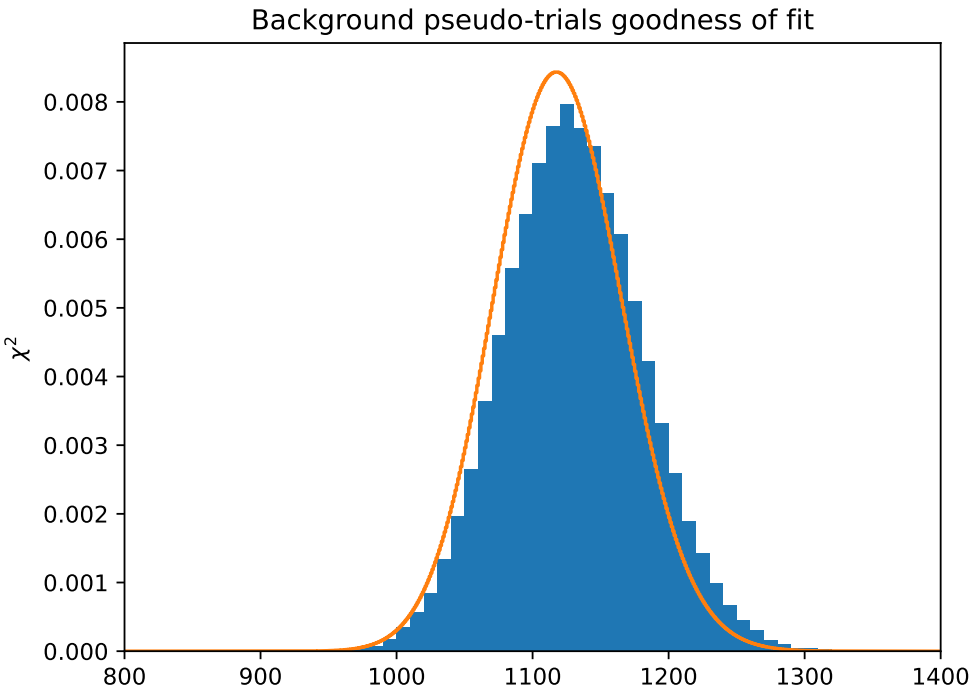

Figure 5.12: **Cross-Correlation Goodness-of-Fit.** The cross-correlation goodness-of-fit was evaluated for pseudo-trials to ensure that the best fit model describes the data well. Although there is a small shift to the right, overall the goodness-of-fit was reasonable.

3. Uncorrelated anisotropic diffuse background.

Bright Neutrino Point Sources

NGC 1068 is known to be a neutrino source. It was discovered in the same data set used in this cross-correlation. The inferred neutrino flux was approximately 88 neutrinos, while the expected diffuse astrophysical neutrino flux is expected to be around 2500 neutrinos. The effect of individual neutrino sources was assessed by creating purely atmospheric simulated data sets and then injecting a point source at the location of NGC 1068. As a baseline, a set of trials was run without any point source. Two additional sets of trials were run. The first injected a flux equal to the measured flux of NGC 1068 and the second injected twice that signal. The test statistic distributions for those three cases are shown in Figure 5.13. The cases with no NGC 1068 and realistic NGC 1068 are virtually identical.

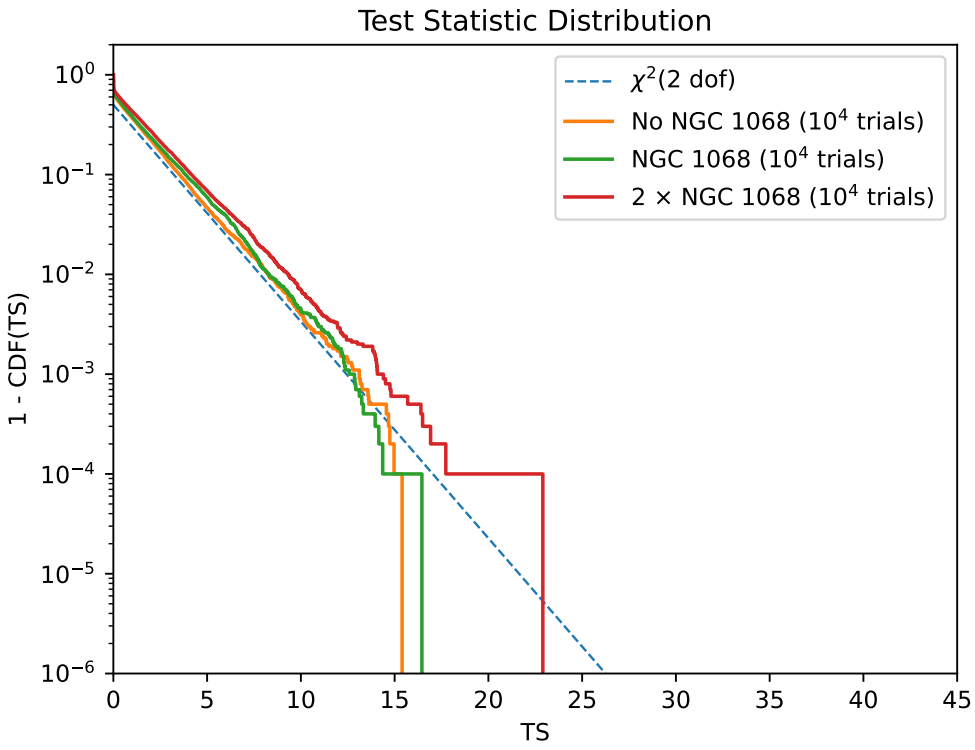

Figure 5.13: **Test Statistic Distribution Including Bright Point Sources.** The test statistic distribution in the case of atmospheric-only events and atmospheric events plus NGC 1068 are shown above. The test statistic distributions are compatible suggesting that a point source like NGC 1068 will not affect the analysis.

The case with NGC 1068 twice as bright as measured has a small tail in the test statistic distribution but is not significant enough to cause a false positive. Regardless of the tail, if there were another source twice as bright as NGC 1068, it would have been found in point source searches. The cross-correlation method is not affected significantly by unknown bright point sources.

Isotropic Background

It is useful to know how a truly isotropic background affects the measurement of the cross-correlation. In theory, an isotropic background is completely removed when the map overdensity is calculated, but the Poisson noise from those events remains in the data. The method should be robust to this excess noise. Data sets with atmospheric neutrinos and

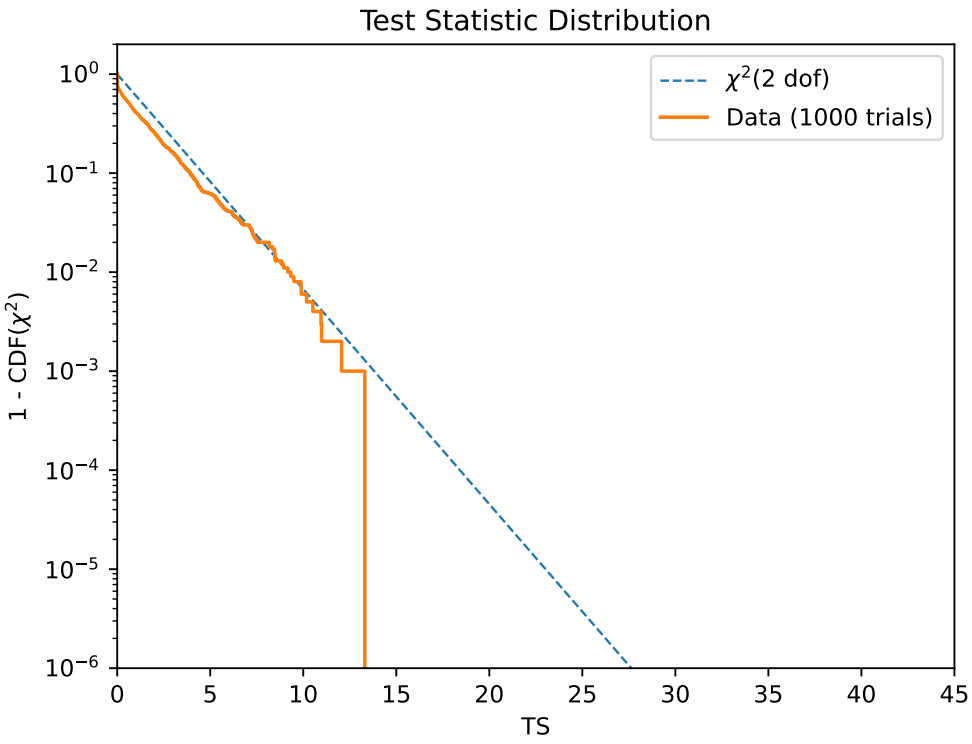

Figure 5.14: **Test Statistic Distribution Including Isotropic Background.** The test statistic distribution in the case of atmospheric-only events and atmospheric events plus and uncorrelated isotropic background are shown above. The test statistic distributions are compatible suggesting that an isotropic background will not affect the analysis.

an isotropic background with 3.5 times the diffuse neutrino flux were created and the test statistic was calculated. The resulting test statistic distribution is shown in Figure 5.14. It is consistent with background.

Uncorrelated Large-Scale Structure

Some fraction of the diffuse neutrino flux likely comes from a redshift range outside of the range probed by the unWISE-2MASS catalog. It is useful to know how such a background would affect the measurement of the correlation with the local large-scale structure. To test this possibility, a simulated large-scale structure template was created. The angular power spectrum of the unWISE-2MASS sky map is shown in Figure 5.4. Recall that each multipole ℓ in the angular power spectrum is a sum over numerous spherical harmonic moments

$-\ell < m < \ell$, so many sky maps correspond to the same power spectrum. A realistic sky map with the same power spectrum as the unWISE-2MASS power spectrum using the Healpy routine `synfast`. This routine creates a skymap with spherical harmonic coefficients randomly drawn as Gaussian random variables. Simulated data sets were generated with signal sampled from this sky map. The data sets consist of atmospheric neutrinos and signal neutrinos tracing the synthetic large-scale structure with signal injection up to 5 times the diffuse neutrino flux. The simulated data were cross-correlated with the actual unWISE-2MASS galaxy overdensity. The resulting test statistic distribution is shown in Figure 5.15. The test statistic distribution is completely consistent with the background-only test statistic distribution. This demonstrates that the cross-correlating is not sensitive to neutrinos that have anisotropy that is different from the unWISE-2MASS anisotropy.

5.14 Results

The results of the cross-correlation analysis were kept blinded until the working group and collaboration agreed that the analysis method was mature and reliable. This section contains the unblinded results. The likelihood maximization was performed as described in Section 5.9. The resulting test statistic is shown in Figure 5.16 with the test statistic distribution for the null hypothesis shown for reference. The observed test statistic was 2.307. The p-value measured with reference to the numerical test statistic distribution is 0.23. This is a deviation of 1.21σ. In comparison with either the analytic estimate for the test statistic distribution or the numerical estimate, this is clearly not a significant result.

The best fit parameters for the null hypothesis and the test hypothesis are shown in Table 5.2 and the likelihood is shown in color and with contours in Figure 5.20. In both the test hypothesis fit and null hypothesis fit, the atmospheric fit parameters are nearly equal to one for the lower two energy bins. This is consistent with what is known about the northern sky track-like event selection. It is background dominated at low energy.

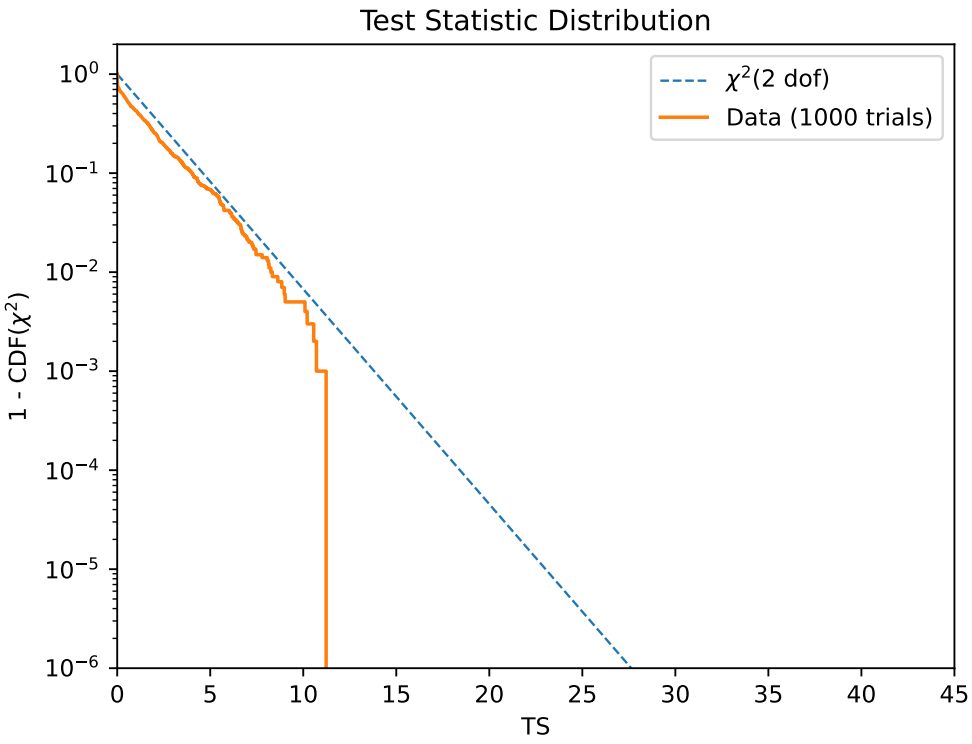

Figure 5.15: **Test Statistic Distribution Including Uncorrelated Large Scale Structure Background.** The test statistic distribution in the case of atmospheric-only events and atmospheric events plus and uncorrelated but realistic large-scale structure are shown above. The test statistic distributions are compatible suggesting that an uncorrelated large-scale structure background will not affect the analysis.

At higher energy, the atmospheric fraction is approximately 0.89 for both fits. Recalling that the three components must sum to one (Equation 5.10), and that $f_{\text{corr}} = 0$ in the null hypothesis fit, that suggests that 21% of the neutrinos come from uncorrelated sources.

The data was well-described by the maximum likelihood test hypothesis model. The χ^2 goodness-of-fit was 1077.9 and there were 1117 degrees of freedom. For a χ^2 distribution with k degrees of freedom, the mean is k and the standard deviation is $\sqrt{2k}$. The observed χ^2 is -0.83σ from the mean. This is well within expectation and indicates that the model is consistent with the data.

The test hypothesis fit found $f_{\text{corr}} = 0.11$ and a spectral index of $\gamma = 4.0$. The likelihood was maximized by an extremely soft spectral index which lies on the bound of the allowed fit space. A spectral index of 4.0 is even greater than the atmospheric neutrino spectral

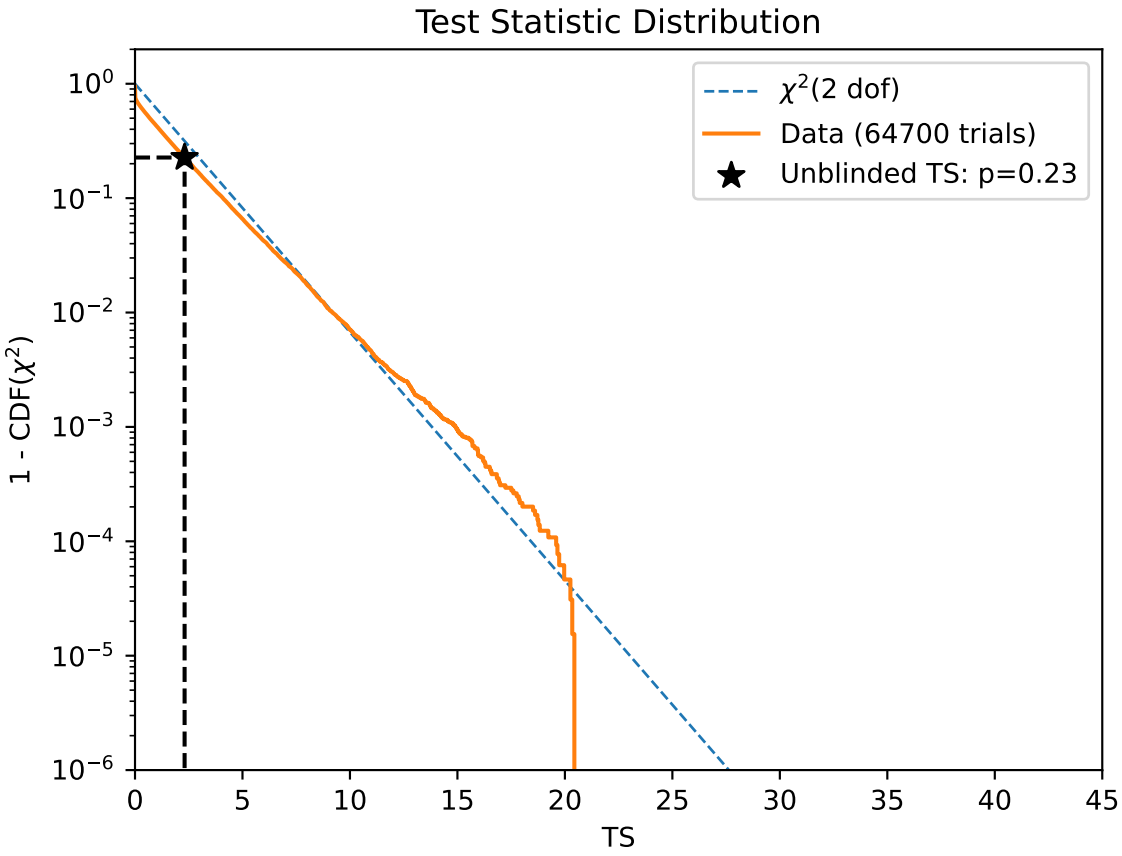

Figure 5.16: **Cross Correlation Test Statistic Distribution.** The numerical and analytic expectations for the test statistic distribution are shown above with the unblinded test statistic. The unblinded test statistic is compatible with the test statistic distribution suggesting that there was no statistically significant effect.

index, suggesting that the fit was not finding an astrophysical component. Instead, it may have identified unmodeled residuals in the distribution of atmospheric neutrinos. It may also have simply been a random fluctuation that appeared as a softer spectrum. Regardless, the null hypothesis cannot be rejected, so the fit parameters do not contain physical significance.

An upper limit on the strength of the correlation can be derived by assuming a fixed spectral index. The most natural choice for the spectral index is the best fit spectral index from the diffuse fit of the same data set. This is an index of $\gamma = 2.37$. The 90% confidence

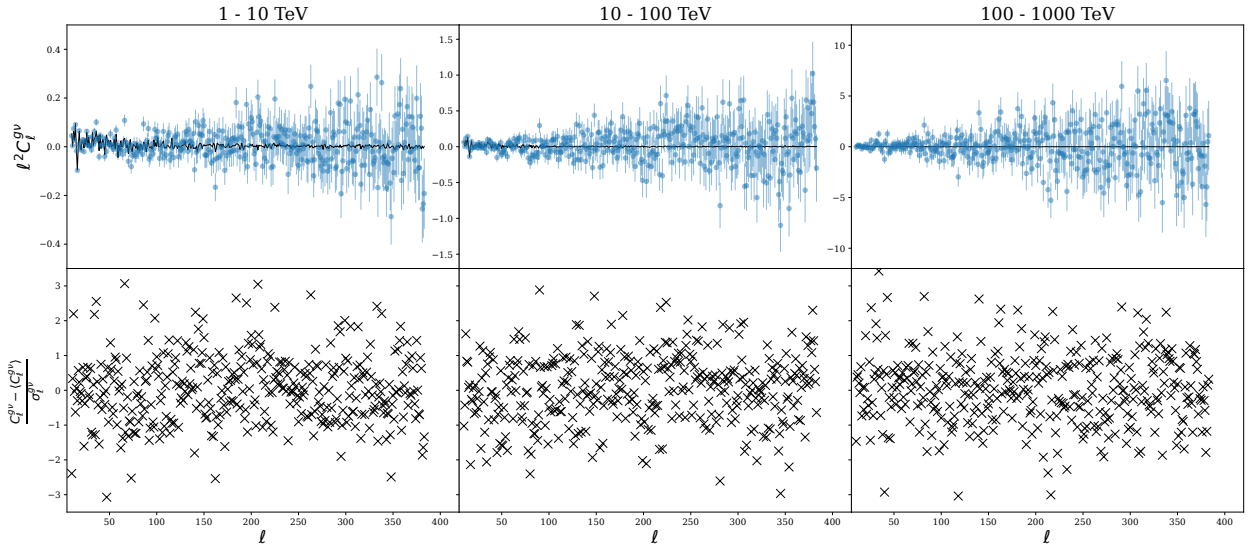

Figure 5.17: **Unblinded Cross Power Spectra.** The cross power spectra in each energy bin are shown in blue dots in the upper panels with the best fit test hypothesis model. The lower panels show the residuals with respect to that model.

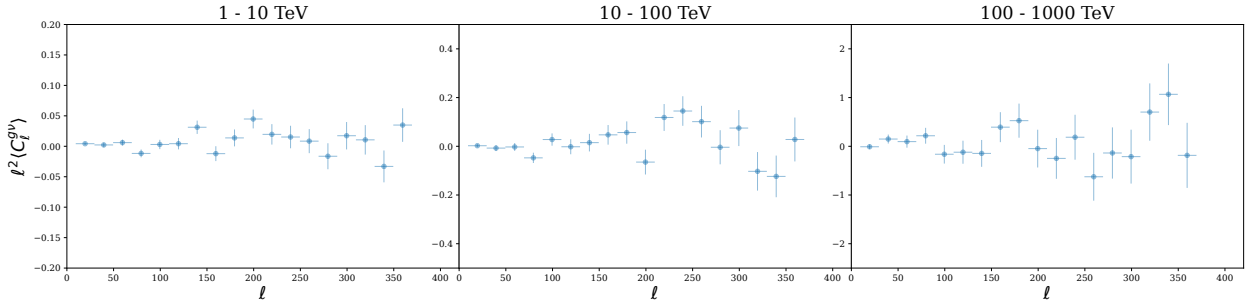

Figure 5.18: **Binned Residual Cross Power Spectra.** The cross power spectra in each energy bin are shown in blue dots. The cross power spectra have had the atmospheric expectation subtracted and have been binned by a factor of 20 in ℓ. The error bars are the standard error of the mean neglecting off-diagonal elements of the covariance matrix. The uncertainties should be treated as lower limits to the actual uncertainty. The cross spectra are consistent with no power.

upper limit for f_{corr} is defined as the maximum value that the parameter can take it has a 90% chance of lying between that value of f_{corr} and zero. This is equivalent to solving

$$0.9 = \text{CDF}(). \tag{5.22}$$

The cumulative distribution function for f_{corr} is shown in Figure 5.21. The inversion was

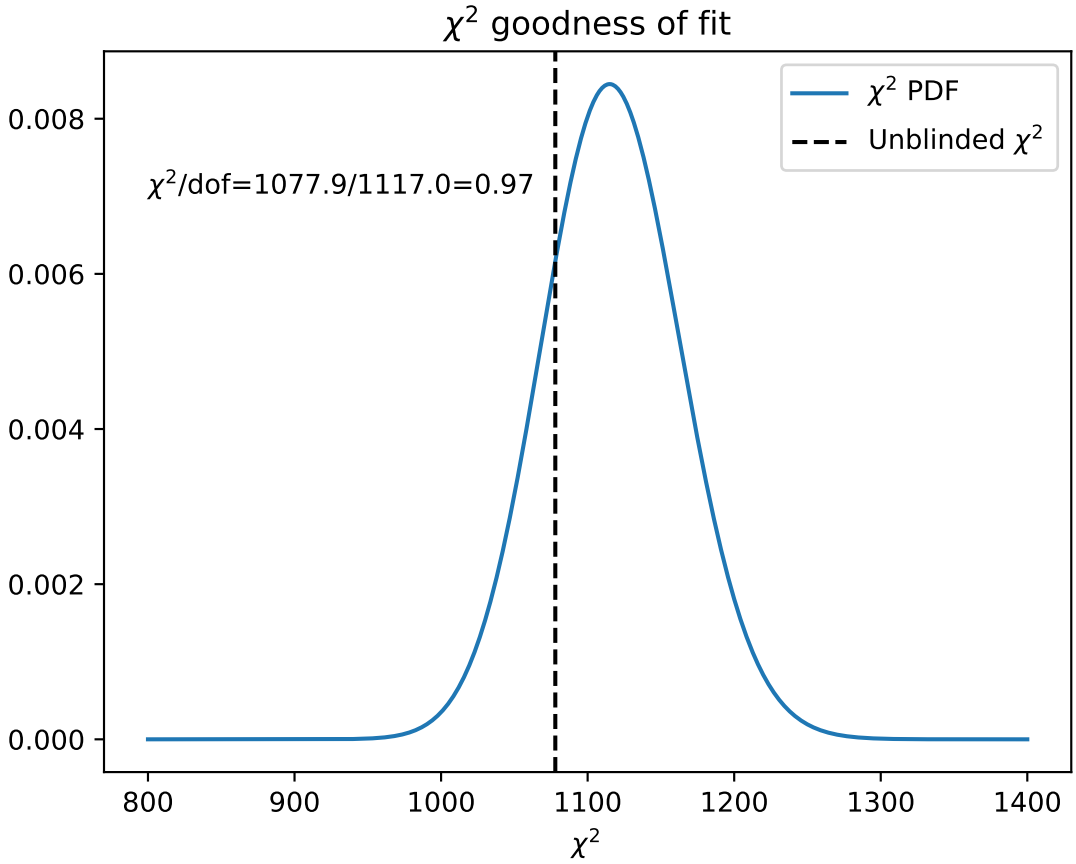

Figure 5.19: **Unblinded Goodness of Fit.** The goodness of fit of the test hypothesis is consistent with the theoretical expectation for the number of degrees of freedom included in the fit.

done by calculating the CDF at evenly spaced intervals, then using a spline to calculate the correlation strength at which the CDF is equal to 0.9. The resulting upper limit is $f_{\text{corr}} < 0.0078$.

5.15 Summary

The two-point angular cross-correlation of IceCube neutrinos and infrared galaxies can be used to constrain the origins of the diffuse astrophysical neutrino flux. The neutrino maps are created in three reconstructed energy bins and are weighted by the effective area before

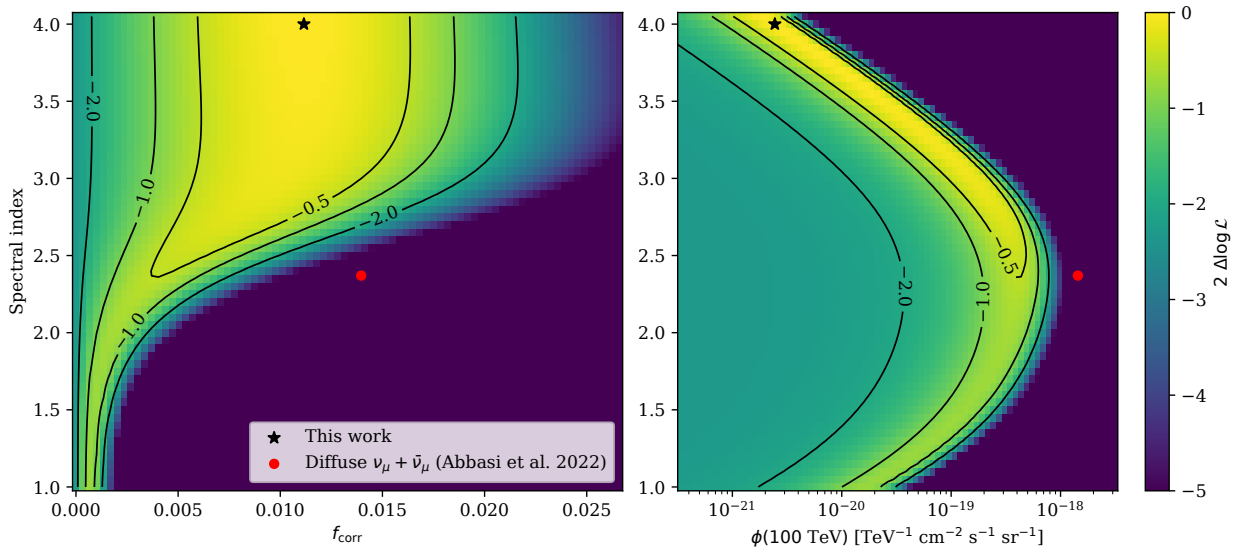

Figure 5.20: **Cross Correlation Likelihood Contours.** Left: For different pairs of astrophysical parameters $(f_{\mathrm{corr}}, \gamma)$, the value of the log-likelihood improvement is shown in contours and colors. Right: Equivalently, the likelihood can be parameterized in terms of the differential flux at 100 TeV.

	Null hypothesis	Test hypothesis
TS	-	2.307
P-value	-	0.23
χ^2	1082	1077
DoF	1120	1122
n_{corr}	-	4143
f_{corr}	-	0.0111
Spectral Index	-	$4.0^\dagger$
$f_{\mathrm{atm},1}$	1.101	1.089
$f_{\mathrm{atm},2}$	1.012	1.122
$f_{\mathrm{atm},3}$	0.893	0.891

Table 5.2: **Summary of Fit Parameters.** The best fit parameters found by the likelihood maximization procedure. The top row is the test hypothesis where some neutrinos are correlated with the large-scale structure. The bottom row is the null hypothesis where f_{corr} is fixed to zero. The dagger (†) indicates that the best fit parameter lies on the boundary of the allowed fit parameter space.

	Null hypothesis	Test hypothesis
TS	-	2.307
P-value	-	0.23
χ^2	1082	1077
DoF	1120	1122
n_{corr}	-	4143^{+2730}_{-4005}
f_{corr}	-	$0.011^{+0.007}_{-0.010}$
Spectral Index	-	$4.0^{\dagger}$
$f_{\text{atm},1}$	$1.101^{+0.030}_{-0.033}$	$1.089^{+0.030}_{-0.030}$
$f_{\text{atm},2}$	$1.012^{+0.072}_{-0.075}$	$1.122^{+0.075}_{-0.075}$
$f_{\text{atm},3}$	$0.893^{+0.414}_{-0.417}$	$0.891^{+0.411}_{-0.420}$

Table 5.3: **Upper Limits for Various Spectral Indices.** The neutrino differential flux upper limits derived from correlation strength are shown above for three spectral indices: 2.0, 2.37, and 3.0. The first column is the 90% confidence level upper limit on the correlation strength. The flux at 100 TeV and the flux at 100 TeV divided by the diffuse flux at 100 TeV are shown in the two right columns.

performing the cross-correlation to reduce the effect of the non-uniform effective area. The unWISE-2MASS galaxies are binned into a Healpix map as well, and the overdensity for each map is computed after masking the galactic plane and other bright infrared sources. I developed tools to create realistic data sets using both real events and Monte Carlo simulated events to simulate the background and signal events. These simulated events are used to evaluate the performance of the cross-correlation method before unblinding the results. The likelihood is formulated in terms of two astrophysical parameters: the correlation strength, and the neutrino spectral index. There is also an atmospheric correlation parameter for each energy bin. Monte Carlo simulations were used to create models for the astrophysical and atmospheric components of the cross-correlation likelihood. This likelihood were maximimzed and the log-likelihood difference relative to a no astrophysical component was evaluated as a test statistic. The test statistic was 2.307. The p-value was 0.23 which is not statistically significant. The test statistic was not significant and I placed upper limits on the strength of correlation assuming several spectral indices.

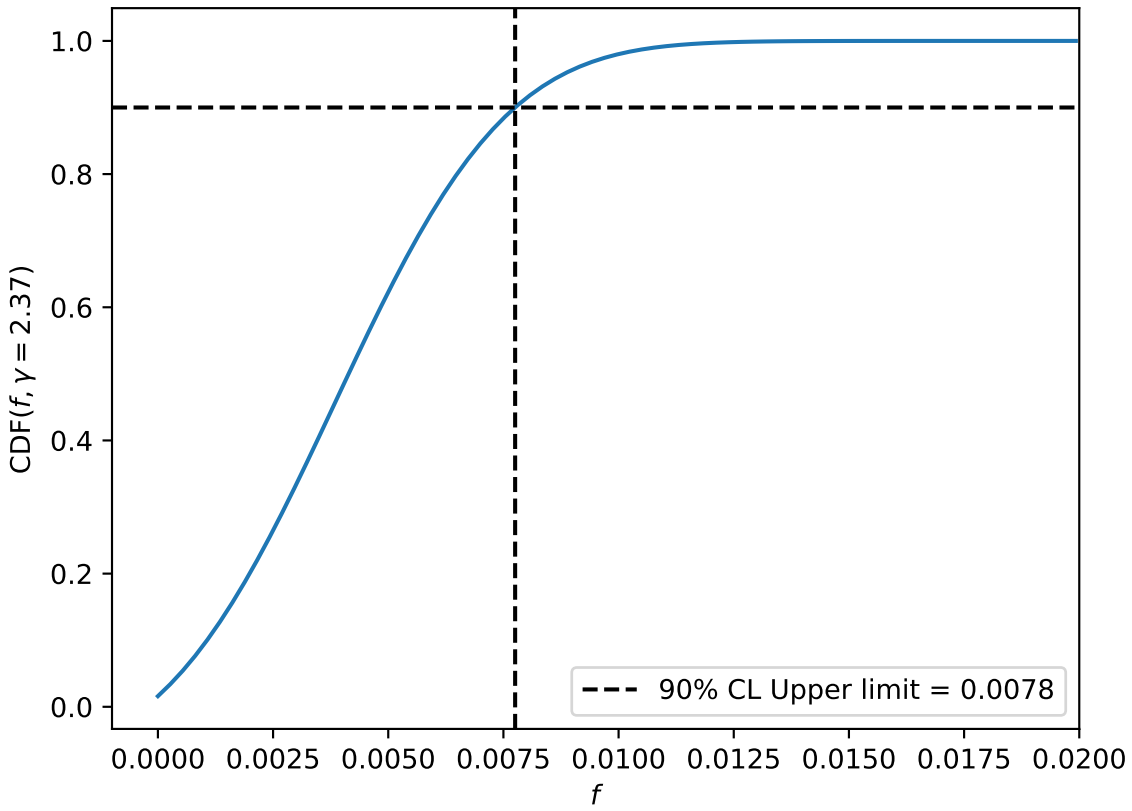

Figure 5.21: **Cross Correlation Likelihood CDF with $\gamma = 2.37$.** The cumulative distribution function for the likelihood is shown in blue. The upper limit is defined such that 90% of the likelihood lies below the value of f_{corr}.

6 ICECUBE CROSS-CORRELATION: INTERPRETATION

6.1 Introduction

The upper limit on the strength of the correlation between the IceCube neutrinos and unWISE-2MASS galaxies can be used to provide constraints on the neutrino flux coming from those galaxies and the distribution of neutrino sources over cosmic history. If the observed neutrinos represent a random sampling from the unWISE-2MASS galaxies and the bias parameters b_ν and b_g are equal, then the contribution of the correlated neutrino flux to the diffuse neutrino flux can be constrained. Additionally, the expected correlation strength can be calculated for various models of neutrino source populations as a function of redshift and compared with the correlation strength upper limit.

6.2 Correlated Neutrino Flux Constraint

The simplest interpretation of the cross correlation strength follows from the assumption that the neutrino counts are sampled from the the galaxy density. In reality, there is likely only a subset of galaxies that are neutrino emitters. If the neutrino-emitting galaxies are a fair sample of the full galaxy catalog and the large-scale structure, the correlation strength is unbiased.

When calculating an upper limit, the spectral index must be fixed. The most natural value is the observed spectral index of diffuse astrophysical muon neutrinos: $\gamma = 2.37$. Other values may also be used; see Chapter 5 for upper limits using other spectral indices. I use $\gamma = 2.0$ and $\gamma = 3.0$ as generic values that span a reasonable range that is consistent with diffuse astrophysical neutrino observations. The upper limits assume that the bias parameters are equal. The upper limits are shown in Figure 6.1 and summarized in Table 5.3. For $\gamma = 2.37$, less than 54% of the astrophysical diffuse flux at 100 TeV can be explained by sources that are correlated with the unWISE-2MASS catalog. For $\gamma = 2.0$ and $\gamma = 3.0$,

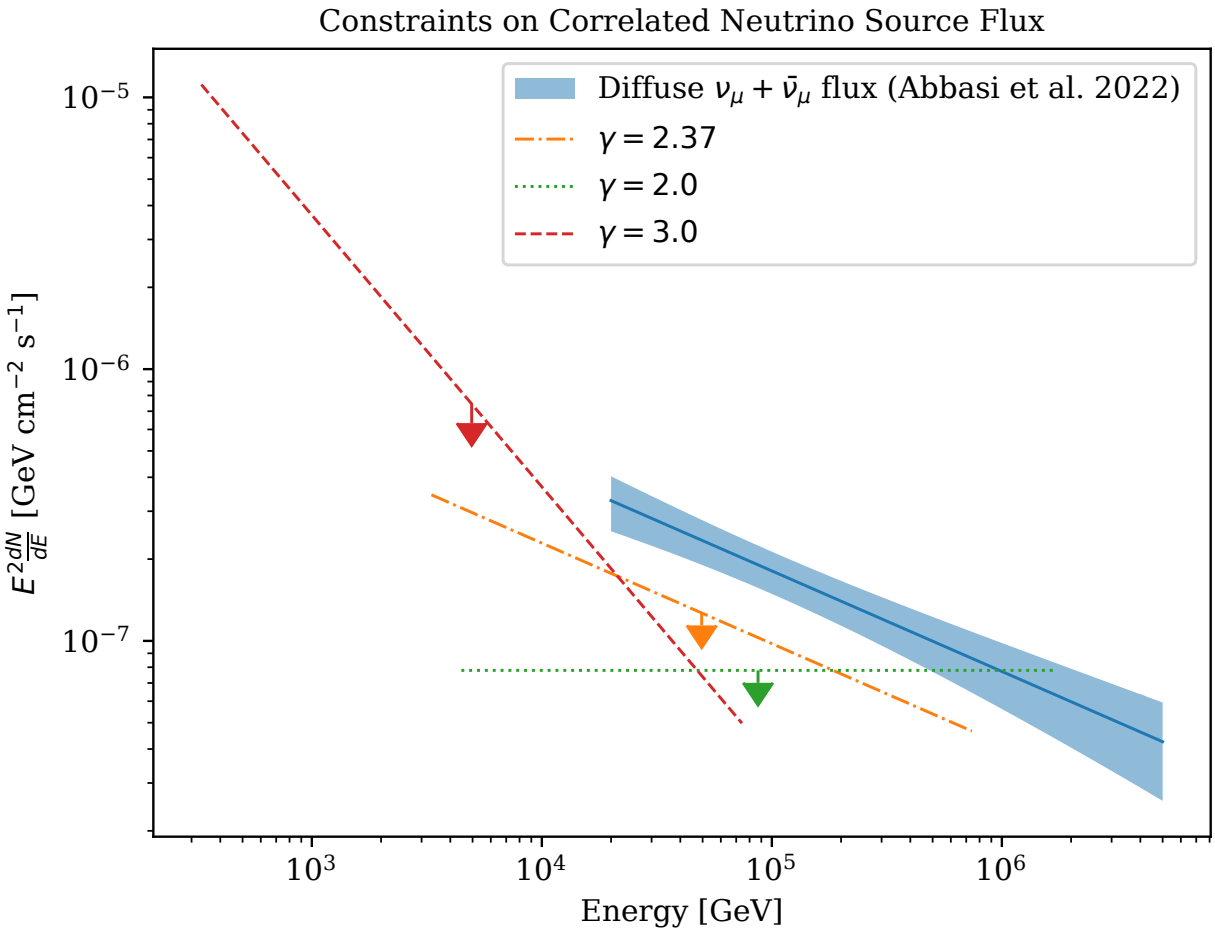

Figure 6.1: **Cross Correlation Upper Limits.** If the neutrinos are sampled from the unWISE-2MASS catalog, then the neutrino flux from those sources can be estimated assuming $\frac{b_\nu}{b_g} = 1$. The derived fluxes in the case of three different spectral indices are shown in the figure compared with the best fit diffuse flux of muon neutrinos. If the diffuse spectral index is assumed for the correlated neutrinos, the correlated flux is less than 54% of the total diffuse flux.

less than 43% and 20% of the flux at 100 TeV can be explained by correlated sources. All of these suggest that around half or more neutrinos come from outside the redshift probed by the unWISE-2MASS catalog, $0.05 < z < 0.22$.

6.3 Neutrino Source Population Modeling

In Section 6.2, we established upper limits on the astrophysical neutrino flux from sources correlated with the unWISE-2MASS catalog. A more careful analysis can constrain the distribution of neutrino sources with respect to redshift. We assume that the sources of astrophysical neutrinos form in overdensities in the underlying matter density field but that the comoving density of these sources evolves with redshift. Because the matter density field evolves as a function of redshift, the clustering between neutrino sources and the unWISE-2MASS galaxies will increase or decrease depending on how many neutrino sources are located in the same redshift range as the galaxies. In this paradigm, we can test parameterized models of the comoving density evolution,

$$\rho(z) \equiv \frac{1}{N_s}\frac{dN_s}{dV} \tag{6.1}$$

where the comoving density is measured in the rest frame at redshift z. We use standard tools from cosmology to predict the expected angular cross-power spectrum and compare this with the upper limit obtained in Chapter 5. The IceCube data set is the observed counts (or equivalently flux) rather than individual sources, so the model source distribution must be converted into a distribution of counts with respect to redshift $\lambda_\nu(z)$. This modeling process will involve several steps:

1. Write down expression for $\rho(z)$.
2. Obtain an expression for $\lambda_s(z) \equiv \frac{1}{N_s}\frac{dN_s}{d\chi(z)}$, the probability of a source occupying redshift between z and $z + dz$.

3. Use $\lambda_s(z)$ to obtain the distribution of counts $\lambda_\nu(z) \equiv \frac{1}{N_\nu}\frac{dN_\nu}{d\chi(z)}$ by re-weighting $\lambda_s(z)$.

4. Use $\lambda_\nu(z)$ and $\lambda_g(z)$ to obtain $C_\ell^{g\nu,\,\mathrm{corr}}$ and C_ℓ^{gg} using Equations 3.28 and 3.31.

5. Use $C_\ell^{g\nu,\,\mathrm{corr}}$ and C_ℓ^{gg} to obtain f_{corr} using Equation 6.7.

These steps will be described in detail below.

(1): Several classes of neutrino source distributions will be considered in step 1. These include:

1. Power law: $\frac{dN_s}{dV} \propto (1+z)^k$

2. Power law with cutoff: $\frac{dN_s}{dV} \propto (1+z)^k\, e^{-z/\xi}$

3. Sources tracing unWISE-2MASS : $\frac{dN_s}{dV} \propto \frac{dN_g}{dV}$

4. Counts tracing unWISE-2MASS : $\frac{dN_\nu}{dV} \propto \frac{dN_g}{dV}$

5. Sources tracing SFR: $\frac{dN_s}{dV} \propto \mathrm{SFR}(z)$

6. Constant co-moving density: $\frac{dN_s}{dV} \propto$ constant

The power law model is a generic model that can be used to compare with predictions from various measurements and models. For example, Stein et al. (2021) predict that tidal disruption events will follow a very negative evolution with $k < -3$. The cosmic ray source emissivity has been measured by Batista et al. (2019) to have $k = -1.6$. Comparing the neutrino power law constraint may illustrate the relationship between astrophysical neutrinos and other high-energy populations.

We also explore several non-parametric models. These models contain no free parameters; however, there is a degeneracy with the bias parameters that cannot be broken. For these models, we assume $b_\nu = b_g$ unless otherwise noted. The first two assume $\lambda_s \propto \lambda_g$ and $\lambda_\nu \propto \lambda_g$. These models explore the possibility that the neutrino sources or neutrino counts are directly traced by the unWISE-2MASS catalog. The star-formation rate is often considered as a likely template for high energy neutrino production because star-formation is

often related to AGN activity and it is thought that astrophysical neutrinos are produced by AGN. The final model tests whether the observed upper limit is consistent with a constant comoving neutrino source density.

(2) and (3): Neutrino source ensembles are simulated using the FIRst Extragalactic Simulation Of Neutrinos and Gamma-rays (FIRESONG) (Tung et al., 2021). FIRESONG is a Python code designed to simulate realistic neutrino source distributions, fluxes of individual neutrino sources as seen at Earth by IceCube, and cumulative diffuse neutrino flux observed by IceCube. The code includes the effects of intrinsic luminosity functions, power law spectra, the "K-correction," and the luminosity distance. Although the code supports distributions of source luminosity, we use a standard candle luminosity. At larger distances, the cosmological redshift can cause neutrinos to redshift into or out of the IceCube sensitive energy range. FIRESONG adjusts the observed flux by the K-correction to accurately describe the flux observed at Earth by IceCube. The luminosity distance is the effective distance by which the luminosity is scaled to describe the flux at Earth,

$$F = \frac{L}{4\pi D_L^2}. \tag{6.2}$$

The luminosity distance must be used because it accounts for the evolution of the universe that occurs while neutrinos propagate at nearly the speed of light. The luminosity distance is

$$D_L(z) = (1+z)\,\chi(z). \tag{6.3}$$

The distribution of neutrino counts with respect to redshift to the neutrino sources with respect to redshift is

$$\frac{dN_\nu}{dz} \propto \frac{1}{D_L(z)^2\,(1+z)^\gamma}\frac{dN_s}{dz} \tag{6.4}$$

where s denotes the sources and assuming the neutrino spectral energy distribution is E^γ. Source distributions are constructed using FIRESONG which appropriately samples the sources as a function of redshift. The sampled sources are aggregated into a histogram and

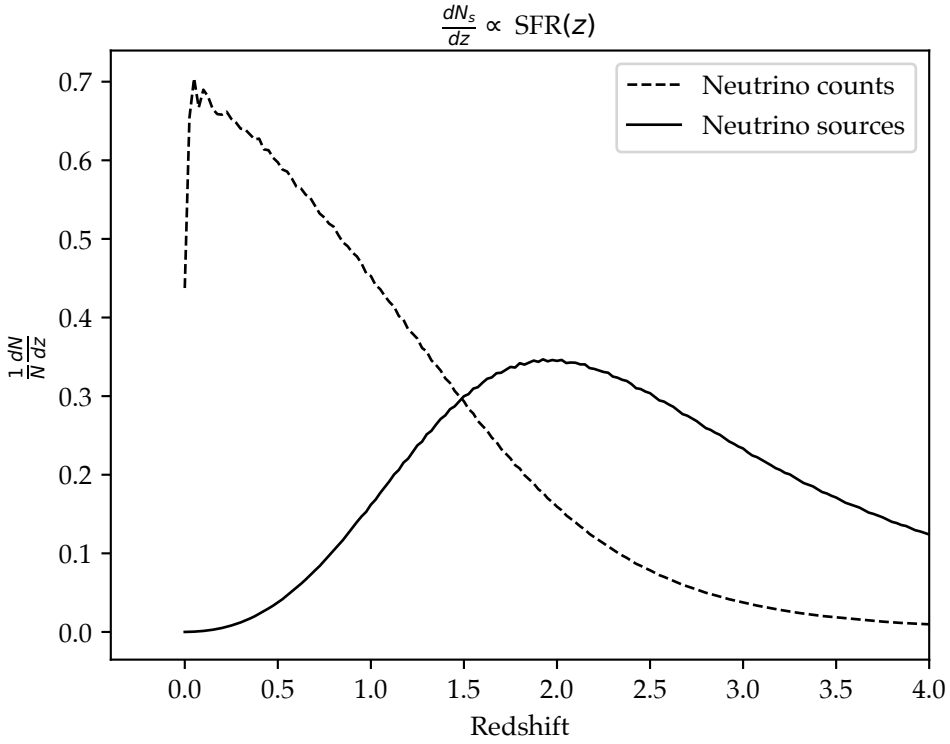

Figure 6.2: **SFR Source and Counts Distribution.** The intrinsic neutrino source distribution with respect to redshift is different from the distribution of counts observed by IceCube. This figure shows an example of this. The intrinsic source distribution (solid line) is proportional to the star formation rate. This distribution is weighted by D_L^2 to arrive at the observed distribution of counts (dashed line).

normalized over redshift to show the evolution of $\frac{dN_s}{dz}$. An example of the flux weighting is shown in Figure 6.2. For a source distribution that peaks at $z \approx 2$, the most nearby sources dominate the sample of neutrino counts.

(4): The strength of the cross-correlation signal depends on the distribution of both catalogs with respect to redshift. The cross-correlation strength depends on the line-of-sight integral of the underlying matter power spectrum,

$$C_\ell^{g\nu} = b_g\, b_\nu \int d\chi\, \chi^{-2}\, \frac{1}{N_g}\frac{dN_g}{dz(\chi)}\, \frac{1}{N_\nu}\frac{dN_\nu}{dz(\chi)} P\left(k = \frac{\ell + \frac{1}{2}}{\chi}\right) \tag{6.5}$$

where N_g is the number of sources in the galaxy catalog, N_ν is the number of neutrinos observed by IceCube, χ is the comoving distance, and $P(k)$ is the matter density power

spectrum. Similarly, the autocorrelation can be written as

$$C_\ell^{gg} = b_g^2 \int d\chi \, \chi^{-2} \left(\frac{1}{N_g} \frac{dN_g}{dz(\chi)} \right)^2 P\left(k = \frac{\ell + \frac{1}{2}}{\chi} \right) \tag{6.6}$$

Equation 3.16 can be solved numerically. The numerical integration is performed by CCL. CCL calculates the matter-matter power spectrum, $P(k)$, by solving the Boltzmann equation in Fourier space. The cosmology used in the calculation is fixed to standard ΛCDM.

(5): The equations in Section 5.5 can be rearranged to arrive at

$$f_{\text{corr}} \equiv \frac{b_\nu}{b_g} \frac{n_{\text{corr}}}{n_{\text{total}}} \approx f_{\text{astro}} \left\langle \frac{C_\ell^{g\nu}}{C_\ell^{gg}} \right\rangle. \tag{6.7}$$

The ratio defined in Equation 6.7 is averaged over multipoles to obtain a single number corresponding to the correlation strength f_{corr}. The fraction of astrophysical events can be calculated from the best fit value of diffuse astrophysical muon neutrinos. The value is $f_{\text{astro}} = 0.013$. Inspection of equations 6.5 and 6.6 shows the equality on the left is exactly when $\lambda_g = \lambda_\nu$. This remains approximately true as long as the redshift range of the galaxy catalog is not too large. We have verified numerically that the ratio of the cross-power spectrum and galaxy autocorrelation vary only by a few percent dependent on multipole ℓ. The factor f_{astro} here represents the astrophysical sample purity for all neutrinos seen by IceCube.

6.4 Power Law Source Distribution

We calculated the expected cross-correlation for a grid of power law from -3 to 3 in steps of 0.1. The expected correlation strength for each value of the power law index can be compared with the observed upper limit. The constraints on the neutrino source population assuming a power law evolution are shown in Figure 6.4. The solid line represents the

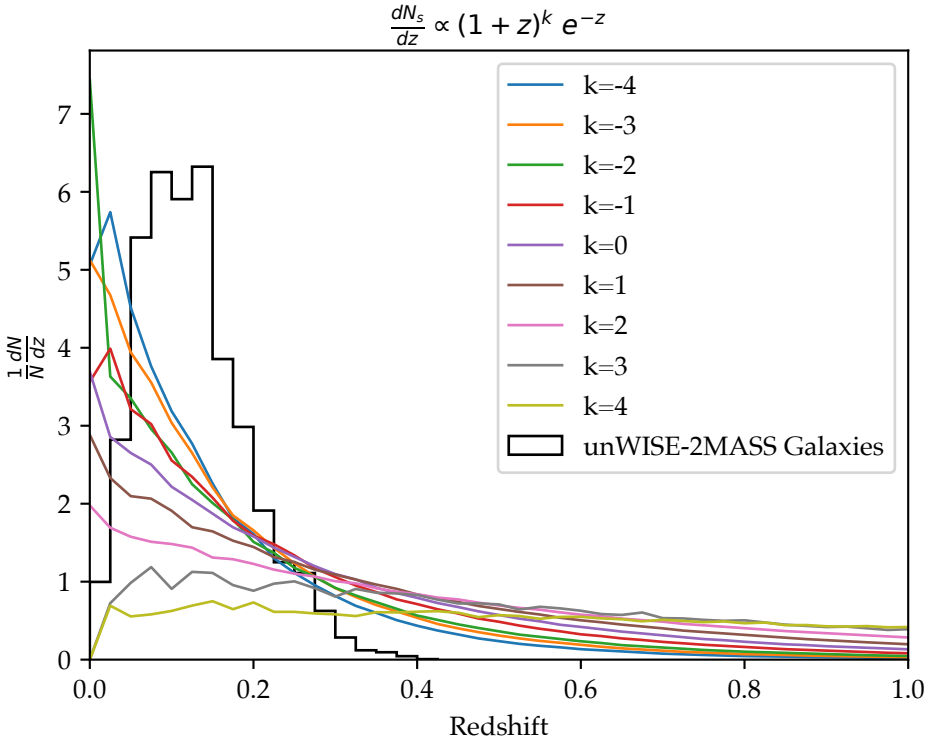

Figure 6.3: **Power Law Counts Distributions.** If the neutrino sources follow a distribution of the form $\frac{dN_s}{dz} \propto (1+z)^k\, e^{-z}$, the luminosity distance squared weighted distributions appear as above. The noise in these curves arises from the finite sample size obtained in FIRESONG. The unWISE-2MASS source distribution is shown as a black histogram. The correlation signal will be maximized when the product of those curves is large.

correlation strength predicted by the model assuming equal bias parameters, and the dashed line is a pessimistic case where $b_\nu = 2\, b_g$. The horizontal dash-dot line is the observed upper limit on the correlation strength. Below the dash-dot line, the observed correlation is compatible with the model; above it, the model predicts a stronger correlation than is consistent with the observation. Assuming equal bias parameters, we find $k < -1.75$ are disfavored.

I performed a similar test varying both the source distribution power law spectral index and exponential cutoff over the same grid of power law indices and an exponential cutoff grid between -3 and -0.1 in steps of 0.1 Examples of these distributions are shown in Figure 6.3. The jointly allowed parameter space of k and ξ is shown in Figure 6.5. The region

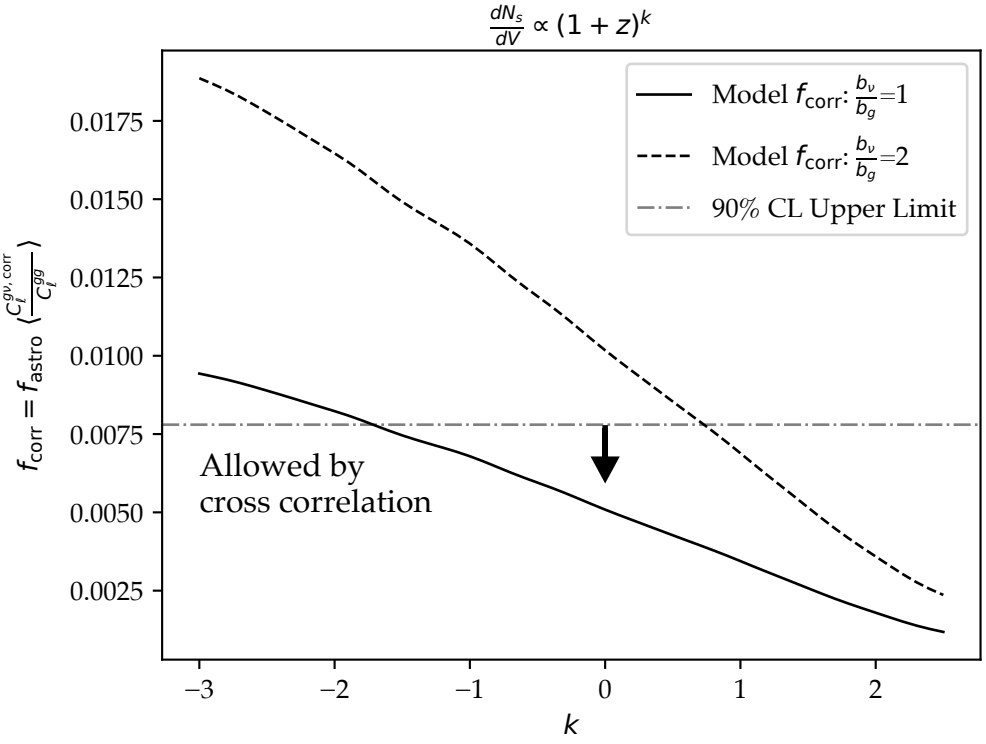

Figure 6.4: **Neutrino Source Distribution Constraints.** If the neutrino sources follow a distribution of the form $\frac{dN_s}{dz} \propto (1+z)^k$, the expected correlation strength, $f_{\rm corr}$, can be calculated given the ratio of diffuse astrophysical neutrinos to total neutrinos, $f_{\rm astro}$. The expected correlation strength for equal bias parameters (solid black) and $\frac{b_\nu}{b_g} = 2$ (dashed line) are shown. The actual upper limit is shown by the gray solid line. The area below the line is allowed by the upper limit.

in the bottom right section of the figure is the allowed values of the exponentially cutoff power-law source distribution. Below $\xi = -1$, the allowed values of k are not strongly affected. Source distributions with $\xi > -0.5$ have a higher concentration of nearby sources, so the correlation strength is inconsistent with the observed correlation upper limit.

6.5 unWISE-2MASS Tracing

The astrophysical neutrino counts or sources may be modeled as a random sampling of the nearby large-scale structure. Although the unWISE-2MASS is not volume limited, it still serves as a useful probe of the nearby large-scale structure. I test two models: (1)

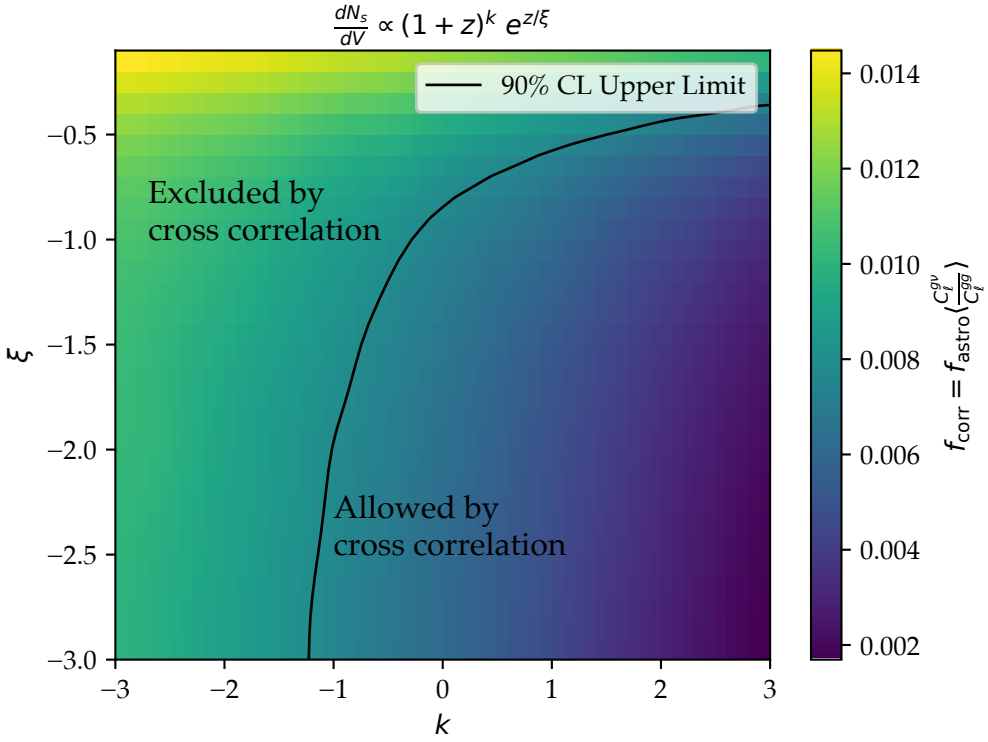

Figure 6.5: **Two Dimensional Neutrino Source Distribution Constraints.** If the neutrino sources follow a distribution of the form $\frac{dN_s}{dz} \propto (1+z)^k\, e^{z/\xi}$, then the expected correlation strength, $f_{\rm corr}$, can be calculated given the ratio of diffuse astrophysical neutrinos to total neutrinos, $f_{\rm astro}$. The white line separates the parameter space that is allowed by the observed upper limit; the region in the lower right corner is allowed. It is assumed that $\frac{b_\nu}{b_g} = 1$.

the neutrino counts are a sampling of the unWISE-2MASS galaxies, ie. $\frac{dN_\nu}{dz} = \frac{dN_g}{dz}$ and (2) the neutrino sources are a sampling of unWISE-2MASS galaxies, ie. $\frac{dN_s}{dz} = \frac{dN_g}{dz}$. The latter is a more physically realistic model; however, the unWISE-2MASS galaxies span a narrow enough redshift range that the difference is small. The first corresponds to the correlated flux measurement from Section 6.2. The expected $f_{\rm corr}$ for these models was obtained by integrating Equation 6.5 using CCL and assuming $\frac{dN_\nu}{dz} = \frac{dN_g}{dz}$ for the first and $\frac{dN_\nu}{dz} = \frac{1}{D_L(z)(1+z)^\gamma}\frac{dN_g}{dz}$ for the second. The model predictions for these two models are $f_{\rm corr} = 0.0160$ and $f_{\rm corr} = 0.0144$. These are approximately twice and 1.8 times the obtained upper limit respectively. If the majority of the astrophysical flux were produced in the redshift range probed by the unWISE-2MASS galaxies, clustering would be detected in

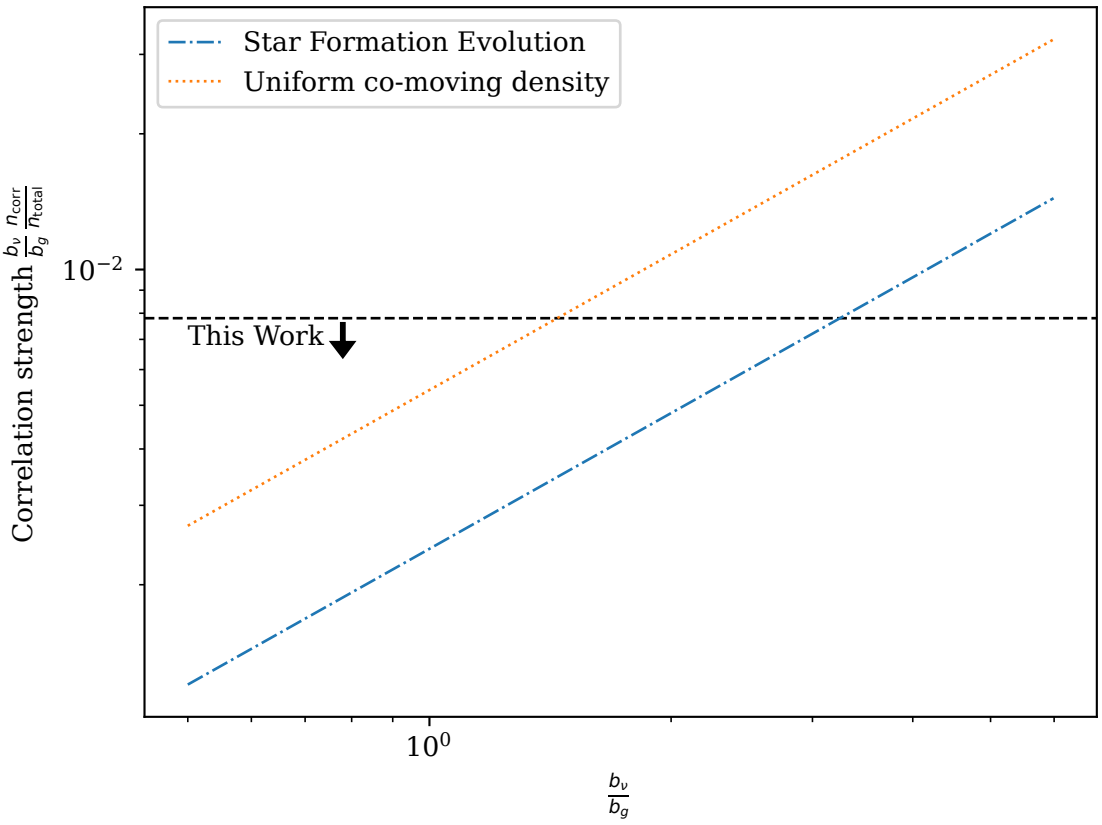

Figure 6.6: **Constraints of SFR and No Evolution Populations.** The expected correlation strength as a function of bias parameters can be compared to the observed upper limit. The most likely case is $b_\nu \approx b_g$. Both the SFR evolution and no evolution models are compatible with this case; however, the no evolution scenario is not allowed for $\frac{b_\nu}{b_g} > 2$.

this analysis.

6.6 No Evolution

Although it is not a likely astrophysical case, it is useful to check whether the observed neutrino sources are consistent with a source evolution that does not evolve, ie. $\frac{dN_s}{dz} =$ constant. This case is already shown in Figure 6.5. It corresponds to $k = 0$ and $\xi \gg 1$. This scenario is excluded by the upper limit in the plot. I also directly computed the expected cross-correlation strength for a source population with no evolution. This is shown in Figure 6.6. The no evolution case is allowed for $b_\nu = b_g$, but not for $b_\nu = 2b_g$

Model	$f_{\text{corr,model}}$	$\frac{f_{\text{corr,model}}}{f_{\text{corr,UL}}}$
Sources tracing unWISE-2MASS	0.016	2.051
Counts tracing unWISE-2MASS	0.014	1.846
Star formation rate	0.002	0.269
Constant comoving density	0.005	0.667

Table 6.1: **Correlation Strength for Non-Parametric Models.** We disfavor models where all the sources have the same distribution with respect to redshift as the unWISE-2MASS catalog or the neutrino counts themselves follow the unWISE-2MASS . We cannot rule out models where neutrino sources follow the star formation rate, or where the neutrino sources have a uniform comoving density unless the neutrino sources have a large bias parameter.

6.7 Star Formation Rate Evolution

The universe has undergone an evolution of the star formation rate (SFR). The cosmic star formation rate peaked at a redshift around two and has been declining since. At nearby redshift, the star formation rate follows a power law approximately following $(1+z)^{3.4}$. Star formation is an interesting neutrino source tracer because high energy neutrinos may be contributed by clusters of young massive stars (Ackermann et al., 2011) or because star formation is also a tracer of active galactic nucleus activity. AGN are also candidate neutrino sources. An evolution following the SFR is difficult to constrain with the observed correlation strength because the majority of the sources lie at large redshift which is outside of the unWISE-2MASS galaxy catalog redshift range. The correlation strength that is allowed by the correlation strength upper limits is shown in Figure 6.6 in terms of the bias parameters. The correlation is compatible with an SFR source evolution for physically reasonable values of the clustering bias parameters. The correlation strengths for the non-parametric models are shown in Table 6.1

6.8 Summary

Constraints have been presented on the fraction of the diffuse astrophysical neutrino flux which is correlated with the unWISE-2MASS galaxies. The exact value depends on the

spectral index. If the diffuse muon neutrino spectral index is assumed, then the correlated flux must be less than 54% of the diffuse measurement. This suggests that around half of the neutrino flux comes from redshift greater than that spanned by the unWISE-2MASS galaxies.

I also presented constraints on the neutrino source distribution with respect to redshift. Numerical models were created using FIRESONG and the Core Cosmology Library for exponentially cutoff power laws, no evolution, and star formation rate distributions. The exponentially cutoff power-law models favor neutrino source candidates with a power law index greater than -1.75. This disfavors more nearby neutrino source candidates such as tidal disruption events. The no-evolution model is allowed except in the case of unusually high neutrino clustering bias. The star formation rate model is allowed for any physically reasonable value of b_ν.

7 OUTLOOK

In this work, the relationship between the diffuse astrophysical neutrino flux and the large-scale structure was explored. Neutrino sources likely form within overdense regions, so tracers of large-scale structure should be correlated with the diffuse neutrino flux. The two-point angular cross-correlation revealed no statistically significant relationship between these neutrinos and a catalog of galaxies tracing the nearby large-scale structure. This suggests that a significant fraction of neutrino sources lie beyond the redshift range spanned by this catalog or that the sources are not related to the large-scale structure.

The sensitivity of a cross-correlation analysis is mainly limited by two factors.

1. Background atmospheric muons: The atmospheric muon background smothers the expected clustering signal. One way to remove this background is to use a selection of events where the neutrino interaction occurs within the detector volume. Unfortunately, this removes almost all the signal events as well. A starting tracks data set has been produced, but contains only a few hundred events.

2. Angular resolution: The angular resolution attenuates the cross power spectrum exponentially with ℓ, $B_\ell = e^{\frac{\ell\theta_p}{16\sqrt{\pi}}}$. A neutrino detector with a larger detection volume provides a longer lever arm for constraining the track origin and improving sensitivity at large ℓ.

IceCube-Gen2 is a planned neutrino telescope that will expand the capabilities of the current IceCube observatory (Clark et al., 2021). This upgrade will improve the angular uncertainty and number of neutrino events by using a larger volume of ice. The sensitivity to the correlation signal can be estimated using analytical estimates for the uncertainty of the cross-power spectra. I neglect the contribution to the power spectra from atmospheric neutrinos and ignore mode-coupling for simplicity.

The expected uncertainty for the observed angular autocorrelation and cross-correlation can be written as

$$\frac{\delta C_\ell^{gg,\text{obs}}}{C_\ell^{gg}} = \sqrt{\frac{2\left(1+\frac{C_{\text{noise}}^{gg}}{C^{gg}B_\ell^{g\,2}}\right)^2}{(2\ell+1)f_{\text{sky}}}} \tag{7.1}$$

and

$$\frac{\delta C_\ell^{g\nu,\text{obs}}}{C_\ell^{g\nu}} = \sqrt{\frac{2\left(1+\frac{C_{\text{noise}}^{gg}}{C^{gg}B_\ell^{g\,2}}\right)\left(1+\frac{C_{\text{noise}}^{\nu\nu}}{C^{\nu\nu}B_\ell^{\nu\,2}}\right)}{(2\ell+1)f_{\text{sky}}}}. \tag{7.2}$$

The noise spectra for a sample containing signal and uncorrelated background events are defined as $C_{\text{noise}} = 4\pi f_{\text{sky}}\left(\frac{n_{\text{signal}}}{n_{\text{background}}}+\frac{1}{n_{\text{signal}}}\right)$. Note that the noise spectrum does not depend on ℓ. The neutrino and galaxy autocorrelation spectra are calculated assuming the unWISE-2MASS redshift distribution for the galaxies and a star formation rate evolution for the neutrinos. The autocorrelation spectra are scaled by a bias equal to 1.23 which is the result found for the unWISE-2MASS catalog, and the neutrino autocorrelation is further scaled by $f_{\text{astro}} = 0.013$ which is the astrophysical purity of the northern tracks sample based on the diffuse measurement (IceCube Collaboration et al., 2022b). The resulting fraction uncertainties on the power spectra are shown in Figure 7.1 for a northern tracks-like sample with current 10 years of IceCube data, 3 years of IceCube Gen2, and 10 years of IceCube Gen2.

The projected uncertainty on the measured correlation strength can be estimated using the Fisher information. The Fisher information is defined as $\mathcal{F} = \frac{\partial^2 \log(\mathcal{L})}{\partial f_{\text{corr}}^2}$ and the expected uncertainty on a parameter is $\sigma_{f_{\text{corr}}} = \frac{1}{\sqrt{\mathcal{F}}}$ If the likelihood is Gaussian and I neglect mode coupling,

$$\mathcal{L} = \prod_\ell \frac{1}{\sqrt{2\pi\sigma_\ell^2}} e^{-\left(\frac{C_\ell^{g\nu}-f_{\text{corr}}C_\ell^{gg}}{\sqrt{2}\sigma}\right)^2}, \tag{7.3}$$

the Fisher information is $\mathcal{F} = -\sum_\ell \frac{C_\ell^{gg\,2}}{\sigma_\ell^2}$. The expected uncertainty on the correlation strength for the current IceCube detector is $\sigma_{f_{\text{corr}}} = 0.015$ which is similar to our 90% confidence level upper limit. After 10 years with IceCube Gen2, $\sigma_{f_{\text{corr}}} = 0.005$. IceCube

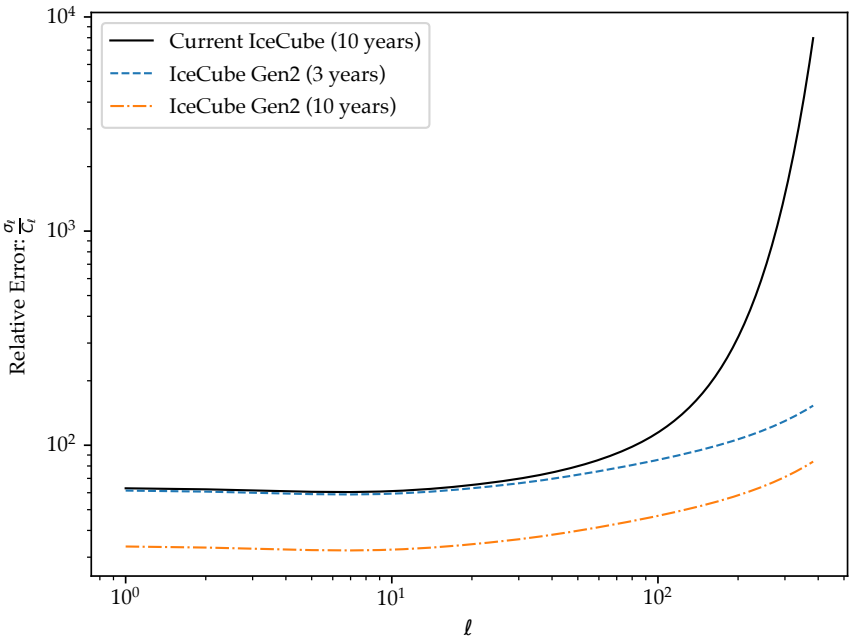

Figure 7.1: **Projected Cross Power Spectra Relative Uncertainty.** The projected cross-power spectra for different iterations of the IceCube detector are shown above.

Gen2 will be able to make a clustering measurment that is three times more precise than our current estimate. This is in the range of the star formation rate ($f_{\text{corr}} = 0.003$) and uniform ($f_{\text{corr}} = 0.005$) neutrino source population evolutions. Measurements of clustering may be within reach of IceCube Gen2.

The statistical analysis used in Chapter 5 follows the standard procedure for frequentist hypothesis testing. There are six steps in frequentist hypothesis testing.

1. Define the test and null hypotheses.
2. Define a test statistic.
3. Derive the distribution of the test statistic under the null hypothesis.
4. Select the significance level that defines the maximum acceptable false positive rate.
5. Calculate the observed test statistic from the observed data.
6. Compare the observed test statistic to the test statistic distribution under the null hypothesis. If the probability of observing a TS under the null hypothesis is less than the desired false positive rate, reject the null hypothesis.

The application of these steps to the cross-correlation analysis is outlined in this section.

Define Hypotheses

The goal of this cross correlation analysis is to determine whether there is any statistically significant clustering between IceCube neutrinos and the large scale structure. The strength of that correlation has been parameterized as f_{corr} in Equation 5.11. A natural test hypothesis is that $f_{\text{corr}} > 0$ and the complementary null hypothesis is that $f_{\text{corr}} = 0$. The spectral index of correlated neutrinos γ is left as a free parameter in the test hypothesis but is restricted to a range consistent with diffuse astrophysical neutrino flux measurements, $1 \leq \gamma \leq 4$. The remaining parameters are nuisance parameters.

The definition of the test hypothesis excludes $f_{\text{corr}} < 0$. It is theoretically possible to measure a negative correlation. An anti-correlation would suggest that neutrinos preferentially arrive from directions that correspond to voids in the large-scale structure. This

would likely require some beyond-standard-model physics to explain. Given that there have been neutrinos observed from AGN, and that AGN are correlated with the large-scale structure, the anti-correlation hypothesis is excluded.

Define a Test Statistic

A test statistic is simply a single real number derived from a set of data. The choice of test statistic is an important consideration for the implementation of a statistical test. A common choice of test statistic is the log of the likelihood ratio,

$$\mathrm{TS} = 2\log\left(\frac{\mathcal{L}(\mathrm{data}|\mathrm{test})}{\mathcal{L}(\mathrm{data}|\mathrm{null})}\right). \tag{A.1}$$

The test hypothesis defined above allows a range of parameters, but only one hypothesis should be tested to avoid false positives due to the look elsewhere effect. The set of parameters which maximizes the likelihood also maximizes the test statistic, so the maximum likelihood will have the highest chance of a significant detection. The test statistic used in Chapter 5 is

$$\mathrm{TS} = 2\log\left(\frac{\mathcal{L}(\{C_{\ell i}^{g\nu}\}|\hat{f}_{\mathrm{corr}}, \hat{\gamma}, \hat{\hat{f}}_{\mathrm{atm},1}, \hat{\hat{f}}_{\mathrm{atm},2}, \hat{\hat{f}}_{\mathrm{atm},3})}{\mathcal{L}(\{C_{\ell i}^{g\nu}\}|0, 0, \hat{f}_{\mathrm{atm},1}, \hat{f}_{\mathrm{atm},2}, \hat{f}_{\mathrm{atm},3})}\right). \tag{A.2}$$

The hats indicate that the parameter is the value that maximizes the likelihood. The particular form of the likelihood depends on the data under study, but it is often the case that the data follow a multivariate normal distribution. The optimization of the atmospheric parameters is performed independently for the test and null hypotheses.

Test Statistic Distribution under the Null Hypothesis

The next step is to derive the test statistic distribution under the null hypothesis,

$$P(\mathrm{TS}|\mathrm{null}) = P(\mathrm{TS}|0, 0, \hat{f}_{\mathrm{atm},1}, \hat{f}_{\mathrm{atm},2}, \hat{f}_{\mathrm{atm},3}). \tag{A.3}$$

There is an analytic result for the distribution of the log-likelihood ratio derived by Wilks (Wilks, 1938). Wilks' theorem states that the log-likelihood ratio will be distributed following a χ^2 distribution with degrees of freedom equal to the difference in degrees of freedom in the test and null hypotheses. In this case, there are two additional fit parameters in the test hypothesis. Wilks' theorem only applies when the test and null hypotheses are nested. Hypotheses are considered nested when the null hypothesis is contained within the maximization space and doesn't lie on the boundary. The hypotheses we have defined fail the boundary criterion because the fit parameter space is constrained to have $f_{\text{corr}} \geq 0$ and the null hypothesis has $f_{\text{corr}} = 0$. This problem has been treated before in the γ-ray astrophysics community when searching for new point sources. Mattox et al. (1996) found that the test statistic ratio is distributed like

$$P(\text{TS}|\text{null}) = \begin{cases} \frac{1}{2} & \text{TS} = 0 \\ \frac{1}{2}\chi^2_{df=2}(\text{TS}) & \text{TS} > 0 \end{cases} \tag{A.4}$$

where $\chi^2_{df=2}(\text{TS})$ refers to the χ^2 probability density with two degrees of freedom. Intuitively, this can be understood by thinking about what happens to realizations of the data set that has likelihoods maximized by values of $\hat{f}_{\text{corr}}$ slightly greater or lesser than zero. If $\hat{f}_{\text{corr}}$ is slightly above zero, this is simply the normal case and the test statistics for those realizations follow the analytical distribution. If $\hat{f}_{\text{corr}} < 0$, then the optimization is limited to $\hat{f}_{\text{corr}} = 0$. In this case, Equation A.2 is equal to zero. Under the null hypothesis, $\hat{f}_{\text{corr}}$ has an expected value equal to zero and has a distribution that is symmetric around zero, so half of the realizations will have $\text{TS} = 0$.

In practice, the test statistic distribution should be numerically validated by using simulated data sets. To evaluate the null test statistic distribution, atmospheric-only data sets were generated, and the test statistic was calculated for each set. The resulting test statistic distribution is shown in Figure 5.16. The blue dashed line in that figure is a χ^2 distribution with two degrees of freedom, but neglecting the factor of one half. The

numerical results are shown in orange. As expected, half of the trials have TS $= 0$. The slope of the test statistic distribution is different than the expected slope from Wilks' theorem. This is possibly due to the additional free parameter introduced by the spectral index γ that has some covariance with f_{corr}.

Select an Acceptable False Positive Rate

The acceptable false positive rate is a matter of convention. In particle physics and astrophysics, it is conventional to claim a discovery if the statistical significance is a 5σ or greater fluctuation above the background expectation. The false positive alarm probability is called a p-value,

$$\begin{aligned} p &= \int_{\text{TS}}^{\infty} P(\text{TS}|\text{null})\, d\text{TS} \\ &= 1 - \int_{0}^{\text{TS}} P(\text{TS}|\text{null})\, d\text{TS} \\ &= 1 - \text{CDF}(\text{TS}|\text{null}) \end{aligned} \tag{A.5}$$

where CDF(TS|null) is the cumulative distribution function of the test statistic under the null hypothesis. The value of $1 - \text{CDF}(\text{TS}|\text{null})$ for the cross-correlation analysis may be read directly off the ordinate of Figure 5.16.

To translate this into the language of particle physics, the observed p-value can be converted into a multiple of the standard deviation if that p-value were observed for a process following a Gaussian distribution with zero mean and unit variance. The p-value for a Gaussian distribution is defined as

$$\begin{aligned} p &= 1 - \text{CDF}(x) \\ &= \frac{1}{2}\left(1 - \text{erf}\left(\frac{x}{\sqrt{2}}\right)\right). \end{aligned} \tag{A.6}$$

This can be inverted to

$$x = \sqrt{2}\,\text{erf}^{-1}(1 - 2p) \tag{A.7}$$

where x is the number of standard deviations away from zero. A 5σ result has a p-value equal to about 10^{-6} or one in a million.

Calculate the Observed Test Statistic

The test statistic is calculated from the log-likelihood ratio defined in Equation A.2. The maximization is performed separately for the test hypothesis and null hypothesis. The maximization problem can be written as

$$\nabla \mathcal{L} = 0 \tag{A.8}$$

where ∇ is the gradient operator. The likelihood itself is a multivariate Gaussian distribution. The likelihood is defined in Equation 5.14. The test hypothesis is minimized with respect to $f_{\text{corr}}, \gamma, f_{\text{atm},1}, f_{\text{atm},2}$, and $f_{\text{atm},3}$ and the null hypothesis is maximized with respect to $f_{\text{atm},1}, f_{\text{atm},2}$, and $f_{\text{atm},3}$ with $f_{\text{corr}} = 0$ and $\gamma = 2.5$ held fixed. In principle, a multivariate Gaussian can be maximized analytically; however, the presence of the spectral index prevents analytic maximization because the derivative $\frac{\partial \mathcal{L}}{\partial \gamma}$ does not have an analytic expression. Both of the maximization steps are done numerically using Python and Scipy.

Calculate the Observed P-Value

The observed p-value can be calculated from the observed test statistic,

$$p = 1 - \text{CDF}(\text{TS}). \tag{A.9}$$

This value is shown in the abscissa of Figure 5.16.

Custom software was developed to perform the cross-correlation used in this analysis. The software is called `nuXgal`. The software can be found on github [1]. The version of this code used in this analysis depends on an IceCube Collaboration internal tool called `csky` which is not publicly available.

B.1 Source

The source code for this package is primarily contained in the directory `KIPAC/nuXgal`. The primary constituents used in this analysis and their roles are as follows:

1. `CskyEventGenerator.py`: Generate simulated data sets for analysis performance testing purposes.

2. `DataSpec.py`: Create a custom neutrino data selection binned in energy from the default Northern Tracks selection within `csky`.

3. `Defaults.py`: Stores global variables that configure the analysis parameters such as energy binning and Healpix pixel size.

4. `GalaxySample.py`: Loads and handles galaxy sample data.

5. `Likelihood.py`: Constructs and evaluates the likelihood and test statistic given a neutrino sample and galaxy sample.

6. `Models.py`: Constructs and stores models for the cross-correlation under different assumptions. Various models are constructed in this module but only the one described in this thesis is used.

7. `NeutrinoSample.py`: Loads and stores a simulated or experimental neutrino data set.

[1] https://github.com/dguevel/nuXgal

B.2 Scripts

There are several scripts associated with this package that use the code described in Section app:source. The scripts that are used in this thesis and are in a mature, non-experimental state are described below.

1. `nuXgal-generate-data.py`: This script generates synthetic data samples for the purpose of testing the performance of the cross-correlation method. The script has options for the level of signal to inject and an input template option for different galaxy catalogs. The background may be RA-scrambled data or simulated data. The output file is a JSON containing the output cross-power spectra as well as some housekeeping data that is useful for further analysis. Multiple trials can be simulated using a single call to this script.

2. `nuXgal-fit-data.py`: This script takes a simulated data set from `nuXgal-generate-data.py` and fits a maximum likelihood model to it. The output is a JSON file containing model parameters and test statistics for each trial in the input file.

3. `nuXgal-unblind.py`: This script performs the unblinding process as approved by the IceCube Collaboration Neutrino Sources Working Group. The experimental data are cross-correlated with the unWISE-2MASS galaxies and fit to the method described in Chapter 5. The output is a JSON file containing the fit parameters and test statistic.

4. `firesong-class-model.py`: This script uses FIRESONG and CCL to calculate model predictions for the clustering parameter given an input neutrino source density evolution. The user inputs the evolution as an input parameter. The output is a simulated list of neutrino sources with their fluxes, the galaxy-neutrino cross-correlation, the galaxy-galaxy correlation, and their average ratio.

5. `compute-covariance.py`: This script calculates the covariance of the multipoles in the angular cross-correlation power spectrum. The input is a list of JSON files gener-

ated by `nuXgal-generate-data.py` containing only background and the output is a Numpy array file containing the covariance matrices for each energy bin.

REFERENCES

Abbasi, R., et al. 2013, Nuclear Instruments and Methods in Physics Research Section A: Accelerators, Spectrometers, Detectors and Associated Equipment, 703, 190, doi: 10.1016/j.nima.2012.11.081

Abell, G. O. 1958, The Astrophysical Journal Supplement Series, 3, 211, doi: 10.1086/190036

Abeysekara, A. U., et al. 2021, Nature Astronomy, 5, 465, doi: 10.1038/s41550-021-01318-y

Abu-Zayyad, T., et al. 2013, The Astrophysical Journal Letters, 768, L1, doi: 10.1088/2041-8205/768/1/L1

Ackermann, M., et al. 2011, Science, 334, 1103, doi: 10.1126/science.1210311

—. 2012, The Astrophysical Journal, 750, 3, doi: 10.1088/0004-637X/750/1/3

Aghanim, N., et al. 2020, Astronomy & Astrophysics, 641, A8, doi: 10.1051/0004-6361/201833886

Ahrens, J., et al. 2004, Nuclear Instruments and Methods in Physics Research Section A: Accelerators, Spectrometers, Detectors and Associated Equipment, 524, 169, doi: 10.1016/j.nima.2004.01.065

Albert, A., et al. 2024, The Astrophysical Journal Letters, 973, L34, doi: 10.3847/2041-8213/ad772e

Alekseev, V. V., et al. 2017, Physics of Particles and Nuclei, 48, 687, doi: 10.1134/S1063779617050033

Alves Batista, R., et al. 2019, Frontiers in Astronomy and Space Sciences, 6, doi: 10.3389/fspas.2019.00023

Amenomori, M., et al. 2011, Advances in Space Research, 47, 629, doi: 10.1016/j.asr.2010.08.029

Arnett, W. D., Bahcall, J. N., Kirshner, R. P., & Woosley, S. E. 1989, Annual Review of Astronomy and Astrophysics, 27, 629, doi: 10.1146/annurev.aa.27.090189.003213

Astiasarain, X., et al. 2023, Astronomy & Astrophysics, 671, A47, doi: 10.1051/0004-6361/202245573

Batista, R. A., de Almeida, R. M., Lago, B., & Kotera, K. 2019, Journal of Cosmology and Astroparticle Physics, 2019, 002, doi: 10.1088/1475-7516/2019/01/002

Bionta, R. M., et al. 1987, Physical Review Letters, 58, 1494, doi: 10.1103/PhysRevLett.58.1494

Brown, L. M. 1978, Physics Today, 31, 23, doi: 10.1063/1.2995181

Chisari, N. E., et al. 2019, The Astrophysical Journal Supplement Series, 242, 2, doi: 10.3847/1538-4365/ab1658

Clark, B., et al. 2021, Journal of Instrumentation, 16, C10007, doi: 10.1088/1748-0221/16/10/C10007

Dodelson, S., & Schmidt, F. 2021, Modern Cosmology, second edition edn. (London, United Kingdom ; San Diego, CA: Academic Press, an imprint of Elsevier)

Drexlin, G., Hannen, V., Mertens, S., & Weinheimer, C. 2013, Advances in High Energy Physics, 2013, 1, doi: 10.1155/2013/293986

Driver, S. P., et al. 2022, Monthly Notices of the Royal Astronomical Society, 513, 439, doi: 10.1093/mnras/stac472

Event Horizon Telescope Collaboration. 2022, The Astrophysical Journal Letters, 930, L12, doi: 10.3847/2041-8213/ac6674

Fang, K., Banerjee, A., Charles, E., & Omori, Y. 2020, The Astrophysical Journal, 894, 112, doi: 10.3847/1538-4357/ab8561

Fang, K., Rodriguez, E. L., Halzen, F., & Gallagher, J. S. 2023, The Astrophysical Journal, 956, 8, doi: 10.3847/1538-4357/acee70

Fang, K., et al. 2022, Physical Review Letters, 129, 071101, doi: 10.1103/PhysRevLett.129.071101

Fedynitch, A., Engel, R., Gaisser, T. K., Riehn, F., & Stanev, T. 2015, Calculation of Conventional and Prompt Lepton Fluxes at Very High Energy, arXiv, doi: 10.48550/arXiv.1503.00544

Gaggero, D., Grasso, D., Marinelli, A., Urbano, A., & Valli, M. 2015, The Astrophysical Journal Letters, 815, L25, doi: 10.1088/2041-8205/815/2/L25

Góra, D., et al. 2018, Universe, 4, 128, doi: 10.3390/universe4110128

Greisen, K. 1966, Physical Review Letters, 16, 748, doi: 10.1103/PhysRevLett.16.748

Griffiths, D. J. 2011, Introduction to Elementary Particles, 2nd edn., Physics Textbook (Weinheim: Wiley-VCH)

Guevel, D., et al. 2023, The Astrophysical Journal, 950, 116, doi: 10.3847/1538-4357/accdde

Haungs, A., et al. 2006, Nuclear Physics B - Proceedings Supplements, 151, 167, doi: 10.1016/j.nuclphysbps.2005.07.031

HESS Collaboration, et al. 2016, Nature, 531, 476, doi: 10.1038/nature17147

Hillas, A. M. 1984, Annual Review of Astronomy and Astrophysics, 22, 425, doi: 10.1146/annurev.aa.22.090184.002233

Hirata, K., et al. 1987, Physical Review Letters, 58, 1490, doi: 10.1103/PhysRevLett.58.1490

Hooper, D. 2024, Particle Cosmology and Astrophysics (Princeton: Princeton University Press)

IceCube Collaboration, et al. 2013, Physical Review D, 88, 042004, doi: 10.1103/PhysRevD.88.042004

—. 2019, Physical Review D, 99, 032004, doi: 10.1103/PhysRevD.99.032004

—. 2020, Physical Review Letters, 125, 121104, doi: 10.1103/PhysRevLett.125.121104

—. 2021, Physical Review D, 104, 022002, doi: 10.1103/PhysRevD.104.022002

—. 2022a, Science, 378, 538, doi: 10.1126/science.abg3395

—. 2022b, The Astrophysical Journal, 928, 50, doi: 10.3847/1538-4357/ac4d29

—. 2023, Science, 380, 1338, doi: 10.1126/science.adc9818

—. 2024, Physical Review D, 110, 022001, doi: 10.1103/PhysRevD.110.022001

Jackson, J. D. 1999, Classical Electrodynamics, 3rd edn. (New York: Wiley)

Jansky, K. 1935, Proceedings of the Institute of Radio Engineers, 23, 1158, doi: 10.1109/JRPROC.1935.227275

Kelley, J. L., & IceCube Collaboration. 2014, in APPLICATIONS OF MATHEMATICS IN ENGINEERING AND ECONOMICS (AMEE'14), Sozopol, Bulgaria, 154–157, doi: 10.1063/1.4902795

Kelner, S. R., & Aharonian, F. A. 2008, Physical Review D, 78, 034013, doi: 10.1103/PhysRevD.78.034013

Kelner, S. R., Aharonian, F. A., & Bugayov, V. V. 2006, Physical Review D, 74, 034018, doi: 10.1103/PhysRevD.74.034018

Kovács, A., & Szapudi, I. 2015, Monthly Notices of the Royal Astronomical Society, 448, 1305, doi: 10.1093/mnras/stv063

Lesgourgues, J., & Pastor, S. 2012, Advances in High Energy Physics, 2012, 1, doi: 10.1155/2012/608515

Lund, N. 1984, Advances in Space Research, 4, 5, doi: 10.1016/0273-1177(84)90287-4

Mainzer, A., Grav, T., Bauer, J., et al. 2011, The Astrophysical Journal, 743, 156, doi: 10.1088/0004-637X/743/2/156

Matthews, J. N., & Jui, C. C. H. 2000, Nuclear Physics B - Proceedings Supplements, 87, 411, doi: 10.1016/S0920-5632(00)00706-4

Mattox, J. R., et al. 1996, The Astrophysical Journal, 461, 396, doi: 10.1086/177068

Mizuno, T., et al. 2015, The Astrophysical Journal, 803, 74, doi: 10.1088/0004-637X/803/2/74

Partenheimer, A., Fang, K., Batista, R. A., & de Almeida, R. M. 2024, The Astrophysical Journal Letters, 967, L15, doi: 10.3847/2041-8213/ad4359

Peebles, P. J. E. 1980, The Large-Scale Structure of the Universe, new paperback printing edn., Princeton Series in Physics (Princeton, New Jersey: Princeton University Press)

Rybicki, G. B., & Lightman, A. P. 1985, Radiative Processes in Astrophysics, 1st edn. (Wiley), doi: 10.1002/9783527618170

Sarkar, K. C. 2024, The Astronomy and Astrophysics Review, 32, 1, doi: 10.1007/s00159-024-00152-1

Schlafly, E. F., Meisner, A. M., & Green, G. M. 2019, The Astrophysical Journal Supplement Series, 240, 30, doi: 10.3847/1538-4365/aafbea

Schlegel, D. J., Finkbeiner, D. P., & Davis, M. 1998, The Astrophysical Journal, 500, 525, doi: 10.1086/305772

Settimo, M., et al. 2016, Journal of Physics: Conference Series, 718, 052037, doi: 10.1088/1742-6596/718/5/052037

Skrutskie, M. F., et al. 2006, The Astronomical Journal, 131, 1163, doi: 10.1086/498708

Spiering, C. 2012, The European Physical Journal H, 37, 515, doi: 10.1140/epjh/e2012-30014-2

Stein, R., van Velzen, S., Kowalski, M., et al. 2021, Nature Astronomy, 1, doi: 10.1038/s41550-020-01295-8

Su, M., Slatyer, T. R., & Finkbeiner, D. P. 2010, The Astrophysical Journal, 724, 1044, doi: 10.1088/0004-637X/724/2/1044

Tavernier, S. 2010, Experimental Techniques in Nuclear and Particle Physics (Berlin, Heidelberg: Springer Berlin Heidelberg), doi: 10.1007/978-3-642-00829-0

Tegmark, M., et al. 2004, Physical Review D, 69, 103501, doi: 10.1103/PhysRevD.69.103501

The IceCube Collaboration, Fermi-LAT, MAGIC, et al. 2018, Science, 361, eaat1378, doi: 10.1126/science.aat1378

THE Pierre Auger Collaboration, et al. 2017, Science, 357, 1266, doi: 10.1126/science.aan4338

Tung, C. F., Glauch, T., Larson, M., et al. 2021, Journal of Open Source Software, 6, 3194, doi: 10.21105/joss.03194

Wilks, S. S. 1938, The Annals of Mathematical Statistics, 9, 60, doi: 10.1214/aoms/1177732360

Zatsepin, G. T., & Kuz'min, V. A. 1966, Soviet Journal of Experimental and Theoretical Physics Letters, 4, 78

Zhang, P., & Beacom, J. F. 2004, The Astrophysical Journal, 614, 37, doi: 10.1086/423329